

**FIRST MULTISPACECRAFT ION MEASUREMENTS IN AND NEAR THE EARTH'S
MAGNETOSPHERE WITH THE IDENTICAL CLUSTER ION SPECTROMETRY
(CIS) EXPERIMENT**

by

H. REME, C. Aoustin, J.M. BOSQUED, I. DANDOURAS, B. LAVRAUD, J.A. SAUVAUD, A. BARTHE,
J. BOUYSSOU, Th. CAMUS, O. COEUR-JOLY, A. CROS, J. CUVILO, F. DUCAY, Y. GARBAROWITZ,
J.L. MEDALE, E. PENOU, H. PERRIER, D. ROMEFORT, J. ROUZAUD, C. VALLAT, D. ALCAYDE, C.
JACQUEY, C. MAZELLE, C. d'USTON
CESR, BP 4346, 31028 Toulouse Cedex 4, France

E. MÖBIUS, L.M. KISTLER, K. CROCKER, M. GRANOFF, C. MOUIKIS, M. POPECKI, M. VOSBURY
UNH, Durham, USA

B. KLECKER, D. HOVESTADT, H. KUCHAREK, E. KUENNETH, G. PASCHMANN, M. SCHOLER,
N. SCKOPKE (†), E. SEIDENSCHWANG
MPE, Garching, Germany

C.W. CARLSON, D.W. CURTIS, C. INGRAHAM, R.P. LIN, J.P. McFADDEN, G.K. PARKS, T. PHAN
SSL, Berkeley, USA

V. FORMISANO, E. AMATA, M.B. BAVASSANO-CATTANEO, P. BALDETTI, R. BRUNO, G.
CHIONCHIO, A. DI LELLIS, M.F. MARCUCCI, G. PALLOCCHIA
IFI, Roma, Italy

A. KORTH, P.W. DALY, B. GRAEVE, H. ROSENBAUER, V. VASYLIUNAS
MPAE, Lindau, Germany

M. McCARTHY, M. WILBER
U.W., Seattle, USA

L. ELIASSON, R. LUNDIN, S. OLSEN
IRF, Kiruna, Sweden

E.G. SHELLEY, S. FUSELIER, A.G. GHIEMMETTI, W. LENNARTSSON
Lockheed, Palo Alto, USA

C.P. ESCOUBET
ESA/ESTEC, Noordwijk, the Netherlands

H. BALSIGER
Bern University, Bern, Switzerland

R. FRIEDEL
Los Alamos National Laboratory NM, USA

J-B. CAO
CCSAR, Beijing, China

R. A. KOVRAZHKIN
IKI, Moscow, Russia

I. PAPAMASTORAKIS
University of Crete, Greece

R. PELLAT
Commissariat à l'Energie Atomique, Paris, France

J. SCUDDER
University of Iowa, USA

B. SONNERUP
Dartmouth College, USA

Revised version: June 30, 2001; accepted for publication, *Ann. Geophysicae*

ABSTRACT

On board the 4 Cluster spacecraft, the Cluster Ion Spectrometry (CIS) experiment measures the full three-dimensional ion distributions of the major magnetospheric ions (H^+ , He^+ , He^{++} , and O^+) from the thermal energies to about 40 keV/e. The experiment consists of two different instruments: a COmposition and DIstribution Function analyser (CIS1/CODIF) giving the mass per charge composition with medium (22.5°) angular resolution, and a Hot Ion Analyser (CIS2/HIA), which does not offer mass resolution but has a better angular resolution (5.6°) adequate for ion beam and solar wind measurements. Each analyser has two different sensitivities in order to increase the dynamic range. First tests of the instruments (commissioning activities) were achieved from early September 2000 to mid January 2001, and the operation phase began on February first 2001. In this paper, first results of the CIS instruments are presented showing the high level performances and capabilities of the instruments. Good examples of data obtained in the Central Plasma Sheet, Magnetopause crossings, magnetosheath, solar wind and cusp measurements. Observations in the auroral regions can be also obtained with the Cluster spacecraft at radial distances 4-6 Earth radii. These results show the tremendous interest of multispacecraft measurements with identical instruments and open a new area in magnetospheric and solar wind-magnetosphere interaction physics.

The CIS instrument on-board the Cluster mission has been described with many details in Rème et al. (1997). This paper included a complete description of the instruments built for the Cluster I mission. However, after the dramatic crash of the Ariane 5 launch on June 4, 1996 at Kourou, 4 new CIS instruments were rebuilt for the Cluster 2 mission. There are significant differences between the hardware, the software and the telemetry products for CIS instruments from Cluster to Cluster 2. For this reason a good up-to-date description of the instruments is given in this paper before the presentation of some first results. This paper must be the reference for the CIS Cluster-2 instruments.

Note that there is different naming for the spacecraft numbers, the spacecraft names, the spacecraft flight model numbers and the CIS experiment flight model numbers. Table 1 clarifies these different names and numbers.




| CLUSTER - II Spacecraft Number | Spacecraft Name | Spacecraft Color and Line Style | Spacecraft FM | | CIS FM Number and Color |
|--------------------------------------|--------------------|------------------------------------|-------------------------------------|------|--|
| 1 | <i>Rumba</i> | Black ————— | FM-5 (Phoenix) | | FM-8  |
| 2 | <i>Salsa</i> | Red ----- | <i>First 2 s/c launched</i> | FM-6 | FM-5  |
| 3 | <i>Samba</i> | Green | | FM-7 | FM-6  |
| 4 | <i>Tango</i> | Magenta ----- | FM-8 | | FM-7  |
| | | | | | Spare: FM-4 (Phoenix) |

Table 1: CIS Flight Model (FM) Naming

1. SCIENTIFIC OBJECTIVES AND EXPERIMENT CAPABILITIES

The prime scientific objective of the CIS experiment is the study of the dynamics of magnetized plasma structures in and in the vicinity of the Earth's magnetosphere, with the determination, as accurately as possible of the local orientation and the state of motion of the plasma structures required for macrophysics and microphysics studies. The four Cluster spacecraft with relative separation distances that can be adjusted to spatial scales of the structures (a few hundred kilometers to several thousand kilometers) give for the first time the unambiguous possibility to distinguish spatial from temporal variations.

The CIS experiment has been designed to provide very substantial contributions to:

- the study of the solar wind/magnetosphere interaction,
- the dynamics of the magnetosphere, including storms, substorms, and aurora,
- the physics of the magnetopause and of the bow shock,
- the polar cusps and the plasma sheet boundary layer dynamics,
- the upstream foreshock and solar wind dynamics,
- the magnetic reconnection and the field aligned current phenomena,
- the study of low energy ionospheric population.

The four Cluster spacecraft encounter ionic plasma of vastly diverse characteristics in the course of one year (Figure 1). In order to study all the plasma regions with the fluxes shown in Figure 1, the CIS experiment needs, therefore, to be a highly versatile and reliable ionic plasma experiment, with the following requirements:

- A very great dynamic range is necessary in order to detect fluxes as low as those of the lobes, but also those as high as solar-wind fluxes, throughout the solar cycle.

- A broad energy range and a full 4π angular coverage are necessary to provide a satisfactory and uniform coverage of the phase space with sufficient resolution. The angular resolution must be sufficient to be able to separate multiple populations, such as gyrating or transmitted ions from the main population downstream of the bow shock, and be able to detect fine structures in the distributions.
- Require a high angular and energy resolution in a limited energy and angular range for detection of cold beams, such as the solar wind. Because of the limited energy range required, a beam tracking algorithm has been implemented in order to follow the beam in velocity space. Moreover, in the foreshock regions, for example, any study of backstreaming ions requires the simultaneous observation of the solar-wind cold beam and of the backstreaming particles. Therefore, together with the solar-wind coverage described above, a coverage of the entire phase space excepting the sunward sector, with broad energy range, is also used.
- In the case of sharp boundaries, such as discontinuities, it is necessary not to miss any information at the discontinuity; thus a very efficient means of mode change, which allows adaptation to the local plasma conditions, is provided.
- Moments of the three-dimensional (3D) distribution (and of the sunward sector, in solar-wind mode) are computed on-board, with high time resolution, to continuously generate key parameters, necessary for event identification.
- To study detailed phenomena of complex magnetospheric plasma physics multiple particle populations must be identified and characterized; therefore, a 3D distribution is needed. In order to transmit the full 3D distribution, while overcoming the telemetry rate limitations, a compression algorithm has been introduced, which allows an increased amount of information to be transmitted.

To achieve the scientific objectives, the CIS instrumentation has been designed to satisfy the following criteria, simultaneously on the 4 spacecraft :

- * Provide a uniform coverage of ions over the entire 4π steradian solid angle with good angular resolution.
- * Separate the major mass ion species from the solar wind and ionosphere, i.e. those which contribute significantly to the total mass density of the plasma (generally H^+ , He^{++} , He^+ , and O^+).
- * Have high sensitivity and large dynamic range ($\geq 10^7$) to support high-time-resolution measurements over the wide range of plasma conditions to be encountered in the Cluster mission (Figure 1).
- * Have high ($5.6^\circ \times 5.6^\circ$) and flexible angular sampling resolution to support measurements of ion beams and solar wind.
- * Have the ability to routinely generate on-board the fundamental plasma parameters for major ion species and with one spacecraft spin time resolution (4 seconds). These parameters include the density (n), velocity vector (\mathbf{V}), pressure tensor (\mathbf{P}), and heat flux vector (\mathbf{H})
- * Cover a wide range of energies, from spacecraft potential to about 40 keV/e.
- * Have versatile and easily programmable operating modes and data-processing routines to optimize the data collection for specific scientific studies and widely varying plasma regimes.

To satisfy all these criteria, the CIS package consists of two different instruments: a Hot Ion Analyser (HIA) sensor and a time-of-flight ion COmposition and DIstribution Function (CODIF) sensor. The CIS plasma package is versatile and is capable of measuring both the cold and hot ions of Maxwellian and non-Maxwellian populations (for example, beams) from the solar wind, the magnetosheath, and the magnetosphere (including the ionosphere) with sufficient angular, energy and mass resolutions to accomplish the scientific objectives. The time resolution of the instrument is sufficiently high to follow density or flux oscillations at the gyrofrequency of H^+ ions in a magnetic field of 10 nT or less. Such field strengths can be frequently encountered by the Cluster mission. Oscillations of O^+ at the gyrofrequency can be resolved outside 6-7 R_E . Hence, this instrument package provides the ionic plasma data required to meet the Cluster science objectives (Escoubet and Schmidt, 1997).

2. THE HOT ION ANALYSER (HIA)

The Hot Ion Analyser (HIA) instrument combines the selection of incoming ions according to the ion energy per charge by electrostatic deflection in a symmetrical quadrispherical analyser which has a uniform angle-energy response with a fast imaging particle detection system. This particle imaging is based on microchannel plate (MCP) electron multipliers and position encoding discrete anodes.

2.1. ELECTROSTATIC ANALYSER DESCRIPTION

Basically the analyser design is a symmetrical quadrispherical electrostatic analyser which has a uniform 360° disc-shaped field of view (FOV) and extremely narrow angular resolution capability. This symmetric quadrisphere or 'top hat' geometry (Carlson *et al.*, 1982) has been successfully used on numerous sounding rocket flights as well as on the AMPTE/IRM, Giotto and WIND spacecraft (Paschmann *et al.*, 1985; Rème *et al.*, 1987; Lin *et al.*, 1995).

The symmetric quadrisphere consists of three concentric spherical elements. These three elements are an inner hemisphere, an outer hemisphere which contains a circular opening, and a small circular top cap which defines the entrance aperture. This analyser is classified as quadrispherical simply because the particles are deflected through 90° . In the analyser a potential is applied between the inner and outer plates and only charged particles with a limited range of energy and initial azimuth angle are transmitted. The particle exit position is a measure of the incident polar angle which can be resolved by a suitable position-sensitive detector system. The symmetric quadrisphere makes the entire analyser, including the entrance aperture, rotationally symmetric. The focusing characteristics are independent of polar angle. We use the following convention: the angle about the spin axis is the azimuth angle whereas the angle out of the spin plane is called polar angle.

The symmetrical quadrispherical analyser has good focusing properties, sufficient energy resolution, and the large geometrical factor of a quadrisphere. Because of symmetry, it does not have the deficiencies of the conventional quadrisphere, namely limited polar angle range and severely distorted response characteristics at large polar angles, and it has a uniform polar response.

The HIA instrument has $2 \times 180^\circ$ FOV sections parallel to the spin axis with two different

sensitivities, with a ratio of about 25 (depending of the flight model and precisely known from calibrations), corresponding respectively to the 'high G' and 'low g' sections. The 'low g' section allows detection of the solar wind and the required high angular resolution is achieved through the use of 8 x 5.625° central anodes, the remaining 8 sectors having in principle 11.25° resolution; the 180° 'high G' section is divided into 16 anodes, 11.25° each. In reality, sectoring angles are respectively $\sim 5.1^\circ$ and $\sim 9.7^\circ$, as demonstrated by calibrations (see section 2.5). This configuration provides 'instantaneous' 2D distributions sampled once per 62.5 ms (1/64 of one spin, i.e. 5.625° in azimuth), which is the nominal sweep rate of the high voltage applied to the inner plate of the electrostatic analyser to select the energy of the transmitted particles. For each sensitivity section a full 4π steradian scan is completed every spin of the spacecraft, i.e. 4 s, giving a full 3D distribution of ions in the energy range $\sim 5 \text{ eV e}^{-1}$ to 32 keV e^{-1} (the analyser constant being ~ 6.70). Figure 2 provides a cross-sectional view of the HIA electrostatic analyser. The inner and outer plate radii are 37.75 mm and 40.20 mm respectively. The analyser has an entrance aperture which collimates the field of view, defines the two geometrical factors and blocks the solar UV radiation.

2.2. DETECTION SYSTEM

A pair of half-ring microchannel plates (MCP) in a chevron pair configuration detects the particles at the exit of the electrostatic analyser. The plates form a 2 x 180° ring shape, each 1 mm thick with an inter-gap of $\sim 0.02 \text{ mm}$, with an inner diameter of 75 mm and outer diameter of 85 mm. The MCPs have 12.5 μm straight microchannels with a bias angle of 8° to reduce variations in MCP efficiency with azimuthal direction. The chevron configuration with double thickness plates provides a saturated gain of 2×10^6 , with a narrow pulse height distribution. The plates have a high strip current to provide fast counting capability. For a better detection efficiency ions are post-accelerated by a $\sim 2300 \text{ V}$ potential applied between the front of the first MCP and a high-transparency grid located $\sim 1 \text{ mm}$ above. The anode collector behind the MCPs is divided into 32 sectors, each connected to its own pulse amplifier (Figure 3).

Main performances of the HIA sensor are summarised in Table 2.

- Full 3D ion distribution functions
- Flux as a function of time, mass and pitch angle
- Moments of the distribution functions : density, bulk velocity, pressure tensor, heat flux vector
- Beams

| Analysers | Energy Range | Energy Distribution (FWHM) | Time Resolution | | Mass Resolution M/DM | Angular Resolution | Geometrical Factor (Total) $\text{cm}^2.\text{sr.keV/keV}$ | Dynamics $(\text{cm}^2 \text{ sec sr})^{-1}$ |
|---|---|----------------------------|-----------------|------|----------------------|-------------------------------------|--|--|
| | | | 2D ms | 3D s | | | | |
| Hot Ion Analyser HIA | $\sim 5 \text{ eV/e} - 32 \text{ keV/e}$ | 18% | 62.5 | 4 | - | $\sim 5.6^\circ \times 5.6^\circ$ | 1.9×10^{-4} for one half $4.9.10^{-3}$ for the other half | $10^4 - 2 \times 10^{10}$ |
| Ion Composition and Distribution Function Analyser CODIF | $\sim 0 - 38 \text{ keV/e}$ Mass range 1 – 32 amu | 16% | 125 | 4 | $\sim 4 - 7$ | $\sim 11.2^\circ \times 22.5^\circ$ | 1.9×10^{-2} for one half 2.1×10^{-4} for the other half $3.0 \times 10^{-2} \text{ cm}^2 \text{ sr}$ for the RPA | $3.10^3 - 3.10^9$ |

| Analysers | Full Instantaneous Field of View | Mass | Power (Nominal Operations) |
|---|----------------------------------|---------|----------------------------|
| Hot Ion Analyser HIA | $8^\circ \times 360^\circ$ | 2.45 kg | 2.82 watts |
| Ion Composition and Distribution Function Analyser CODIF | $8^\circ \times 360^\circ$ | 8.39 kg | 6.96 watts |

CIS total raw CIS Total Weight : 10.84 kg without harness
Average power : 9.78 watts

CIS Telemetry : $\sim 5.5 \text{ kbit/s}$
Expected total bit number (for the 4 spacecraft) : 10^{12} bits

Table II. Main features and measured parameters of the CIS experiment

2.3. SENSOR ELECTRONICS

Signals from each of the 32 MCP sectors are sent through 32 specially designed very fast A121 charge-sensitive amplifier/discriminators that are able to count at rates as high as 5 MHz. Output counts from the 32 sectors are accumulated in 48 counters (including 16 redundant counters for the solar wind), thus providing the basic angular resolution matrix according to the resolution of the anode sectoring.

According to the operational mode several angular resolutions can be achieved:

- * in the normal resolution mode, the full 3D distributions are covered in $\sim 11.25^\circ$ angular bins ("high G" geometrical factor); this is the basic mode inside the magnetosphere;
- * in the high resolution mode the best angular resolution, $\sim 5.6^\circ \times 5.6^\circ$, is achieved within a 45° sector centred on the Sun direction, using the 'low g' geometrical factor section; this mode is dedicated to the detection of the solar wind and near-ecliptic narrow beams.

High voltage power supplies

HIA needs a high-voltage power supply to polarise MCPs at ~ 2300 - 2500 V and a sweeping high voltage applied on the inner plate of the electrostatic analyser. The high voltages to polarise the MCPs are adjustable under control of the data processor system (DPS) microprocessor.

The energy/charge of the transmitted ions is selected by varying the deflection voltage applied to the inner plate of the electrostatic analyser, between 4800 and 0.7 V. The exponential sweep variation of the deflection voltage is synchronised with the spacecraft spin period. The sweep should consist of many small steps that give effectively a continuous sweep. The counter accumulation time defines the number of energy steps, i.e. 31 or 62 count intervals per sweep. The covered energy range and the sweeping time are controlled by the onboard processor through a 12 bit DAC and a division in two ranges for the sweeping high voltage. So the number of sweeps per spin, the amplitude of each sweep and the sweeping energy range can be adjusted according to the mode of operation (solar wind tracking, beam tracking, etc.). In the basic and nominal mode the sweep of the total energy range is repeated 64 times per spin, i.e. once every 62.5 ms, giving a $\sim 5.6^\circ$ resolution in azimuth resolution. In the solar wind mode, HIA sweep is truncated when "high G" is facing the Sun in order to avoid the solar wind detection with "high G" and to protect the MCP lifetime.

2.4. IN-FLIGHT CALIBRATION TEST

A pulse generator can stimulate the 32 amplifiers under processor control. In this way important functions of the HIA instrument and of the associated on-board processing can easily be tested. A special test mode is implemented for health checking of the microprocessor by making ROM checksums and RAM tests. The sweeping high voltage can be tested by measuring the voltage value of each individual step and the MCP gain can be checked by occasionally stepping MCP HV and by adjusting the discrimination level of charge amplifiers. Performances of the HIA sensor are shown in Table 2 and in Figure 1.

2.5. HIA PERFORMANCES

Pre-flight and extensive calibrations of all four HIA flight models and of the spare model were performed at the CESR vacuum test facilities in Toulouse, using large and stable ion beams of different ion species and variable energies, detailed studies of MCPs and gain level variations, MCP matching, angular-energy resolution for each sector from a few tens of eV up to 30 keV. Typical performances of the HIA instrument are reproduced in Figures 4, 5 and 6. Figure 4 shows an example of typical energy and angular resolutions of the HIA analyser (flight model FM5/SC2) for an energy beam of 800 eV; in this case the energy resolution is 16.3 % and the intrinsic azimuthal resolution $\sim 5.5^\circ$. In average the analyser energy resolution $\Delta E/E$ (FWHM) is $\sim 17\%$, almost independent of anode sectors and energy; thus the intrinsic HIA velocity resolution is $\sim 9\%$, only about half of the average solar wind spread value. This is equivalent to an angular resolution of $\sim 5^\circ$ and is thus quite consistent with the angular resolution capabilities of the instrument, i.e. $\sim 5.9^\circ$ (FWHM) in azimuthal angle, as indicated in Figure 4, and $\sim 5.6^\circ$ in polar angle. As seen in the example of Figure 5 for the model FM6/SC3, the polar resolution stays, as expected, almost constant, $\sim 9.70^\circ$, over the 16 sectors (anodes 0 to 15) constituting the 'high G' section (Figure 5). Anodes 16 to 31 correspond to the 'low g' section and their response transmission is attenuated by a factor of about 25 (depending of the flight model, see Table 3) due to the presence of a pin-hole grid placed in front of the 180° collimator; the polar resolution of sectors 20 to 27 is $\sim 5.2^\circ$. Figure 6 shows the excellent agreement for the transmission width for the 4 flight models and the spare model. Thus, when compared to the basic sectoring, $\sim 5.6^\circ$ and $\sim 11.2^\circ$, all effective polar resolutions are reduced, due to existence of an insulation space between the discrete anodes, as well as by the presence of support posts within the field of view. Finally, experimental energy, angle resolutions and transmission factors are introduced in the geometrical factor used to compute moments of the distribution function.

| Parameter | FM5/SC2 | | FM6/SC3 | | FM7/SC4 | | FM8/SC1 | | FM4/SPARE | |
|--|-------------------------|--------------------------|--------------------------|--------------------------|--------------------------|--------------------------|--------------------------|--------------------------|-----------|-------|
| Geometrical Factor | G | g | G | g | G | g | G | g | G | g |
| Attenuation grid | 1 | 1/24 | 1 | 1/22 | 1 | 1/25 | 1 | 1/25 | 1 | |
| ? E/E, % | 16.44 | 15.94 | 16.66 | 15.96 | 17.61 | 17.23 | 16.59 | 16.07 | 17.19 | 17.32 |
| K analyser (all sectors) | 7.629 | | 7.341 | | 7.042 | | 7.685 | | 7.454 | |
| Geometrical Factor per anode (cm ² .sr.keV/keV) | 3.00 x 10 ⁻⁴ | 5.769 x 10 ⁻⁶ | 3.805 x 10 ⁻⁴ | 1.084 x 10 ⁻⁵ | 3.403 x 10 ⁻⁴ | 6.368 x 10 ⁻⁶ | 4.966 x 10 ⁻⁴ | 1.226 x 10 ⁻⁵ | | |

Table 3. Energy resolution, analyser constant and geometrical factor per anode for the 4 HIA flight models and for the spare model. High geometrical factor corresponds to 0-15 sectors and low geometrical factor corresponds to 20-27 sectors (see Figure 3). These parameters are slightly different from the parameters of the Cluster-1 models due to the modification of the sphere scalloping design used to obtain a better UV rejection (see below).

UV Rejection

A number of very interesting events are expected to occur when the HIA spectrometers face the Sun (2 times/spin): of course the intense solar wind, but also, for example, tailward ion beams flowing along the Plasma Sheet Boundary Layer (PSBL). A number of measures were applied in order to suppress or limit the solar UV contamination. Part of the UV is rejected by the entrance collimator; moreover, the inner surface of the outer sphere is scalloped and both spheres (and all internal parts) are treated and coated with a special black cupric sulfide. Extensive vacuum chamber tests of the HIA analysers were performed, using a calibrated continuous discharge source for extreme UV at He-584 Å and L α 1215 Å lines. Reduction of the solar UV light reflectance at the L α line were demonstrated in Rème et al. (1997) for Cluster 1 flight models. The resulting maximum count rate recorded by the sunward looking sector (11.2° wide) for these models was about 80 counts s⁻¹ (for an intensity equivalent to 3 Sun intensity units) and the UV contamination was distributed over about ~100° in polar angle; this UV contamination was judged acceptable. Figure 7a shows this UV contamination for a Cluster-1 HIA flight model. However for Cluster-2 flight models, it was decided to improve the UV rejection by changing the scalloping of the outer sphere. The result is excellent. Figure 7b shows the UV test result for FM4 spare model in the same conditions for that of Figure 7a for Cluster-1. The contamination is divided by a factor of about 700. In Figure 8 is shown an example of measurements by HIA FM6/SC3 instrument in the Central Plasma Sheet on September 11, 2000. "Natural counts" are detected between about 150 eV and 14 keV. The UV rejection is excellent because there are no counts in the sun direction (+ and - 180°) for the highest energy ion measurements where no natural particle are present in this region. In the same Figure the absence of counts at the lowest and highest energies, ie below and above the Central Plasma Sheet particle energies show that the HIA sensors have a very low MCP and amplifier noise.

3. THE ION COMPOSITION AND DISTRIBUTION FUNCTION ANALYSER (CODIF)

The CODIF instrument is a high-sensitivity mass-resolving spectrometer with an instantaneous 360° x 8° field of view to measure complete 3D distribution functions of the major ion species, within one spin period of the spacecraft. Typically these include H⁺, He⁺⁺, He⁺ and O⁺. The sensor primarily covers the energy range between 0.02 and 38 keV/charge. With an additional Retarding Potential Analyser (RPA) device in the aperture system of the sensor with pre-acceleration for energies below 25 eV/e, the range is extended to energies as low as the spacecraft potential. Hence, CODIF covers the core of all plasma distributions to importance of the Cluster mission.

To cover the large dynamic range required for accurate measurements in the low-density plasma of the magnetotail and the dense plasma in the magnetosheath/cusp/ boundary layer, it is mandatory that CODIF employ two different sensitivities. The minimum number of counts in a distribution needed for computing the basic plasma parameters, such as the density, is about 100. These must be accumulated in 1 spin to provide the necessary time resolution. However, the maximum count rate which the time-of-flight system can handle is ~10⁵ counts s⁻¹ or 4 x 10⁵ counts spin⁻¹. This means the dynamic range achievable with a single sensitivity is only 4 x 10³.

Figure 1 shows the fluxes covered by CODIF ranging from magnetosheath/magnetopause protons to tail lobe ions (which consist of protons and heavier ions); fluxes from $\sim 10^3$ to over 10^8 must be covered, requiring a dynamic range of larger than 10^5 . This can only be achieved if CODIF incorporates two sensitivities, differing by a factor of about 100. CODIF therefore consists of two sections, each with 180° field of view, with different (by a factor of 100) geometrical factors. This way one section has always count rates which are statistically meaningful and at the same time can be handled by the time-of-flight electronics. The exception is solar wind H^+ which often saturates the instrument, but is measured with the small g of HIA.

The CODIF instrument combines ion energy per charge selection by deflection in a rotationally symmetric toroidal electrostatic analyser with a subsequent time-of-flight analysis after post-acceleration to ≥ 15 keV/e. A cross section of the sensor showing the basic principles of operation is presented in Figure 9. The energy-per-charge analyser is of a rotationally symmetric toroidal type, which is basically similar to the quadrispheric top-hat analyser used for HIA. It has a uniform response over 360° of polar angle. The energy per charge selected by the electrostatic analyser E/Q , the energy gained by post-acceleration $e.U_{ACC}$, and the measured time-of-flight through the length d of the time-of-flight (TOF) unit, τ , yield the mass per charge of the ion M/Q according to: $M/Q = 2(E/Q + e.U_{ACC}) / (d/\tau)^2 \cdot \alpha$. The quantity α represents the effect of energy loss in the thin carbon foil ($\sim 3 \mu\text{g cm}^{-2}$) at the entry of the TOF section and depends on particle species and incident energy.

3.1. ELECTROSTATIC ANALYSER DESCRIPTION

The electrostatic analyser (ESA) has a toroidal geometry which provides optimal imaging just past the ESA exit. This property was first demonstrated by Young *et al.* (1988). The ESA consists of inner and outer analyser deflectors, a top-hat cover and a collimator. The inner deflector consists of toroidal and spherical sections which join at the outer deflector entrance opening (angle of 17.9°). The spherical section has a radius of 100 mm and extends from 0 to 17.9° about the z -axis. The toroidal section has a radius of 61 mm in the poloidal plane and extends from 17.9° to 90° . The outer deflector covers the toroidal section and has a radius of 65 mm. The top-hat cover consists of a spherical section with a radius of 113.2 mm, which extends from 0 to 16.2° . It thus fits inside the entrance aperture of the outer deflector. The outer deflector and the top-hat cover are at signal ground under normal operation, but are biased at about -100 V during RPA operation. The inner deflector is biased with voltages varying from -1.9 to -4950 V to cover the energy range in normal ESA operation and set to about -113 V for the RPA.

The fact that the analyser has complete cylindrical symmetry provides the uniform response in polar angle. A beam of parallel ion trajectories is focused to a certain location at the exit plane of the analyser. The exit position, and thus the incident polar angle of the ions, is identified using the information from the start detector (see Section 3.2). The full angular range of the analyser is divided into 16 channels of 22.5° each. The broadening of the focus at the entrance of the TOF section is small compared to the width of the angular channels.

As illustrated in Figure 9, the analyser is surrounded by a cylindrical collimator which serves to define the acceptance angles and restricts UV light. The collimator consists of a cylindrical can with an inner radius of 96 mm. The entrance is covered by an attenuation grid with a radius of 98 mm which is kept at spacecraft ground. The grid has a 1% transmission factor over 50% of the analyser entrance and $> 95\%$ transmission over the remaining 50%. The high

transmission portion extends over the azimuthal angle range of 0 to 180° where 0° is defined along the spacecraft spin axis. The low transmission portion, whose active entrance only extends from 22.5° to 157.5° in order to avoid the counting of any crossover from the other half, has a geometric factor that is reduced by a factor of ≈ 100 in order to extend the dynamic range to higher flux levels. On the low-sensitivity half, the collimator consists of a series of 12 small holes vertically spaced by approximately 1.9° around the cylinder. These apertures have acceptance angles of 5° FWHM, so there are no gaps in the polar angle coverage. The ion distributions near the polar axis are highly over-sampled during one spin relative to the equatorial portion of the aperture. Therefore, count rates must be weighted by the sine of the polar angle to normalise the solid-angle sampling for the moment calculations and 3D distributions.

The analyser has a characteristic energy response of about 7.6, and an intrinsic energy resolution of $\Delta E/E \approx 0.16$. The entrance fan covers a viewing angle of 360° in polar angle and 8° in azimuth. With an analyser voltage of 1.9- 4950 V, the energy range for ions is 15 - 38000 eV/e. The deflection voltage is varied in an exponential sweep. The full energy sweep with 30 contiguous energy channels is performed 32 times per spin. Thus, a partial two-dimensional cut through the distribution function in polar angle is obtained every 1/32 of the spacecraft spin. The full 4π ion distributions are obtained in a spacecraft spin period.

The outer plate of the analyser is serrated in order to minimize the transmission of scattered ions and UV. For the same reason the analyser plates are covered with a copper black coating. Behind the analyser the ions are accelerated by a post-acceleration voltage of -14 to -25 kV, such that also thermal ions have sufficient energy before entering the TOF section. After the first in-flight tests this high voltage has been put at -15 kV in all the spacecraft, giving good results and safe use of CODIF.

Retarding Potential Analyser

In order to extend the energy range of the CODIF sensor to energies below 15 eV/e, an RPA assembly is incorporated in the two CODIF apertures (see Figure 10). The RPA provides a way of selecting low-energy ions as input to the CODIF analyser without requiring the ESA inner deflector to be set accurately near 0 V. The RPA collimates the ions, provides a sharp low-energy cutoff at a normal incident grid, pre-accelerates the ions to 100 eV after the grid, and deflects the ions into the ESA entrance aperture. The energy pass of the ESA is about 5-6 eV at 100 eV of pre-acceleration, assuming all deflection voltages are optimised. This energy pass is very sensitive to the actual RPA deflection optics, so that deflection voltages have to be determined at about the 1% level.

The RPA assembly consists of a collimator, RPA grid and pre-acceleration region, and deflection plates. The collimator section is kept at spacecraft ground. When the RPA is active, only RPA measurements are produced by CODIF. The RPA can be thought of as a separate ion optics front end for CODIF which can be switched in on command, replacing the normal ion optics. A separate RPA aperture ring defines a field of view parallel to the normal CODIF field of view, but displaced towards the analyser top by about 15 mm. As with normal CODIF operations, the field of view extends 180° in azimuth on one side of the analyser and 135° on the other side. Only one side can be active at a time. Unlike the normal CODIF entrance aperture, both sides of the RPA have the same sensitivity; there is no attenuation grid on one half to reduce the effective geometric factor for the RPA.

When the RPA is enabled, the normal entrance aperture is shuttered off by a positively biased grid, which pushes ions near 100 eV/e away from the entrance slot below the top cap. Although higher energy ions could still enter this slot, the bias between hemispheres is set to pass energies near 100 eV/e only, so that higher energy ions strike the inner hemisphere, and fail traversing the analyser gap to exit ring. A retarding grid at the RPA entrance rejects ions with energy/charge below the set threshold voltage and allows higher energy/charge ions to pass. The accepted ions are first collimated and accelerated by 100 volts, and then routed by 3 deflector surfaces into the main entrance slot. The hemispherical analyser filters out the higher energies from the incoming beam and the remainder enter the TOF section for a velocity measurement. The deflection system provides a method of steering the RPA low-energy ions into the CODIF ESA.

The RPA grid and pre-acceleration region consist of a pair of cylindrical rings, sandwiched between resistive ceramic material. Both inner and outer cylindrical rings contain apertures separated by posts every 22.5° , similar to the ESA collimator entrance, to allow the ions to pass through the assembly. The RPA grid is attached to the inner surface of the outer cylindrical ring. This outer ring has a small ledge which captures the RPA grid and which also provides the initial optical lens that is crucial to the RPA operation. Both inner and outer cylindrical rings are in good electrical contact with the resistive kapton (silver epoxy). During RPA operation the outer cylindrical ring is biased from spacecraft ground to about + 25 V and provides the sharp low- energy RPA cutoff. This voltage is designated V_{rpa} in Figure 10. The inner cylindrical ring tracks the outer ring voltage and is biased at $-100 \text{ V} + V_{rpa}$. The inner cylindrical ring, the ESA outer deflector, and the ESA top-hat cover are electrically tied to the RPA deflector.

The RPA deflection plates consist of three toroidal deflectors located above the ESA collimator entrance and one deflector disk located below the collimator entrance. The three toroidal deflectors are used to deflect the ions into the ESA. The deflector disk is used to prevent low-energy ions from entering the main aperture and to collect any photoelectrons produced inside the analyser, while in RPA mode.

3.2. TIME-OF-FLIGHT AND DETECTION SYSTEM

The CODIF sensor uses a time-of-flight technology (Möbius *et al.*, 1985). The specific parameters of the time-of-flight spectrometer have been chosen such that a high detection efficiency of the ions is guaranteed. High efficiency is not only important for maximizing the overall sensor sensitivity, but it is especially important for minimising false mass identification resulting from false coincidence at high counting rate. Too thin a carbon foil would result in a significant reduction in the efficiency of secondary electron production for the 'start' signal, while an increase in thickness does not change the secondary electron emission significantly (Ritter, 1985). Under these conditions a post-acceleration of $\geq 14 \text{ kV}$ is necessary for the mass resolution of the sensor.

After passing the ESA the ions are focused onto a plane close to the entrance foil of the time-of-flight section (Figure 11). The TOF section is held at the post-acceleration potential in order to accelerate the ions into the TOF section.

In the TOF section, the velocity of the incoming ions is measured. The flight path of the ions is defined by the 3 cm distance between the carbon foil at the entrance and the surface of the 'stop' microchannel plate (MCP). The start signal is provided by secondary electrons, which

are emitted from the carbon foil during the passage of the ions. The entrance window of the TOF section is a $3\mu\text{g cm}^{-2}$ carbon foil, which is an optimum thickness between the needs of low-energy loss and straggling in the foil and high efficiency for secondary electron production. The electrons are accelerated to 2 keV and deflected onto the start MCP assembly by a suitable potential configuration.

The secondary electrons also provide the position information for the angular sectoring. The carbon foil is made up of separate 22.5° sectors, separated by narrow metal strips. The electron optics are designed to strongly focus secondary electrons originating at a foil onto the corresponding MCP start sector.

The MCP assemblies (Figure 11) are ring-shaped with inner and outer radii of 6 x 9 cm and 3 x 5 cm for the stop and start detectors, respectively. For the start signals, the output of the MCPs is collected on a set of segmented plates behind the MCPs (22.5° each), and on thin wire grids with $\approx 50\%$ transmission at a distance of 10 mm in front of the signal plates. The stop signals are collected through a solid non transparent grid (and not through a semi transparent grid like for Cluster 1), improving a lot the H^+ detection efficiency. All are at ground potential (see Figure 9). Thus almost all of the post-acceleration voltage is applied between the rear side of the MCPs and the signal anodes. The timing signals are derived from the 50% transmission grids, separately for the high- and the low-sensitivity TOF section. The position signals, providing the angular information in terms of 22.5° sectors, are derived from the signal plates behind the start MCP.

Main performances of the CODIF sensor are summarised in Table 2.

3.3. SENSOR ELECTRONICS

The sensor electronics of the instrument comprise two time-to-amplitude converters (TACs) to measure the time-of-flight of the ions between the start carbon foil and the stop MCPs, two sets of eight position discriminators at the start MCPs, two sets of two position discriminators at the stop MCPs, and the event selection logic. Each individual ion is pulse-height-analysed according to its time-of-flight, incidence in azimuthal (given by the spacecraft spin) and polar angle (given by the start position), and the actual deflection voltage.

The eight position signals for each TOF section (one TOF section for Low Side, one TOF for High Side, see Figure 11), in order to achieve the 22.5° resolution in polar angle, are independently derived from the signal anodes, while the timing signals are taken from the grids in front of the anodes. Likewise, the stop MCPs, consisting of four individual MCPs, are treated separately to carry along partial redundancy. By this technique the TOF and the position signals are electrically separate in the sensor. The position pulses are fed into charge-sensitive amplifiers and identified by pulse discriminators, the signal of which is directly fed into the event selection logic. The TOF unit is divided into two TOF channels.

The conditions for valid events are established in the event-selection logic. The respective coincidence conditions can be changed via ground command. Several count rates are accumulated in the sensor electronics. There are monitor rates of the individual start and stop detectors to allow continuous monitoring of the carbon foil and MCP performance. The total count rates of TOF coincidence show the valid events accumulated for each TOF section. These rates can be compared with the total stop count rates in order to monitor in-flight the efficiency of the start and stop assemblies.

In order to protect the MCPs, the solar-wind protons and the solar-wind alpha particles are blocked from detection by a simple scheme during the sweeping cycle, as shown in Figure 12 (actually there are 4 consecutive sweeps that are modified when G is facing the solar wind, whereas they are not modified when g is facing the solar wind). The sweep, starting at high energies, is shown for the high-sensitivity section in the upper panel and for the low-sensitivity section in the lower panel in $\log E$ and azimuthal angle. The voltage sweep, which starts at high energies, is stopped above the alphas when the high-sensitivity section is facing the solar wind. The result is a small data gap for both sections of the sensor simultaneously. The primary purpose for introducing this scheme is to avoid short-time gain depression of the MCP area which would otherwise persist for the order of 1 s after the impulsive high count rate that would result from the solar wind.

High voltage system

A sweep-voltage high-voltage power supply generates an exponential voltage waveform from 1.9 to 4950 V for the electrostatic analyser. A ≥ 14 kV static supply feeds the post-acceleration voltage, which can be adjusted via ground command. Another adjustable supply is used for the MCPs and the collection of secondary electrons. It supplies up to 5 kV and is floated on top of the post-acceleration voltage.

3.4. IN-FLIGHT CALIBRATION

Upon command, an in-flight-calibration (IFC) pulse generator can stimulate the two independent TOF branches of the electronics according to a predefined program. Within this program all important functions of the sensor electronics and the subsequent on-board processing of the data can be automatically tested. Temporal variations of calibration parameters can be measured. The in-flight calibration can also be triggered by ground command in a very flexible way, e.g. for trouble shooting purposes. In addition, the known prominent location of the proton signal can, if necessary, serve as a tracer of changes in the sensor itself.

3.5. CODIF PERFORMANCES

3.5.1. Resolution in Mass per Charge

The instrumental resolution in mass per charge is determined by a combination of the following effects:

- * energy resolution of the electrostatic deflection analyser ($\Delta E/E = 0.16$);
- * TOF dispersion caused by the angular spread of the ion trajectories because of the characteristics of the analyser and the straggling in the carbon foil (the angular spread of $= 13^\circ$ leads to $\Delta\tau/\tau = 0.03$);
- * TOF dispersion caused by energy straggling in the carbon foil ($\Delta\tau/\tau$ up to $= 0.08$ for 25 keV O^+);
- * electronic noise in the TOF electronics and secondary-electron flight time dispersion (typically 0.3 ns).

The resulting TOF dispersion amount $\Delta\tau/\tau \leq 0.1$, which finally leads to a M/Q resolution between 0.15 for H^+ and 0.25 for low energy O^+ .

3.5.2. CODIF Calibrations

The TOF efficiency is a function of the ion species and the total energy, the sum of the original ion energy plus the energy gained in the post-acceleration potential. The total efficiency for measuring an ion in CODIF is determined by the efficiency of the "Start" signal, the efficiency of the "Stop" signal, and the efficiency of "Valid Single Events". The "Start" efficiency is a function of the number of secondary electrons emitted from the carbon foil, the focusing of the electrons onto the MCP, the MCP active area, and the MCP gain and MCP signal threshold. It is measured using the ratio of the Start-Stop Coincidence rate (SFR) to the "Stop" rate (SR). The "Stop" efficiency is a function of the scattering of the ion in the foil (which can scatter it away from the active area), and again of the MCP active area, MCP gain and signal threshold. It is given by the ratio of SFR rate to the "Start" rate, SF. In order for an ion to be counted as a valid event, it must generate not only a start and stop signal, but also a single "Start Position" (PF) signal. The "Valid Event Efficiency" is given by the ratio of the valid Single event rate, SEV, to SFR. These efficiencies are all a function of energy and species, as well as MCP voltage. Determining the final efficiencies is done in two steps. First the optimum voltage at which to run the MCP's is determined. Then, using the optimum MCP voltage, the efficiencies for each species as a function of energy and position are determined.

Each CODIF model, including the spare model, has been very well calibrated. As an example are presented here the results for CODIF CIS model FM7, put on spacecraft 4. For the other models see the full report of L. Kistler (2000).

To determine ion efficiencies verses energy, once the optimum MCP voltage is set, data are collected over a range of beam energies. The total ion efficiency is a function of total ion energy (original beam energy plus post-acceleration). Even when the instrument is operating at the optimum MCP voltage, there is a significant difference between the final efficiencies measured at different positions (pixels). Thus it was necessary to determine the final ion efficiencies as a function not only of energies and species, but also of position.

Figures 13, 14 and 15 are plots of the total adjusted ion efficiencies verses total beam energy on both High Side (HS) and Low Side (LS) for H^+ , He^+ , and O^+ ions. The efficiency for He^{++} is the same as for He^+ at the same total energy (not energy per charge). Since He^{++} goes to twice the energy, we did separate curve fits for He^{++} (not shown) to assure that the curves were stable at higher energies.

Figure 16 shows the time-of-flight spectra over a range of energies for FM7. This Figure is assembled from many data sets using individual species. The relative heights of the peaks depend on the beam intensity and length of the run, and so have no significance for his analysis. The vertical lines show the thresholds used to distinguish species. During commissioning, it was found that a large peak can be observed in the lowest channel, and during time periods with a high oxygen flux, there is a second peak below the proton peak which seems to be correlated with the O^+ flux. It is probably due to ions with a time-of-flight greater than the allowed 200 ns from the long O^+ tail. To keep these spurious peaks from being counted with the protons, a threshold below the H^+ peak was introduced.

The mass resolution of the CODIF instrument is defined by the resolution in time-of-flight. The width of the peaks in time-of-flight is determined by the spread in energy that results from energy loss in the carbon foil and any noise in the time-of-flight electronics. Because the energy loss is a statistical process, ions which enter the foil with one energy come out with a range of energies. The percentage of energy lost is the worst for low-energy ions and heavy

ions. The electronic noise in the time-of-flight circuit is independent of ion energy. Because the loss in the carbon foil is a smaller fraction of the total energy, the peaks should get narrower with increasing energy. This is evident in the O^+ peaks, but is not so clear for the lower mass peaks. One reason for this is that there is a significant difference between the locations of the peaks for different positions. Because the peaks move closer together with energy, but the width of the low mass ions does not significantly improve, there are more problems with overlapping peaks, and therefore worse mass resolution, at high energies. The bin with the most overlap with other species is the He^{++} bin. A quantitative analysis of the spill-over between bins is shown in Figure 17. Each panel shows the fraction of a particular species which is classified in a particular mass bin. The thresholds were chosen to maximize the percentage of an ion that falls into the correct bin, but also to minimize the percentage of H^+ that falls into the wrong bin. This is particularly important at the H^+/He^{++} boundary. Because there is usually much more H^+ than He^{++} in space plasmas, a small percentage of H^+ spilling into the He^{++} bin can significantly effect the He^{++} measurement. In this case, about 3.5% of the H^+ falls into the He^{++} bin, and 70% of the He^{++} is in the He^{++} bin. For O^+ , the fraction that falls into the O^+ bin was kept low at low energies to reduce the background in the bin. At 15 keV, the O^+ has a long tail extending to high TOF channels. The background from accidental coincidences in a bin is proportional to the number of TOF channels in the bin, so there is an advantage to keeping a narrow bin, even if some of the real signal is lost.

The RPA geometric factor and Energy response has been also calibrated (McCarthy, 2000). For the group of 8 anodes when the high sensitivity side is enabled, the total RPA geometric factor is $3.0 \times 10^{-2} \text{ cm}^2.\text{sr}$. It is $2.2 \times 10^{-2} \text{ cm}^2.\text{sr}$ for the group of 6 anodes when the low sensitivity side is enabled.

3.5.3. Dynamic Range

The design of the electrostatic analyser guarantees a large geometrical factor in the high-sensitivity section $A\Delta E/E\Delta\tau\pi = 0.025 \text{ cm}^2.\text{sr}$. The energy bandwidth is $\Delta E/E = 0.16$. The efficiency of the TOF unit is about 0.5. Differential energy fluxes as low as $\sim 3 \times 10^3 \text{ ions s}^{-1} \text{ cm}^2 \text{ sr}^{-1}$ can be detected by the instrument with the full time resolution of 1 spin period and about 5 counts energy⁻¹ channel. The sensitivity is increased for longer integration time accordingly. Therefore the dynamic range reaches seven decades. The upper flux limit of the instrument amounts to $3 \times 10^9 \text{ ions s}^{-1} \text{ cm}^2 \text{ sr}^{-1}$, which leads to a count rate of $10^5 \text{ counts s}^{-1}$ in one TOF unit (near saturation of the analysing electronics) and still guarantees a mass density determination to better than 10 % accuracy for the reduced aperture geometry.

| Model | High Side Geometrical Factor* (averaged) cm^2sr | Low Side Geometrical Factor* (averaged) cm^2sr | k Analyser Constant | ? a (full) FWHM (degrees) |
|-------------|---|--|---------------------------|------------------------------------|
| FM5 | 2.58E-03 | | 7.382 | 6.124 |
| FM6 | 2.45E-03 | | 7.217 | 5.774 |
| FM7 | 2.53E-03 | 2.36E-05 | 7.412 | 5.790 |
| FM8 | 1.85E-03 | 2.61E-05 | 7.455 | 6.271 |
| FM4 (spare) | 2.45E-03 | 2.74E-05 | 7.566 | 6.136 |
| Average | 2.39E-03 | 2.57E-05 | | |

Table 4

Summary of the geometric factors for one instrument position (out of 8 for High Side and 6 for Low Side), and energy and angle response for the CODIF instruments deduced from all calibration data.

4. DATA PROCESSING SYSTEM

CIS data can be collected in a variety of modes with different bit-rates: 5527 bit/s in mode NM1 (normal mode), 6521 bit/s in mode NM2 (Ion mode), 4503 bit/s in mode NM3 (Electron mode, the PEACE instruments having more bit than in NM1), 26762 bit/s in BM1 (Normal burst mode), 6546 bit/s in BM2 (WEC/WBB TR mode) and 29456 bit/s in BM3 (Event memory readout). NM1 and BM1 are the normal modes. BM3 is a special mode to dump the instrument scratch memory only.

4.1. ON-BOARD DATA-PROCESSING SYSTEM

Because of the high sensitivity and high intrinsic velocity-space resolution of the CIS instruments, continuous transmission of the complete 3D ion distributions sampled at the full time and angular resolution would require impossibly large bit rates. So, extensive on-board data-processing is a fundamental aspect of the CIS experiment. The CIS flight software has been designed to meet the scientific requirements of the mission even in limited transmission bit-rate allocation conditions.

First, the instrument data system (DPS) controls the operation and data collection of the two CODIF and HIA instruments, formats the data for the telemetry channel, and receives and executes commands. In addition, the DPS analyses and compresses on-board the tremendous amount of data to maximise the scientific return despite the limited CIS telemetry allocation. The DPS and the CODIF instrument are integrated in one box called CIS-1 and HIA is integrated in another box called CIS-2.

The first stage in the reduction of the CODIF data is to classify the data by species and position, and then to sum the counts in each mass/angle bin in an incrementing memory accumulator. The species determination is done by comparing the time-of-flight value of an event with a set of thresholds stored in a look-up table. There are 5 thresholds stored for each energy step, corresponding to a low threshold for H^+ and He^{++} , threshold between He^{++} and He^+ , a top threshold for He^+ , and a low and a high threshold for O^+ . An example of the threshold locations over a range of energies is shown in Figure 16. These accumulated counts are the input to both the moment calculation and to the transmitted distribution functions.

4.1.1. Moments

Moments of the distribution functions measured by the analysers are computed by the DPS and continuously transmitted with maximum time resolution (1 spin period or 4 s) for CODIF (for four masses) and HIA instruments. These moments include particle density N_i (including partial densities over several energy ranges for CODIF, and sunward and anti-sunward densities for HIA), the three components of the flow vector V_i , the six unique components of the momentum flux tensor, and the ion heat flux vector. From these, the full pressure tensor can be deduced as well as the temperature anisotropies $T_{//}/T_{\perp}$. Full 4π space coverage of the

analysers and their clean response function guarantee a high accuracy for the on-board computed moments. To calculate moments, integrals over the distribution function are approximated by summing products of measured count rates with appropriate energy/angle weighting over the sampled distribution.

Besides instrument sensitivity and calibration, the accuracy of computed moments is mainly affected by the finite energy and angle resolution, and by the finite energy range. The requirement on instrumental accuracy is best demonstrated in the measurements of mass flow through the magnetospheric boundary and in the computation of the current density in current layers like the magnetopause and the Flux Transfer Events (FTEs). Directional errors in the bulk velocity of less than 2° and relative errors less than 5 % in the product of bulk velocity times number density of the different species are highly desirable. As for the mass flow, quantitative tests of other conservation laws (stress and energy balance) require measurements of plasma moments with uncertainties less than 5 %. Paschmann *et al.* (1986) tested the capability of the AMPTE/IRM plasma instrument in a simulation study. For parameters typically observed in high-speed flow events, the simulation shows that density, velocity, temperature and pressure are accurately measured to within 5 %. With the better azimuthal coverage and resolution of the CIS instruments, improved accuracy (in comparison to AMPTE/IRM) of the plasma moments was expected by Martz, 1993. The accuracy requirements concerning the analysis of two- and three- dimensional current structures as well as shear and vortex flows, i.e. measurements strongly related to the four spacecraft aspect, are fulfilled by the capability of the instrument, as it is demonstrated by in-flight measurements.

4.1.2. Reduced distributions

Other reduced distributions, including pitch-angle distributions, averages (over 2 to 5 spin periods) or snapshots of the 3D distributions, can be computed with resolutions dependent upon the specific scientific objectives and telemetry rate. The two-dimensional pitch-angle distribution requires far less telemetry than the full distribution, thus allowing higher time resolution. Pitch- angle distributions can be transmitted when the magnetic field direction (provided on-board by the magnetometer) is in the field of view of the detector.

4.1.3. On-board processing unit

Accomplishing these computations in real time is a heavy processing burden, and requires a sophisticated data system, both in terms of hardware and software. The data system is based on a set of two microprocessors. The main processor, located in the CIS-1 box, interfaces with the spacecraft On-Board Data Handling System (OBDH), the magnetometer, the plasma wave experiments (DWP), and the CIS-2 processor. It is in charge of formatting telemetry data, receiving and executing commands or passing them to the other processor, and controlling the burst memory. It also controls, collects and analyses data from the CODIF. The second processor is included in CIS-2 box and controls, collects and analyses data from the HIA. The main processor is interfaced with the second one by a serial data line; the HIA processor compresses the data so that the serial link can transmit at the highest data rates.

4.1.4. Scratch Memory

The CIS experiment acquires data at nearly the fastest useful rate. In order to store a series of many two- and three-dimensional distributions at full time resolution, a 1 Mbyte memory is included in the instrument, so that discontinuities can be studied in detail. This scratch

memory is read when the spacecraft is in BM3 telemetry mode, or in NM1 mode 15 (Table VII) when the appropriate flag is set in the software.

4.2. TELEMETRY

4.2.1. Data Products

Tables V and VI give HIA and CODIF scientific telemetry products, respectively. Products consist of on-board computed moments, one-, two- and three-dimensional distributions and pitch-angle distributions. The high flexibility in selecting data products to be transmitted at a given period depends upon the telemetry mode, bit rate sharing between CIS-1 and -2, and of course of the plasma environment; energy, angle, and time resolutions can be optimised to extract maximum information relevant to the scientific objectives. Data format changes are programmed within the instrument and do not require any reformatting of the spacecraft or ground data systems.

Table V. HIA scientific telemetry products

| HIA SCIENTIFIC TELEMETRY PRODUCTS | | | | | |
|---|--------------------|--|--------------------------|----------------------|--------------|
| Quantity | Product no. | Accum. Size | Basic Time (spin) | Total (bits) | bit/s |
| I. HOT POPULATIONS (large geometrical factor section) | | | | | |
| Moments 3Df(n,3v,6P,3H) | P2 | 468 words 16 spins 1 packet | 1 | 468 x 16 + 32 | 117.5 |
| Hot 3D Max Resolution (Large G Section) 62E x 8q x 16f | P5 | 3968 words 4 packets | 1 | 63488 + 192 | 15920 |
| 3D 31E x 88W | P6 | 1364 words 2 packets | 1 | 21824 + 96 | 5480 |
| 3D 31E x 42W | P7 | 651 words 1 packet | 1 | 10416 + 48 | 2616 |
| 1D 62E | P9 | 8 spins 1 packet | 1 | 496 x 8 + 32 | 125 |
| 1D 31E | P18 | 8 spins 1 packet | 1 | 248 x 8 + 32 | 63 |
| 2D Azim. Distribution (integrated over polar angles) 31E x 16f | P10 | 496 words 2 spins | 1 | 3968 x 2 + 48 | 998 |

| | | | | | |
|--|--------------------|--------------------------------|-------------------|-------------------------------|--------------|
| 2D Polar Distribution (integrated over azim. Angles) 31E x 16q | P11 | 496 words 2 spins | 1 | 3968 x 2 + 32 | 996 |
| 2D Polar Distribution 31E x 16q for 3 sectors (solar wind, antisolar and flanks) | P20 | 1488 words 2 spins | 1 | 11904 x 2 + 32 | 2976 |
| 2D Pitch Angle Distrib. Cut (2 slices/spin when <i>B</i> is in the field of view) 31E x 16q x 2 slices | P12 | 496 words 1 spin | 0.5 x 2 | 3968 x 2 + 48 | 1996 |
| | P19 | 2 spins | 1 | 3968 x 2 + 64 | 1008 |
| 3D 16E x 88W | P15 | 704 words 1 packet | 1 | 11264 + 48 | 2828 |
| 3D 30E x 88W | P16 | 1320 words 2 packets | 1 | 21120 + 96 | 5304 |
| 3D 62E x 88W | P17 | 2728 words 3 packets | 1 | 43648 + 144 | 10948 |
| 3D 31E x 8q x 16f (*) | P21 | 1984 words 2 packets | 1 | 31744 + 96 | 7960 |
| 3D 31E x 8q x 16f compressed (**) | P23 | 992 words 2 packets | 1 | 15872 + 5 x 2 x 16 | 4008 |
| II. COLD POPULATIONS - SOLAR WIND (small geometrical factor section) | | | | | |
| Cold moments for solar wind 2DE (n,3v,6P,3H) | P4 | 156 words 16 spins | 1 | 312 x 16 + 16 x 18 | 82.5 |
| 3D 31E x 8q x 8f (cold 3D) | P8 | 992 words 1 packet | 1 | 15872 + 32 | 3976 |
| 2D Cold Azim. Distrib. (q integration) 31E x 8f (5.6° each) | P13 | 496 words 4 spins | 1 | 1984 x 4 + 32 | 498 |
| 2D Cold Polar Distrib. (f) integration) 31E x 8q (5.6° each) | P14 | 496 words 4 spins | 1 | 1984 x 4 + 32 | 498 |
| 3D 31E x 8q x 16f (*) | P22 | 1984 words 2 packets | 1 | 31744 + 32 | 7944 |
| 3D 31E x 8q x 16f compressed (**) | P24 | 992 words 1 packet | 1 | 15872 + 4 x 16 | 3984 |
| Quantity | Product no. | Accum. Size | Basic Time | Total (bits) | bit/s |

| | | | | | |
|-----------------------------------|------------|----------|----------|-------------------|-------------|
| | | | (spin) | | |
| III. PROM PRODUCTS | | | | | |
| PROM HIA Sweep Diagnostics | P0 | 1 | 1 | 1024 + 32 | 264 |
| PROM HIA 48C, 32E | P1 | 1 | 1 | 12288 + 32 | 3080 |
| IV. VARIOUS PRODUCTS | | | | | |
| HIA Memory I/O Read | P61 | 1 | - | 32 + 32 | 16 |
| HIA Memory Dump | P62 | 1 | - | 4112 + 32 | 1036 |

ϕ : azimuthal angle Packet header: 2 x 16 bits = 32 bits
 θ : polar angle Frame Header: 9 x 16 bits = 144 bits / 5.1522 sec
 Ω : solid angle (duration independent of the TM mode)
 1 word = 16 bits
 *: calibration products
 **: compression ≥ 2 (2.5 should be expected; 2 assured)

For example HIA produces typically a data volume of 32 polar sectors times 62 energies times 32 azimuth sectors, 16 bit-words, sampled in one spin period (4s). Such a very high data rate has to be handled by a real-time operating system in order to elaborate and compress data to a few kbit s⁻¹ telemetry stream output. All information is transmitted as log-compressed 8-bit-words, except moments which are transmitted with 12 bits. Pitch-angle distributions are instantaneous measurements when **B** is in the field of view of the instruments, and typical full 3D distributions are reduced to 88 Ω (solid angles) by taking into account oversampling in the polar regions.

Table VI. CODIF scientific telemetry products

| CODIF SCIENTIFIC TELEMETRY PRODUCTS | | | | | |
|--|-------------|-----------------------|--------------------------|------------------------------------|------------------------------------|
| Quantity | Product no. | Packet number s | Basic Time (spins) | Total (bits) | bit/s |
| I. HOT POPULATIONS | | | | | |
| Moments 3DE(n,3v,6P,3H) x 4M | P7 | 1 | 1 | 1872 + 32 | 476 |
| 3D 64M x 8E x 6W <i>(6W : 2 polar, 4 perpendicular)</i> | P11 | 2 | 2 | 24576 + 64 | 3080 |
| 3D protons 1M x 16E x 88W | P12 | 1 | 1 | 11264 + 32 | 2824 |
| 3D protons 1M x 31E x 88W | P13 | 2 | 1 | 21824 + 64 | 5472 |
| 3D protons 1M x 31E x 24W | P14 | 1 | 1 | 5952 + 32 | 1496 |
| 3D He⁺⁺ 1M x 16E x 88W | P15 | 1 | 1 | 11264 + 32 | 2824 |
| 3D He⁺⁺ 1M x 31E x 88W | P16 | 2 | 1 | 21824 + 64 | 5472 |
| 3D He⁺, O⁺ 2M x 16E x 88W | P17 | 2 | 1 | 22528 + 64 | 5648 |
| 3D He⁺, O⁺ 2M x 31E x 88W | P18 | 4 | 1 | 43776 + 128 | 10944 |
| 3D He⁺ 1M x 16E x 88W | P32 | 1 | 1 | 11264 + 32 | 2824 |
| 3D O⁺ 1M x 16E x 88W | P33 | 1 | 1 | 11264 + 32 | 2824 |
| 3D He⁺ 1M x 31E x 88W | P34 | 2 | 1 | 21824 + 64 | 5472 |
| 3D O⁺ 1M x 31E x 88W | P35 | 2 | 1 | 21824 + 64 | 5472 |
| 2D 4M x 31E x 16f* | P19 | 1 | 1 | 15872 + 32 | 3976 |
| 2D 2M x 16E x 16f (protons + He⁺⁺)** | P21 | 1 | 1 | 4096 + 32 | 1032 |
| or 4M x 16E x 8f ** | P20 | 1 | 1 | 4096 + 32 | 1032 |
| 2D protons 1M x 31E x 32f | P22 | 1 | 1 | 7936 + 32 | 1992 |
| 2D PAD Cut 4M x 16E x 8q <i>(2slices/ spin when B is in the field of view)**</i> | P23 | 1/slice | 0.5 | 4096 x 2 + 2 x 32 | 2064 (1032/slice) |
| 2D PAD Cut 4M x 31E x 8q <i>(2slices/ spin when B is in the field of view) *</i> | P24 | 1/slice | 0.5 | 7936 x 2 + 2 x 32 | 3984 |
| Monitor Counting Rates 18 signals x 16E x 16f | P27 | 8 | 32 spins | 36864 + 256 | 290 |

| | | | | | | |
|--|-----------------|-----------------------|--------------------------|---------------------------------------|-----------------------------|---|
| Live Pulse Height Data (selected events) | P28 | 1 | | 24 x k + 32 every 2 spins k > 1 | Depending of k value | |
| | | | | | | |
| | | | | | | |
| | | | | | | |
| | | | | | | |
| II. RPA MODES | | | | | | |
| RPA diagnostic product | P29 | 4 | 1 spin | 45056 + 256 | 11328 | |
| 3D | 4M x 16E x 88 W | | | | | |
| III. COLD POPULATIONS | | | | | | |
| Cold Populations Moments | P9 | 1 | 1 | 1872 + 32 | 476 | |
| 3DE(n,3v,6P,3H) x 4M | | | | | | |
| | | | | | | |
| Quantity | Product no. | Packet number s | Basic Time (spins) | Total (bits) | bit/s | |
| IV. COMPRESSED PRODUCTS | | | | | | |
| 3D H ⁺ | 1M x 16E x 88W | P39 | 1 | 1 | - | - |
| 3D H ⁺ | 1M x 31E x 88W | P40 | 2 | 1 | - | - |
| 3D H ⁺ | 1M x 31E x 24W | P41 | 1 | 1 | - | - |
| 3D He ⁺⁺ | 1M x 16E x 88W | P42 | 1 | 1 | - | - |
| 3D He ⁺⁺ | 1M x 31E x 88W | P43 | 2 | 1 | - | - |
| 3D He ⁺ /O ⁺ | 2M x 16E x 88W | P44 | 2 | 1 | - | - |
| 3D He ⁺ /O ⁺ | 2M x 31E x 88W | P45 | 4 | 1 | - | - |
| 3D He ⁺ | 1M x 16E x 88W | P46 | 1 | 1 | - | - |
| 3D O ⁺ | 1M x 16E x 88W | P47 | 1 | 1 | - | - |
| 3D He ⁺ | 1M x 31E x 88W | P48 | 2 | 1 | - | - |
| 3D O ⁺ | 1M x 31E x 88W | P49 | 2 | 1 | - | - |
| V. BURST PRODUCTS | | | | | | |
| Burst Memory Counters | P36 | 16 | 1 | (16384 + 32) x 16 | 65664 | |
| Burst Status | P37 | 1 | 1 | 448 + 32 | 120 | |

| | | | | | |
|--|------------|----------|----------|-------------------|-------------|
| Burst Trigger | P38 | 1 | - | 2912 + 32 | 736 |
| VI. VARIOUS PRODUCTS | | | | | |
| PROM product. Sweep Diagnostics | P0 | 1 | 1 | 4096 + 32 | 1032 |
| PROM product. 48C, 32E | P1 | 1 | 1 | 12288 + 32 | 3080 |
| PROM product. 2 x 18C, 32E | P2 | 1 | 1 | 9216 + 32 | 2312 |
| PROM/EEPROM product. Raw events | P3 | 1 | 1 | 16384 + 32 | 4104 |
| PROM product. Full events | P4 | 1 | 1 | 16384 + 32 | 4104 |
| PROM/EEPROM prod.WEC IEL data | P5 | 1 | 1 | 512 + 32 | 136 |
| PROM/EEPROM prod.FGM IEL date | P6 | 1 | 1 | 4096 + 32 | 1032 |
| Memory I/O Read | P61 | 1 | - | 32 + 32 | 16 |
| Memory Dump | P62 | 1 | - | 4112 + 32 | 1036 |

ϕ : azimuthal angle (spin phase angle)

θ : polar angle

Ω : solid angle

β : near 90° pitch angles (the highest possible angle)
for gyrotropic distributions (for 4 high energies)

4M: protons, a + 2 other masses

* best possibility

** basic use

(*) possibility to have different time of
resolution for the different masses

Packet Header: 32 bits

Basically, for HIA, the high-sensitivity section has full 180° coverage and hot population data are computed using data from this section. When there is a cold population like the solar wind, data products are provided by the small geometrical factor, but the rest of the spin (360° - 45°) is not ignored; data are taken and transmitted. Data from the large geometric factor section are also taken and transmitted.

For CODIF, 4M stands for the four major species : H^+ , He^{++} , O^+ and He^+ . 64M 3D distributions can be read out at a slow rate. They give more detailed information about the presence of minor species. 4M, 88Ω (solid angles), 3D distributions should be read out as often as possible, after all the other data types have been accommodated. A priority scheme for the time resolution is given according to the abundance of the species:

H^+ highest resolution,

He^{++} or O^+ highest resolution or slower by a factor of 2,

He^+ or other species factor of 2 or factor 4 slower.

4.2.2. Data Compression

A linear compression scheme is implemented as a part of the on-board CIS software, which allows the possibility to transmit compressed 3D distributions more often. The compression factor can be adjusted by setting new values to the compression parameters. A number of simulations have proven that a factor of two in the compression factor can easily be reached without any loss of data. The chosen algorithm for this compression is based on the evaluation of the dispersion of the maximum of a Data Block around the average of the 8 successive

value data block itself. If the maximum (Max) satisfies the following:

$$\text{Max} - k * \sqrt{\text{Max}} < \text{Data Block}_{\text{Average}}$$

where k is an adjustable parameter factor to set the dispersion, the data are assumed to be equal to the $\text{Data Block}_{\text{Average}}$ which is transmitted as representative of the whole Data Block. Otherwise the Data Block length is divided by a factor two and the above inequality is applied until the relation is satisfied or the Data Block length has been reduced to one. If k is assumed to be 0 the compression becomes error-free.

4.2.3. Remote-sensing distribution with CODIF

Close to boundaries a distribution of four angles at 90° pitch-angle (phase 0°, 90°, 180°, 270°) is accumulated for two species (H^+ and O^+) in the four highest energies, by making use of the distinct gradient anisotropies of these ions within about one gyroradius of the boundary.. This allows the boundary motions to be traced. Since no automatic sensing of the boundaries is implemented on Cluster, this data product is included in the telemetry when the satellites are close to the nominal position of the interesting boundaries. Generally, data from the High Side section of CODIF are used, which provides substantial counting statistics at all magnetospheric boundaries. The accuracy of this analysis will be tested using the full 3D distributions during time periods when they are available with the full time resolution in Burst Mode.

4.2.4. CODIF Live Pulse Height data

For each particle CODIF measures the following parameters:

| | | |
|---------------------|---------|------------------------------------|
| Time-of-flight: | 8 bits | (giving 256 values) |
| Azimuthal position: | 5 bits | (32 sectors) |
| Proton on/off: | 1 bit | |
| Energy step: | 7 bits | (one between 128 elementary steps) |
| Pixel number: | 3 bits | |
| Total: | 24 bits | each |

4.2.5. CODIF Monitor Rates

To check the performance and the counting efficiency of CODIF certain monitor rates have to be accumulated and transmitted with the science data:

| | |
|--------------------|------------------------------------|
| 2 Starts | (each time-to-amplitude converter) |
| 2 Coincidences | (each time-to-amplitude converter) |
| 16 Start positions | |
| 4 Stop positions | |

To cut down in bit rate a specific scheme is used by which only every fourth energy step and every eighth sector are transmitted at a time. A cycle is completed after 32 spins.

4.2.6. Telemetry Formats

Instrument science and housekeeping data are read out over a single serial interface; the two types are differentiated by separate word gates. Telemetry is collected as a series of blocks, a fixed number per telemetry frame. Telemetry frames are always 5.152222 s in duration independent of telemetry mode, and are synchronised by a 'Reset' pulse that occurs at the beginning of each frame. Housekeeping data consists of 54 bytes per telemetry frame. Science can be collected in a variety of modes with different bit-rates; these modes are subdivided into

'Normal' and 'Burst' Modes, differentiated by the number of blocks per frame (10 for normal and 62 for burst). The different bit rates for Normal Mode are generated by changing the number of words per block.

BM3 is a special mode to dump the instrument scratch memory only; it is not an ordinary operating mode.

Two contingency modes exist in which all available data go either to CIS-1 (CODIF) or to CIS-2 (HIA).

The four Cluster spacecraft fly through a number of different plasma environments, and there must be a mechanism to change the mode of the instrument with a minimum number of commands when moving from one region to another. The CIS instruments have a large amount of flexibility either in the selection of the operating mode or in the reduction of the data necessary to fit the available telemetry bandwidth. The instrument must be capable of making many changes to the operational details in response to a few commands.

Table VII shows the 16 CIS basic operation modes with the bit-rate sharing between CODIF and HIA, defined for each spacecraft bit-rate mode. The CIS instruments operate in the different regions of the Earth's environment in these 16 operative modes that, for the five telemetry regimes foreseen (forgetting HK and BM3 modes), give a total amount of 80 science data transmission schemes. Each basic scheme corresponds to a given sequence of products, spanning from the moments of the ion distributions to the 3D.

Roughly speaking, all these 16 operative regimes can be grouped into solar-wind tracking oriented modes, solar-wind study modes with the priority on the backstreaming ions, magnetospheric modes, an RPA mode and a calibration mode. Moreover part of these solar-wind and magnetospheric modes are duplicated in a similar mode in which 3D compression is introduced (modes 4, 5, 13, and 14).

For HIA the 16 basic CIS operation modes have also been implemented, mixing basic products defined in Table V. These 16 modes can be grouped in 2 mode families, according to the plasma populations encountered along the Cluster orbit: the so-called (a) 'magnetospheric' modes, and (b) 'solar-wind' modes. In both modes moments are systematically transmitted, computed every spin from the data acquired on the high-sensitive half-hemisphere ('high G' section) when the spacecraft are inside the magnetosphere, and from the attenuated half-hemisphere section ('low g') when the spacecraft are in the interplanetary medium. In this way one of the goals of the mission, i.e. to be able to produce high-resolution (4 s) moments by on-board computation, has been fulfilled for all the listed regimes apart from the calibration mode. The computed moments can be used on-board to drive automatic operative mode changes (when this option has been remotely enabled) to better follow fluctuations which require fast-sensitivity-adapting capabilities or to select the best energy sweep regime to cover the local solar wind distribution. This energy tracing in the solar wind has been successfully tested. The automatic mode change, from magnetospheric to solar wind modes, and vice versa, remains however to be tested.

'Magnetosphere' basic modes stay relatively simple, i.e. the full energy-angle ranges are systematically covered and the different data products (including moments) are deduced from the $62\text{E} \times 88\Omega$ energy solid angle count rate matrices accumulated on the 'high G' section.

| | | | TELEMETRY MODE CIS-2 BITRATE (bps) | | | | TELEMETRY MODE CIS-1 BITRATE (bps) | | | |
|---|--------|---|---------------------------------------|-------|-------|--------|---------------------------------------|-------|-------|--------|
| MODE | | Mode Name | NM1 | NM2 | NM3 | BM1 | NM1 | NM2 | NM3 | BM1 |
| 0 | SW-1 | SOLAR WIND / SW tracking | 1 272 | 1 272 | 1 272 | 7 000 | 4 255 | 5 252 | 3 231 | 19 762 |
| 1 | SW-2 | SOLAR WIND / 3D backstreaming ions | 1 272 | 1 272 | 1 272 | 7 000 | 4 255 | 5 252 | 3 231 | 19 762 |
| 2 | SW-3 | SOLAR WIND / SW tracking | 2 135 | 2 135 | 2 135 | 13 162 | 3 392 | 4 386 | 2 368 | 13 600 |
| 3 | SW-4 | SOLAR WIND / 3D backstreaming ions | 2 135 | 2 135 | 2 135 | 13 162 | 3 392 | 4 386 | 2 368 | 13 600 |
| 4 | SW-C1 | COMPRESSION SW-3 (+3Ds) solar wind tracking | 2 135 | 2 135 | 2 135 | 13 162 | 3 392 | 4 386 | 2 368 | 13 600 |
| 5 | SW-C2 | COMPRESSION SW-4 (+3Ds) backstreaming ions | 2 135 | 2 135 | 2 135 | 13 162 | 3 392 | 4 386 | 2 368 | 13 600 |
| 6 | | RPA | | | | | | | | |
| 7 | PROM | PROM OPERATION | | | | | | | | |
| 8 | MAG-1 | MAGNETOSPHERE 1 | 1 272 | 1 272 | 1 272 | 7 000 | 4 255 | 5 252 | 3 231 | 19 762 |
| 9 | MAG-2 | MAGNETOSPHERE 2 | 2 135 | 2 135 | 2 135 | 13 162 | 3 392 | 4 386 | 2 368 | 13 600 |
| 10 | MAG-3 | MAGNETOSPHERE 3 | 3 124 | 4 148 | 2 135 | 13 162 | 2 403 | 2 373 | 2 368 | 13 600 |
| 11 | MAG-4 | MAG-1 SHEATH/TAIL | 1 272 | 1 272 | 1 272 | 7 000 | 4 255 | 5 252 | 3 231 | 19 762 |
| 12 | MAG-5 | MAG-2 SHEATH/TAIL | 2 135 | 2 135 | 2 135 | 13 162 | 3 392 | 4 386 | 2 368 | 13 600 |
| 13 | MAG-C1 | COMPRESSION MAG-1 + 3Ds | 1 272 | 1 272 | 1 272 | 7 000 | 4 255 | 5 252 | 3 231 | 19 762 |
| 14 | MAG-C2 | COMPRESSION MAG-4 + 3Ds sheath/tail | 1 272 | 1 272 | 1 272 | 7 000 | 4 255 | 5 252 | 3 231 | 19 762 |
| 15 | CAL | CALIBRATION | | | | | | | | |
| NM1: 5527 bit/s (Normal mode) NM2: 6521 bit/s (Ion mode) NM3: 4503 bit/s (Electron mode) BM1: 26762 bit/s (Normal burst mode) BM2: 6546 bit/s (WEC/WBB TR mode) BM3: 29456 bits/s (Event memory readout) | | | | | | | | | | |
| Calibration mode at the beginning and the end of each observation period (Detailed 3D distributions without combination of polar anodes) | | | | | | | | | | |

Table VII. Cluster 2 CIS operations modes

'Solar wind' modes allow a precise and fast measurement (4s) of the ion flow parameters (H^+ , He^{++}). For that, in the solar wind, the sweep energy range is automatically reduced and adapted every spin, centred on the main solar wind velocity by using a criterion based on the H^+ thermal and bulk velocities computed during the previous spin. Moreover, detailed 3D distributions (e.g. for upstreaming ions and/or for interplanetary disturbances) are included in the basic products transmitted to the telemetry.

In both regions, and within the HIA telemetry allocation, a maximum bit rate has been allowed for transmission as often as possible of full size (or reduced) 3D distributions.

Science data packets include a number of data products from both HIA and CODIF in a flexible format. Data are time-tagged in such a way as to allow absolute timing of the data on the ground. The format allows bit rate allocations to the various data products to be changed relatively easily with minimal impact on ground processing. All auxiliary data necessary to analyse the data, such as instrument operational mode and timing information, are included in science data products, as it could be difficult to recombine housekeeping packets with the science packets.

Finally, housekeeping data (81 bit s^{-1}), extensively used during spacecraft development tests, give all the information needed to follow the health and safety of the instrument.

Table VIII shows the scientific products of HIA transmitted nominally in the various telemetry modes.

CIS2: SCIENTIFIC MODES

| MAGNETOSPHERIC MODES | | | | | | HIGH G SECTION | | | | | | | |
|-------------------------|-----------|------|----------|----------------------|-------|----------------|-----|--------------|-----------------|-----------------|-----------------|-----------------|-----------------|
| TELEMETRY MODE | | | | HIA Bit rate (bit/s) | | M | 1D | 2D | | | 3D | | |
| OPERATION MODE | | | | | | P2 | P9 | P10 | P11 | P12 | P6 | P15 | P17 |
| NM1 | NM2/BM2 | NM3 | BM1 | Alloc. | HIA | Mom. | 62E | 2D ϕ AZ | 2D θ POL | 2D α PAD | 31Ex88 Ω | 16Ex88 Ω | 62Ex88 Ω |
| 5527 | 6521/6546 | 4503 | 26762 | | | 117.5 | 125 | 998 | 996 | 1998/1008 | 5480 | 2628 | 10948 |
| MODES 8-11 | | | | 1272 | 1238 | | | | | | | 3 sp | |
| MODES 6-9-12 (& 10 NM3) | | | | 2135 | 2070 | | | | | | 3 sp | | |
| MODE 7 | | | | 2135 | 2112 | | | | | | | | |
| 10 | | | | 3124 | 3071 | | | | | | | 1 sp | |
| | MODE 10 | | | 4148 | 4079 | | | | | 1 sl. | | | |
| | | | 6-7-8-11 | 7000 | 6731 | | | | | 1 sl. | | | |
| | | | 9-10-12 | 13162 | 13062 | | | | | 2 sl. | | | |

| SOLAR WIND MODES | | | | | | HIGH G SECTION | | | | | Low g SECTION | | | |
|------------------|-----------|------|---------|----------------------|-------|----------------|--------------|-----------------|-----------------|-----------------|---------------|-----------------|--------------|-----------------|
| TELEMETRY MODE | | | | HIA Bit rate (bit/s) | | 1D | 2D | 3D | M | 2D | 3D | | | |
| OPERATION MODE | | | | | | P18 | P10 | P20 | P6 | P15 | P4 | P13 | P14 | P8 |
| NM1 | NM2/BM2 | NM3 | BM1 | Alloc. | HIA | 31E | 2D ϕ AZ | 2D θ POL | 31Ex88 Ω | 16Ex88 Ω | M | 2D θ POL | 2D ϕ AZ | 31Ex88 Ω |
| 5527 | 6521/6546 | 4503 | 26762 | | | 63 | 998 | 2976 | 5480 | 2628 | 82.5 | 498 | 498 | 3976 |
| MODE 0 | | | | 1272 | 1275 | | 5 sp | | | | | | | /4 sp |
| MODE 2 | | | | 2135 | 2141 | | | | | | | | | /2 sp |
| | | | MOD 0-6 | 7000 | 6889 | | | | 2 sp | | | | | |
| | | | MODE 2 | 13162 | 12531 | | | | | | | | | |
| MODE 1 | | | | 1272 | 1088 | | | | | 3 sp | | | | /18 sp |
| MODE 3 | | | | 2135 | 2074 | | | | 3 sp | | | /2 sp | | /18 sp |
| | | | MODE 1 | 7000 | 6307 | | | | | | | | | /5 sp |
| | | | MODE 3 | 13162 | 6464 | | | | | | | | | /15 sp |

| COMPRESSION MAGNETOSPHERE | | | | | | HIGH G SECTION | | |
|---------------------------|-----------|------|-------|----------------------|-------|----------------|--------|------------------|
| TELEMETRY MODE | | | | HIA Bit rate (bit/s) | | M | 1D | 3D |
| OPERATION MODE | | | | | | P2 | P9 | P23 |
| NM1 | NM2/BM2 | NM3 | BM1 | Alloc. | HIA | Moments | 1D62 E | 31Ex80x16 ϕ |
| 5527 | 6521/6546 | 4503 | 26762 | | | 117.5 | 124.5 | 3206 [COMP=2.5] |
| MODES 13-14 | | | | 1272 | ~1270 | | | ~ 3 sp |
| | | | 13-14 | 7000 | | | | |

| COMPRESSION SOLAR WIND | | | | | | HIGH G SECTION | | Low g SECTION | | | |
|--|--------------|------|--------|--------------------|-------|---------------------|--------------------|---------------|--------------------|-----------------|------------------|
| TELEMETRY MODES Operation Modes (see Table) | | | | HIA Bit rate (bps) | | 3D | M | 2D | 3D | | |
| | | | | Alloc. | HIA | P6 | P23 | P4 | P13 | P14 | P24 |
| NM1 | NM2 BM2 | NM3 | BM1 | | | 31E x88 Ω | 31Ex80x16 ϕ | M | 2D θ POL | 2D ϕ AZ | 31Ex80x8 ϕ |
| 5527 | 6521 6546 | 4503 | 26762 | | | 5480 | 3206 [COMP=2.5] | 78.5 | 498 | 498 | 1992 [COMP=2] |
| PRIORITY: SOLAR WIND | | | | | | | | | | | |
| MODE 4 | | | | 2 165 | ~1732 | | | | | | |
| | | | MODE 4 | 13162 | ~4844 | | | | | | |
| PRIORITY: UPSTREAMING IONS | | | | | | | | | | | |
| MODE 5 | | | | 2 165 | 2076 | 2 sp. | | | | | /16 sp. |
| | | | MODE 5 | 13162 | | | | | | | /5 spins |

3 sp.: integrated over 3 spins /3 sp.: once every 3 spins 1,2 sl.: 1 or 2 slices

Table 8
CIS 2 Scientific Modes

4.3. PROCESSING UNIT

One of the decisive variables which affects the instrument operation is the telemetry mode; when the telemetry mode changes, the CIS instrument receives a single command and changes accordingly its bit rate allocation and data product collection mechanism to match the available telemetry. Some instrument parameters stay mode-independent and are programmable, such as MCP voltage.

The DPS is made of a small PROM, some EEPROM, and some RAM memories. The non-volatile EEPROM memory contains most of the on-board code and parameter tables, the RAM memory is used primarily to hold data blocks and some operational parameters and the PROM memory contains the bootstrap code needed to load or change the EEPROM. The EEPROM memory cannot be read while it is being programmed, and programming takes several millisecond per block; it contains most of the operational parameters so that they do not have to be reloaded on power-up.

As a basic philosophy the default operational parameters are kept in EEPROM memory, while the current operational parameters are in RAM memory. The telemetry mode independent parameters are copied from the defaults on processor reset (this is called the 'Fixed Table'). The 'Operational Mode Table' is copied from the default table to set up a new mode after commanding. Sometimes it may also be desirable to follow automatic operational mode changes based only on science data (e.g. moments) collected by the instrument. The 'Telemetry Allocation Table' is a subset of the Operational Mode default Table; when the telemetry rate changes, the appropriate Telemetry Allocation Table is copied from the default table for the new rate and the current operational mode.

The CIS-1 and CIS-2 instruments have separate tables, but of course are controlled by the same telemetry rate and operation mode commands.

4.4. GROUND SCIENCE DATA PROCESSING

The CIS raw telemetry is pipeline-processed at the French Cluster Data Centre at CNES, Toulouse, where CESR-developed software is running. Level-1 and Level-2 data products are thus systematically generated. Level-1 files correspond to decommutated and decompressed data, organised in flat files, in full time resolution, one file per spacecraft-day-data product. Level-2 files are CDF files in physical units, and they include density for the major ion species, bulk velocity, parallel and perpendicular temperature. These files are organised following the Cluster Science Data System (CSDS) recommendations, and they populate two data bases: the Prime Parameter Data Base (PPDB: 4 spacecraft, 4 s resolution) and the Summary Parameter Data Base (SPDB: 1 spacecraft, 1 min resolution). The contents of these data bases are distributed to other National Data Centres on a daily basis. The PPDB are accessible to the whole Cluster community, and the SPDB are public domain. Due to their broad accessibility, and to the quality of their data products, these data bases must permit joint analysis of plasma parameters from several instruments, further enhancing the science return of the Cluster mission. Caveats concerning the limitations of the data are systematically added to the CSDS files, and the users are strongly encouraged to read these caveats prior to any study.

Higher level data processing (Level-3) is performed at the CIS PI and Co-I institutes, using interactive software that reads the Level-1 and Level-2 files, and the calibration files. This

software has been developed at CESR (“CL” software) and at IFSI (“IFSIDL” software); it is modular and object oriented, and has been designed to take into account the data collection pattern specific to each CIS mode.

The health and the performance of the CIS instrument are monitored at various levels, by using files retrieved via the network from the Cluster Data Disposition System (DDS) , both at JSOC and at CESR.

5. FIRST IN-FLIGHT CIS RESULTS

The first CIS instrument tests began early September 2000 in the frame of the commissioning period . This period for CIS ended around January 20, 2001. The commissioning period was scheduled to test and adjust all the models and to test the telemetry products in the different modes, extremely complex for CIS. The scientific measurements had no priority during this period and technical tests can limit the interest of the measurements in some cases.

As a conclusion of this commissioning, 3 CIS instruments are working very well. However, on spacecraft 2, very rapidly, a problem of power consumption appeared showing that something was going wrong on the primary side of the Low Voltage Power Converter. After several tests, a test was tried on October 25, 2000 but after 3 minutes the spacecraft current limiter turned off the CIS instrument. Other tests will be tried later in the mission but the problem seems to be very serious and the probability to recover the spacecraft 2 CIS instrument is small. With 3 spacecraft, CIS instruments are still capable to give important information on the composition, fluxes, velocities, dynamics and temperatures of ions. In connection mainly with FGM, PEACE and RAPID instruments, many new and important results will be obtained with the Cluster mission. However, the loss of the CIS instrument on-board one of the spacecraft of the Cluster mission is very unfortunate and ESA is looking to launch the CIS spare model on a microsatellite to recover the 4 point ion measurements.

5.1 Example of validation of the moment calculations

In Figure 18 is shown an example of outbound magnetopause crossing by the Samba spacecraft on December 19, 2000. In this Figure are shown an Energy-Time spectrogram measured by the HIA sensor, the density calculated on-board by HIA and the waves measured by the WHISPER instrument (P. Decreau, private communication). On the density plot measured by HIA are 3 points showing the electron density deduced from the wave instrument. Before this magnetopause crossing the density was too small to be measured by the wave instrument. In the magnetosheath the agreement is excellent between the 2 instruments.

5.2 Importance of the calibrations

The Cluster PPDB and SPDB data sets (see paragraph 4.4) are created from the moments generated on-board the spacecraft. The calculation depends on the efficiencies of the instrument as a function of energy and angle. These efficiencies change with time due to MCP gain fatigue, so there are times when the correct efficiencies are not being used in the on-board calculation. An example of this is shown in Figure 19, from Jan 31st, 2001. During this time, the efficiencies for CODIF on s/c 3 have changed, but no correction had yet been

implemented. Figure 19 shows the velocities from both HIA and CODIF during a time when the spacecraft was in the outer magnetosphere, and velocities should be low. Below the counting rate of CODIF, for H^+ ions, as a function of the energy, the next three panels show the on-board velocities. The CODIF instrument shows a large velocity of -300 km/s in the Z-direction, while the HIA instrument shows nearly zero velocity. This is the result of the wrong efficiency coefficients in the CODIF on-board calculation. The other 6 panels (bottom) show the velocities calculated using the 3D distribution functions, and correct efficiencies. For each direction, first CODIF is shown, and then HIA. Now the two instruments agree very well, and the Z-velocity from both instruments is close to zero. Times like these will be noted in the "caveats" of the PPDB and SPDB data set. When the on-board moments have problems, a member of the CIS team should be contacted to obtain moments from the 3D distributions.

MCP gain fatigue is a slow irreversible process, but which can be compensated by raising the MCP high voltage. This operation has been performed during the first semester 2001, once for CODIF (s/c 3) and once for HIA (s/c 1 and 3).

5.3 Example of validation of the data compression

In Figure 20 are shown simultaneous CODIF measurements from 01:54 UT to 02:23 UT, on Feb. 23, 2001, for s/c 1 and s/c 3. These measurements are identical on the 2 s/c during this period excepted that CODIF data are not compressed for s/c 3 and are compressed for s/c 1. The data compression works very well. Then, for the same telemetry allocation, if the general results are identical for the 2 s/c, the compressed mode gives a better time resolution and compressed data give access to more detailed structures.

5.4 Example of Central Plasma Sheet measurements on September 30, 2000

The Central Plasma Sheet was crossed only at the beginning of the commissioning phase. On September 30, 2000, CIS was on for the spacecraft 3 and 4 and simultaneous measurements of entry and exit of CPS, on the dusk side, were obtained. Figure 21 shows 4.5 hours of HIA and CODIF measurements with s/c 3 from 02:45 UT to 07:15 UT. During this period IMF B_z was negative and a small substorm was detected around 05:30 UT. In the CPS, fluxes are quite isotropic. Several short CPS excursions are detected before the main entry and around 06:00 UT the spacecraft leaves the CPS before coming back with several fluctuations. Energies are typically between 1 keV and 10 keV. Very similar results are obtained with s/c 4. Details of short entries in the boundary layer and the CPS are shown for the 2 s/c in Figure 22. The general and detailed structures are very similar between the 2 s/c. Figure 23 shows the simultaneous measurements for the event around 03:19 UT. It is not possible to show significant differences between the 2 s/c for this event. However in another example small delay (about 12 seconds) between the 2 s/c can be detected (Figure 24). For the study of the CPS the interdistance between the 2 s/c appears to be a little too small. Two examples of 3D distribution functions measured by CODIF on s/c 3 are shown in Figures 25 and 26. At 03:03:31 UT counterstreaming ions are seen in the sunward and in the antisunward directions (positive and negative V_x) while, at 06:17:23 UT strong sunward directed ions are detected with, in addition, a small slow beam in the V_y, V_z plane.

5.5 The occurrence of a mixed magnetosheath-plasma sheet ion region immediately earthward of the low latitude boundary layer (LLBL).

In this section we study two passes by spacecraft 3 across the dusk flank mid-latitude magnetopause (MP). On one pass (Dec 07, 2000) an extended stagnant mixed ion region was detected. On another pass (Dec 12, 2000) along essentially the same trajectory, the region immediately earthward of the MP / LLBL was the more typical single population hot plasma sheet. The observations were practically identical for s/c 4 on these days.

Figure 27 shows an outbound pass, on Dec 07, 2000, by s/c 3 from the plasma sheet to the magnetosheath, crossing the mid-latitude dusk flank magnetopause. Panels c-e show that the plasma sheet ion distribution before 9:30 UT consists of a single high energy population in both H^+ (panel d) and O^+ (panel e) while the magnetosheath proper (say at 15:00 UT) contains a single colder population. Multiple crossings of the MP / LLBL occurred at 11:15-11:40 UT and 13:45-14:08 UT and these boundary regions are recognized by the presence of tailward flowing mixed magnetosheath - plasma sheet ions (panels c and g). The region of interest here is the 1 hour interval, 10-11 UT, where s/c 3 encountered an extended period (over 2 hours and $2 R_E$ in GSE-y) of mixed low and high energy ions. This region is distinguishable from the MP / LLBL by its stagnant plasma. O^+ is present in the high energy population but absent in the low energy component, indicating that high energy H^+ and O^+ are of magnetospheric origin while the low energy component comes from the magnetosheath. The ion density (panel f) in the mixed ion region ($\sim 3 \text{ cm}^{-3}$) is considerably higher than that of the plasma sheet ($\sim 1 \text{ cm}^{-3}$) while its temperature (panel h) is lower. Finally, the mixed ions were detected when the IMF (panel i-k) was strongly northward (IMF $B_z \sim 5 \text{ nT}$) and the solar wind density was unusually high ($\sim 17 \text{ cm}^{-3}$).

On this day, CIS was operating on s/c 3 and s/c 4. The general features of the mixed ion region are quite similar for the 2 spacecraft. Even with a zoom in time (Figure 28) no significant differences are seen between the 2 spacecraft. This indicates that the mixed-ion region has spatial scales much larger than the spacecraft separation of 650 km.

Figure 29 shows another pass by s/c 3 on Dec 12, 2000 along a similar trajectory. The magnetosheath (say after 15:30 UT) and plasma sheet (before 12:30 UT) properties are typical of these regions and are similar to the Dec 7, 2000 event. However, adjacent to the dusk mid-latitude magnetopause which were crossed multiple times between 12:30 and 15:30 UT, the only mixed ions observed next to the MP were confined to the thin layers of fast flowing LLBL. Immediately earthward of the fast flowing LLBL, the ions encountered by the spacecraft are the typical single-population hot plasma sheet ions, i.e., no stagnant mixed ions were detected. This pass occurred when the IMF B_z was $\sim 0 \text{ nT}$ and the IMF B_y was slightly negative. The solar wind was at its typical $2.5\text{-}3 \text{ cm}^{-3}$ level.

A region of stagnant mixed magnetosheath - plasma sheet ions earthward of the MP / LLBL has been detected by Geotail [Fujimoto et al., 1996; 1998], ISEE-2 [Fuselier et al., 1999], and WIND [Phan et al., 2000]. A stagnant cold and dense plasma region earthward of the fast flowing LLBL may also be related to the region termed the "halo" by Sckopke et al. [1981] and later reported by Williams et al. [1985], although these studies did not reveal whether the ions in the stagnant region are LLBL-like (mixed ions) or plasma sheet-like (single population). None of the previous studies could establish the mixed-ion entry sites or the entry mechanisms. The tendency for these cold dense ions to occur for northward IMF only arose from statistical surveys. [Terasawa et al., 1997].

The two passes presented here were along similar trajectories (with a difference of $2 R_E$ in GSM-z) and in both cases the s/c went from the hot plasma sheet to the magnetosheath, but

one pass detected an extended mixed-ion region while the other did not. The mixed-ion case was detected when the IMF was strongly northward and the solar wind was unusually dense, while IMF $B_z \sim 0$ nT and the density was more typical for the case when the mixed ions were not detected. To reveal whether the IMF, solar wind density or other factors determine the presence or absence of a mixed-ion region earthward of the MP/LLBL requires a comprehensive survey of CLUSTER crossings of the flank magnetopause regions. The detection of consecutive regions of the magnetosheath, MP/LLBL and the stagnant mixed ions on Dec 07, 2000 suggests that the entry site must be at the dusk magnetopause. Finally, the spatial extent of the mixed ion region, which is presently not known, can be determined by CLUSTER multi-point measurements when the s/c separation is sufficiently large (2000 km).

5.6 Example of measurements in the magnetosheath and the solar wind (January 24, 2001)

On January 24, 2001 there is a very interesting case of 3 s/c simultaneous measurements, CIS instrument on s/c 1 having been commissioned some days before. Figure 30 shows HIA measurements on s/c 1 and 3 between 01:00 UT and 08:00 UT. The 2 HIAs are in the magnetosphere mode until about 05:55 UT; then they shift to solar wind mode. In magnetospheric mode, the solar wind is clearly identified by unidirectional and monoenergetic ions while in the magnetosheath the distribution is larger in energy and in angle. In solar wind mode the solar wind is detected on small g side but not on the large G side (the high voltage is truncated in this mode to avoid MCP fatigue) while the magnetosheath ions are detected by the large G side. Multiple bow shock traversals are detected. Figures 31 and 32 present a very interesting 3 s/c effect. Between 05:40 and 05:55 UT the results of CODIF (H^+ counting rate, densities and velocities) show ion gyroradius effects seen at the entry for the 3 s/c around 05:40 UT and at the exit for s/c 1 and 3 near 05:47 UT. The entry near 05:40 UT (Figure 31) is detected first by s/c 4 then by s/c 1 and slightly after by s/c 3. Near 05:47 UT s/c 1 and 3 emerge from the bow shock while s/c 4 remains downstream of the shock all the time. These results are consistent with the geometry of the 3 s/c at this time. So s/c 4 is a little nearer of the Earth; it is the first to go into the magnetosheath and stays inside during all this event while the 2 other spacecraft enter the magnetosheath later and exit, being near the shock as seen between 05:47 and 05:55 UT before returning to the magnetosheath. Thus the morphology is very stable and the s/c configuration enters and exits in formation, like into and out of a fixed stable boundary. This example shows the large interest of multispacecraft measurements.

5.7 Example of cusp measurements (Feb 19, 2001)

On Feb 19, 2001, the Cluster spacecraft have flown into the cusp before going to the magnetosheath. Figure 33 shows HIA data on s/c 1 and s/c 3 between 01:00 and 04:30 UT. The general features are quite identical between the 2 s/c. For the same time interval the H^+ and He^{++} CODIF data for s/c 1, 3, and 4 are shown in Figure 34. Note there is a change of sensitivity for CODIF at 02:15 UT on s/c 4 (from High Side to Low Side measurements). A zoom of the H^+ data is shown in Figure 35 between 01:00 and 01:20 UT.

At 01:05, after having passed the near tail lobes, Cluster spacecraft entered the mid-altitude cusp, where is clearly seen a plasma of magnetosheath origin. Energy distributions and ion composition (H^+ and He^{++}) of CODIF data strongly differ between the cusp and the day side plasma sheet (Figure 34) the cusp being characterized by the significant presence of the He^{++} ions. This latter region was encountered between 02:20 and 02:50, and occasionally between

03:00 and 03:20 before the entry of the spacecraft in the magnetosheath.. There is a small delay between s/c 3, first entering the cusp, the s/c 1 then the s/c 4 in agreement with the geometry of the spacecraft tetrahedron (from OVT, not shown); s/c 1 and s/c 4 are however relatively closer and the time difference between these 2 spacecraft is small.

During the main mid-altitude cusp traversal (01:05 to 02:20), many injection and time/energy dispersed structures can be seen, looking like the "Cusp Ion Steps" studied by Lockwood and Smith (1992). In Figure 36 is shown a GSE distribution function from CODIF H^+ measurements. This Figure shows both incoming/downflowing and reflected/upflowing ion populations as expected in the mid-latitude cusp. Its apparent D-shaped structure (Cowley, 1982) may not be a sign of reconnection at the dayside magnetopause. Indeed, it is reversed in V_z component (assuming \mathbf{B} field lies roughly in the $-\mathbf{z}$ direction) compared to what would be expected for such a reconnection signature (see also Smith and Lockwood, 1996).

Since the IMF is clearly oriented southward during the whole interval (not shown), the apparent poleward convection feature (since there is a global increase in particle mean energy during the crossing), added to the previous remarks, leads to a possible occurrence of subsolar reconnection, as first proposed by Dungey. Other examples of reconnection signatures as seen by CIS are presented, in more details, by Bosqued et al. (this issue).

5.8 CIS Observations in the auroral acceleration region

The four Cluster satellites are very useful for studying auroral plasma acceleration processes and plasma sheet dynamics at radial distances 4-6 Earth radii over the nightside south and north auroral zones. Starting from late December 2000 the Cluster orbit pericenter moves into the nightside/tail region, thus allowing data taking within the auroral oval close to the local magnetic midnight. The four Cluster s/c traverse auroral oval field lines consecutively at almost the same magnetic local time, separated in time by about 200 s (s/c1-s/c3).

The CIS team have so far identified over 10 cases of nightside auroral oval traversal by the spacecraft 1, 3 and 4 that contain interesting data on the ionospheric upward acceleration of ions. Ion outflow from the auroral regions is a significant plasma source in the magnetosphere (Chapell, 1998, Kondo et al., 1990, Andre and Yaw, 1997). The four Cluster spacecraft have the unique capability of traversing auroral field lines at almost constant heights above what is statistically conceived the altitude of auroral plasma acceleration. The consecutive traversal makes it possible, for the first time, to study in situ the temporal/spatial evolution of auroral plasma acceleration processes. Some preliminary findings from the CIS data are as follows:

- The upward acceleration of ionospheric ions is quite dynamic, with small and medium scale features varying considerably within 200 s, however,
- the large scale morphology of the upward acceleration region, the large scale "ion inverted V", remains rather constant in the few minutes time scale,
- The field aligned upward acceleration process is clearly mass dependent, heavier ions acquiring higher peak energies.
- Ion acceleration clearly continues in the 4-6 R_E altitude range, mainly by what appears to be transverse heating/acceleration. Instead of focusing with height (due to the magnetic mirror force) the ion beams continues to be broad.
- Downward plasma sheet ion beams are generally seen in the same region as upgoing ion beams. The downgoing beams have higher energies than the upgoing beams, suggesting that they originate from an acceleration region in the tail (Sauvaud et al, 1999; Sergeev et

al., 2000) or, if they originate in the conjugate/opposite hemisphere, this indicates that the ion acceleration process progresses even beyond the altitude of $6 R_E$.

An example illustrating the Cluster spacecraft 1 (Rumba) traversal of the auroral acceleration region is shown in Figure 37. The two color spectrogram in the lowermost panels represent data taken in the solar direction, which in case of Cluster at auroral latitudes near midnight looks close to the magnetic field lines. At the top are ion fluxes measured by HIA in four angular sectors and integrated over the four sectors. The satellite in this case exited the ring current (left), into the auroral oval, and entered the polar cap region (right). Notice the low energy ion structures for both upflowing H^+ and O^+ . In Figure 38 the evolution of upward ion acceleration can be deduced from the 3 s/c measurements, which are in full agreement with the field line geometry given by OVT (Stasiewicz, 2001). Figure 39 shows the position, given by OVT, of the 4 s/c, going in the upward direction, and their magnetic connection to the Earth: s/c 1 is followed by s/c 3, then by s/c 2 and finally by s/c 4: in agreement with this Figure, on Figure 38 s/c 1 is the first arriving in the polar cap followed by s/c 3 and after by s/c 4.

These results fit the general pattern of ionospheric ion acceleration and plasma sheet ion precipitation near the polar boundary of the auroral oval reported from FAST, POLAR and INTERBALL measurements. However, Cluster will be able to determine the characteristic times of the ion acceleration/precipitation processes for the first time.

5.9 RPA measurements.

One example of data obtained in the RPA mode (February 14, 2001) is shown in Figure 40 with CODIF on spacecraft 3. At the top of the Figure, ion fluxes measured by HIA in 4 directions, from 04:00 to 12:00 UT, are shown; at the bottom are shown RPA measurements between 0 and 25 eV/e for the 4 ion species and the ion density deduced from HIA. Low energy H^+ ions are measured mainly between 04:30 and 07:00 UT, then, later, at the entrance in the magnetosheath with RPA measures the low energy part of the H^+ ions. Note, however, that the counting rate scales are very different for HIA and for RPA.

5.10 Influence of ASPOC on the low energy ion measurements

The ASPOC instrument (Riedler et al., 1997) is designed to emit indium ions from a source to control the s/c potential. Effectively, the CIS instrument has seen the positive effect of ASPOC for ion measurements. In the example of Figure 41 are presented the CIS CODIF data obtained on 04 February 2001 for the 3 spacecraft Rumba, Samba and Tango: On Rumba and Samba CODIF is operating on the RPA mode from 14:36 UT to 15:36 UT while on Tango CODIF is operating in the RPA mode from 14:41 UT to 15:41 UT. Then the CIS instruments are operated in a magnetospheric mode. Although during magnetospheric modes the CODIF energy range goes up to about 38 keV/e, the energy scale is limited, on this plot, up to 300 eV, just to focus on the effects on the low energy population. On spacecraft 1 ASPOC is not operating; on spacecraft 3 ASPOC stops emission at 15:19:57 UT and on spacecraft 4 ASPOC stops emission at 17:40:57 UT. The switch-off of the ASPOC beam is clearly observable on the CIS data. On s/c 3 CIS stops to observe low-energy H^+ and He^+ after 15:19:57. On s/c 4 CIS stops to observe them after 17:40:57. The effect is particularly clear on the He^+ population (20 to 70 eV), observed on s/c 4 from about 16:40, and which was never observed on the other two s/c, on which the ASPOC beam was off during that interval. He^+ being a

minority ion species of ionospheric origin, it cannot be detected at these low energies without the s/c potential neutralisation by ASPOC. The effect is also a small effect very clear on s/c 4 at the same time with the decrease of H^+ ion fluxes below 100 eV, when ASPOC is put off. So ASPOC, by lowering the spacecraft potential, has a positive effect for the detection of low energy ions, not normally detected.

6. CONCLUSION

The general characteristics of the two CIS instruments, including scientific performances, weight and raw power, are summarised in Table I. Note that the entrance of each sensor is placed about 10 cm outside the spacecraft platform in order to have an unobstructed field of view and to minimise the effect of the spacecraft potential on the trajectories of the low-energy particles. The two planes of view of CODIF and HIA, mounted on opposite sides of the spacecraft are parallel and tangential to the spacecraft body. The field of view of the two sensors is $15^\circ \times 360^\circ$.

In summary, by their unique features, the CIS instruments provide fast measurements of the major plasma ion species with greatly improved accuracy and resolution. The inherent flexibility of the instrument control allow a permanent optimisation of the scientific operation according to the various situations encountered along the Cluster orbits. The extensive on-board data processing and compression not only improve the time resolution of the measurements and significantly reduce data ground-processing costs, but also make the plasma fundamental parameters available quickly and directly in a usable form to the scientific community.

The first results presented in this paper show that, even with only 3 spacecraft, CIS is able to have in a near future a major contribution at the knowledge of the magnetosphere and its interaction with the solar wind.

7. References

- Andre M. and A.W. Yau, Theories and observations of ion energization and outflow in the high latitude magnetosphere, *Space Sci. Rev.*, **80**, 24, 1997.
- Bosqued J.M. et al., CLUSTER Observation of the High-Latitude Magnetopause and Cusp: First Results from the CIS Ion Instruments, *Ann. Geophys.*, this issue, 2001.
- Burgess D., Cyclic Behaviour at Quasi-parallel Collisionless Shocks, *Geophys. Res. Lett.* **16**, 345, 1989.
- Carlson C.W., et al., An Instrument for Rapidly Measuring Plasma Distribution Functions with High Resolution, *Adv. Space Res.* **2**, 7, 67, 1982.
- Chappell C.R., The terrestrial plasma source: a new perspective in solar-terrestrial processes from Dynamics Explorer, *Rev. Geophys.*, **26**, 4757, 1988.
- Cowley S.W.H., The causes of convection in the earth's magnetosphere - A review of developments during the IMS, *Rev. Geophys. Space Phys.*, **20**, 531, 1982.
- Dungey, J.W., Interplanetary magnetic field and the auroral zones, *Phys. Rev. Lett.*, **6**, 47, 1961.
- Escoubet P.C., R. Schmidt and M.L. Goldstein, Cluster Science and Mission Overview, *Space*

Sciences Review **79**,11, 1997.

Giacalone J., *et al.*, Artificial Spacecraft in Hybrid Simulations of the Quasi-parallel Earth's Bow Shock: Analysis of Time Series Versus Spatial Profiles and a Separation Strategy for Cluster, *Ann. Geophysicae* **12**, 591, 1994.

Gloeckler G., *et al.*: 1993, Detection of Interstellar Pick-up Hydrogen in the Solar System, *Science* **261**, 70.

Fujimoto, M., A. Nishida, T. Mukai, Y. Saito, T. Yamamoto, and S. Kokubun, Plasma sheet entry from the flanks of the near-Earth magnetotail: Geotail observations in the dawnside LLBL and the plasma sheet, *J. Geomag. Geoelectr.*, **48**, 711, 1996.

Fujimoto, M., T. Terasawa, T. Mukai, Y. Saito, T. Yamamoto, and S. Kokubun, Plasma entry from the flanks of the near-Earth magnetotail: Geotail observations, *J. Geophys. Res.*, **103**, 4391, 1998.

Fuselier, S. A., B. J. Anderson, and T. G. Onsager, Electron and ion signatures of field line topology at the low-shear magnetopause, *J. Geophys. Res.*, **102**, 4847, 1997.

Fuselier, S. A., R. C. Elphic, and J. T. Gosling, Composition measurements in the dusk flank magnetosphere, *J. Geophys. Res.*, **104**, 4515, 1999.

Kistler L. M., Cluster CODIF Calibration Report, Part I, II and III, 2000.

Kondo T., B.A. Whalen, A.W. Yau, and W.K. Peterson, Statistical analysis of upflowing ion beam and conic distributions at DE-1 altitudes, *J. Geophys. Res.*, **95**, 12091, 1990.

Lin R.P., *et al.*, A Three-dimensional Plasma and Energetic Particle Investigation for the Wind Spacecraft, *Space Sci. Rev.* **71**, 125, 1995.

Lockwood M., and M.F. Smith, The variation of reconnection rate at the dayside magnetopause and cusp ion precipitation, *J. Geophys. Res.*, **97**, 14841, 1992.

McCarthy M., Cluster 2 CIS RPA Calibration report, 14 March 2000.

Martz C., Spectrométrie Ionique dans la Magnétosphère et le Vent Solaire. Simulation et Précision des Mesures Coordonnées au Moyen des 4 Satellites de la Mission Cluster, Thesis, Paul Sabatier Toulouse University, 1993.

Möbius E., *et al.*, The Time-of-Flight Spectrometer SULEICA for Ions of the Energy Range 5-270 keV/charge on AMPTE IRM, *IEEE Trans. Geosc. Remote Sens.* **GE-23**, 274, 1985.

Möbius E., *et al.*, Direct Observation of He⁺ Pick-up Ions of Interstellar Origin in the Solar Wind, *Nature* **318**, 426, 1985.

Möbius E., *et al.*, Interaction of Interstellar Pick-up Ions with the Solar Wind, *Astrophys. Space Sci.* **144**, 487, 1988.

Paschmann G., *et al.*, The Plasma Instrument for AMPTE IRM, *IEEE Trans. Geosc. Remote Sens.* **GE-23**, 262, 1985.

Paschmann G., *et al.*, The Magnetopause for Large Magnetic Shear: AMPTE/IRM Observations, *J. Geophys. Res.* **91**, 11099, 1986.

Phan, T. D., R. P. Lin, S. A. Fuselier, and M. Fujimoto, Wind observations of mixed magnetosheath-plasma sheet ions deep inside the magnetosphere, *J. Geophys. Res.*, **105**, 5497, 2000.

Quest K.B., Theory and Simulation of Collisionless Parallel Shocks, *J. Geophys. Res.* **93**, 9649, 1987.

Rème H., *et al.*, The Giotto Electron Plasma Experiment, *J. Phys. E: Sci. Instrum.* **20**, 721-731, 1987.

Rème H., *et al.*, The Cluster Ion Spectrometry (CIS) Experiment, *Space Sciences Review* **79**, 303-350, 1997.

Riedler *et al.*, Active Spacecraft Potential Control, *Space Sciences Review* **79**, 271-302, 1997.

Ritter H., Sekundärelektronenemission von Kohlenstoffolien beim Durchgang von Ionen im Energiebereich von 40 bis 500 keV, MPE Report 190, 1985.

Sauvaud J.A. *et al.*, Sporadic plasma sheet ion injections into the high altitude auroral bulge:

satellite observations, *J. Geophys. Res.*, **104**, 28565, 1999.

Scholer M. and Terasawa T., Ion Reflection and Dissipation at Quasi-parallel Collisionless Shocks, *Geophys. Res. Lett.* **17**, 119, 1990.

Scholer M.: Interaction of Upstream Diffuse Ions with the Solar Wind, *Adv. Space Sci.*, 1997.

Sckopke N, G. Paschmann, G. Haerendel, B.U.O. Sonnerup, S.J. Bame, T.G. Forbes, E.W. Hones, Jr and C.T. Russell, Structure of the low-latitude boundary layer, *J. Geophys. Res.*, **86**, 2099, 1981.

Sckopke N., *et al.*, Ion Thermalization in Quasi-perpendicular Shocks Involving Reflected Ions, *J. Geophys. Res.* **95**, 6337, 1990.

Sergeev et al., Plasma sheet ion injections into the auroral bulge: correlative study of spacecraft and ground observations, *J. Geophys. Res.*, **105**, 18465, 2000.

Smith M.F., and M. Lockwood, Earth's magnetospheric cusps, *Rev. Geophys.*, **34**, 233, 1996.

Stasiewicz K., New Methods and Techniques in Visualization and Mapping of Magnetospheric Boundaries, Physical Signatures of Magnetospheric Boundary Layer Processes, J.A. Holtet and A. Egeland editors, Kluwer Academic Publishers, 433-447, 1994.

Stasiewicz K., Orbit Visualization Tool-2 (OVT) for CLUSTER, <http://ovt.irfu.se>, 2001.

Terasawa, T., *et al.*, Solar wind control of density and temperature in the near-Earth plasma sheet: WIND/GEOTAIL collaboration, *Geophys. Res. Lett.*, **24**, 935, 1997.

Trattner K., *et al.*, Statistical Analysis of Diffuse Ion Events Upstream at the Earth's Bow Shock, *J. Geophys. Res.* **99**, 13389, 1994.

Williams D.J., D.G. Mitchell, T.E. Eastman, and L.A. Frank, Energetic particle observations in the low-latitude boundary layer, *J. Geophys. Res.*, **90**, 5097, 1985.

Young D., *et al.*, 2π -radian field-of-view toroidal electrostatic analyzer, *Rev. Sci. Instr.*, **59**, 743, 1988.

Figure Captions

Figure 1. Representative ion fluxes encountered along the Cluster orbit in the solar wind (SW), the magnetopause (MP), the magnetosheath (MSH), the plasma mantle (PM), the magnetosphere (MSPH), the plasma sheet (PS), the lobe and upwelling ions (UPW). The range of the different sensitivities of CIS1/CODIF (Low Side, High Side and RPA) and CIS2/HIA (Low g and High G) are shown with different colors.

Figure 2. Cross-sectional view of the HIA analyser.

Figure 3. Principle of the HIA anode sectoring.

Figure 4. Typical energy (top curves) and angular (bottom curve) resolutions of the HIA analyser (flight model 5), for an energy beam of 800 eV; the energy resolution is about 19.6% and the intrinsic azimuthal resolution is about 6.6°.

Figure 5. Relative transmission of the 16 HIA High G (from 270° to 90°) and 16 HIA Low g (from 90° to -90°) polar sectors (see Figure 3) for FM6 at 5 keV.

Figure 6. Beta sector transmission of HIA for the 4 flight models and the spare model. Results are very similar for the 5 models. Sectors 0-15 corresponds to the High G and 16-31 to the low g. Transmission in sectors 20-27 is divided by 2 as expected from the geometry.

Figure 7. UV effects on a Cluster 1 HIA model (counts/5 sec) in Figure 7a and on a Cluster 2 HIA model (counts/minute) in Figure 7b in function of the polar angle. The background for Cluster 2 has been divided by 2 orders of magnitude by improving the analyser scalloping.

Figure 8. Example of in-flight measurements of HIA on s/c 3 in the Central Plasma Sheet on September 11, 2000. Each rectangle is a θ -F plot, θ , in ordinate, ranges from -90° to $+90^\circ$, F, in abscissa, ranges from -180° to $+180^\circ$, sunward direction being $(\theta, F) = (0^\circ, \pm 180^\circ)$. Each line corresponds to one of the 16 logarithmically spaced energies between 24.3 eV (bottom line) to 34117.3 eV. 10 successive measurements are shown (one by column). There is no sun effect in the detector.

Figure 9. Cross-sectional view of the CODIF sensor. The voltages in the TOF section are shown for a 25 kV post-acceleration.

Figure 10. Geometry of the CODIF RPA.

Figure 11. The CODIF sensor: Schematics (left) and MCP sectoring (right).

Figure 12. Energy sweeping scheme of CODIF in the solar wind. The sweep is shown in $\log E$ versus azimuthal angle for the high-sensitivity section (upper panel) and low-sensitivity section (lower panel), starting at the high energy end. When looking into the solar wind, the sweep stops above the alpha particles for the high-sensitivity section but the sweep does not stop for the alpha particles and the protons for the low-sensitivity section.

Figure 13. CODIF FM7 HS side normalised total efficiency versus total energy for H^+ for the different anodes and with a general fit (upper curve) and CODIF FM7 LS side normalised total efficiency versus total energy for H^+ for the different anodes and with a general fit; HS fit of the upper curve is added (lower curve).

Figure 14. CODIF FM7 HS side normalised total efficiency versus total energy for He^+ for the different anodes and with a general fit (upper curve) and CODIF FM7 LS side normalised total efficiency versus total energy for He^+ for the different anodes and with a general fit; HS fit of the upper curve is added (lower curve).

Figure 15. CODIF FM7 HS side normalized total efficiency versus total energy for O^+ for the different anodes and with a general fit (upper curve) and CODIF FM7 LS side normalised total efficiency versus total energy for O^+ for the different anodes and with a general fit; HS fit of the upper curve is added (lower curve).

Figure 16. CODIF FM7 time-of flight spectra for the four major species at 5 energies. The spectra are averaged over all positions. The vertical lines show the thresholds used to distinguish species.

Figure 17. Example of ion spillover effect in CODIF FM7: fraction of each 4 major ion species detected in the H^+ , He^{++} , He^+ , and O^+ bins.

Figure 18. Comparison of the electron density measured by the Whisper instrument and the ion density measured by HIA, on Dec. 19, 2000 when the s/c 3 leaves the magnetosphere going to the magnetosheath. At the top are the ion fluxes, at the bottom the wave measurements of Whisper and in the middle the density measured by HIA and 3 points

deduced from the Whisper measurements. The agreement is excellent. Before the magnetopause traversal the density is too small to be evaluated by Whisper.

Figure 19. Example showing the importance of the calibrations: from top to bottom: Instrument modes and CODIF and HIA sensitivities, energy-time spectrogram of CODIF for H^+ ions in function of the energy, on-board calculated CODIF and HIA velocities (3 panels), velocities calculated on ground using the 3D distribution functions, and correct efficiencies for HIA and CODIF (6 panels).

Figure 20. Comparison of CODIF compressed data (upper panel) and uncompressed data (lower panel) on Feb 23, 2001: Upper panel gives, for s/c 1, from top to bottom, Telemetry modes, sensitivity and uncompressed energy-time spectrogram H^+ CODIF in 4 directions (top to bottom: sunward, dusk, antisunward and dawn CODIF measurements). Lower panel gives the same results for s/c 3 with compressed counting rates.

Figure 21. CPS and near CPS measurements by the CIS experiment on Sept. 30, 2000, between 02:45 and 07:15 UT, with s/c 3. From top to bottom: HIA telemetry modes and sensitivities, energy-time spectrogram HIA, measured in the sunward, dusk, antisunward, dawn looking directions and integrated over 4 p, CODIF telemetry modes and sensitivities, H^+ and O^+ CODIF energy-time spectrogram integrated over 4 p, on-board and ground calculated ion density, from HIA, and on-board GSE velocity components measured by CODIF.

Figure 22. Simultaneous measurements on Sept. 30, 2000 between 03:00 and 03:30 UT with s/c 3 (CODIF and HIA) and s/c 4 (CODIF). From top to bottom, the upper panel shows, for s/c 3, CIS telemetry modes, the HIA energy-time spectrogram integrated over 4 p, the HIA ion density, on-board HIA GSE velocity components, H^+ and O^+ CODIF energy-time spectrogram integrated over 4 p, H^+ CODIF density and on-board GSE velocity components measured by CODIF. The lower panel shows identical CODIF measurements for s/c 4.

Figure 23. Simultaneous measurements on Sept. 30, 2000 between 03:17 and 03:22 UT with s/c 3 (CODIF) and s/c 4 (CODIF). See caption of Figure 22 for the description of the measurements.

Figure 24. Simultaneous measurements on Sept. 30, 2000 between 06:32:15 and 06:34:55 UT with s/c 3 (CODIF and HIA) and s/c 4 (CODIF). See caption of Figure 22 for the description of the measurements.

Figure 25. CODIF H^+ distribution function (accumulation over 3 spins) in GSE coordinates, on s/c 3, on Sept. 30, 2000 at 03:04:31 UT.

Figure 26. CODIF H^+ distribution function (accumulation over 3 spins) in GSE coordinates, on s/c 3, on Sept. 30, 2000 at 06:17:23 UT.

Figure 27. Dec 7, 2000 magnetopause crossings between 09:00 and 16:00 UT as seen by s/c 3; from top to bottom: Instrument modes, energy-time spectrograms of HIA ions, CODIF H^+ , and CODIF O^+ , HIA density, HIA velocity, and shifted IMF (from ACE, courtesy of N. Ness). The 1 keV CODIF O^+ in the magnetosheath are instrument artifacts due to the contamination from high H^+ fluxes. The 10 keV O^+ are true O^+ counts.

Figure 28. HIA and CODIF measurements on s/c 3 and CODIF measurements on s/c 4, on

Dec 7, 2000 between 13:50 and 14:10 UT. See caption of Figure 22 for the description of the measurements.

Figure 29. Dec 12, 2000 magnetopause crossings between 12:00 and 17:00 UT as seen by s/c 3; from top to bottom: Instrument modes, energy-time spectrograms of HIA ions, CODIF H^+ , and CODIF O^+ , HIA density, HIA velocity, and shifted IMF (from ACE, courtesy of N. Ness). The 1 keV CODIF O^+ in the magnetosheath are instrument artifacts due to the contamination from high H^+ fluxes. The 10 keV O^+ are true O^+ counts.

Figure 30. Measurements of HIA with s/c 1 and s/c 3 on Jan 24, 2001, in the magnetosheath and the solar wind, between 01:00 and 08:00 UT. Upper panel shows HIA measurements with s/c 1 and lower panel HIA measurements with s/c 3. In each panel, from top to bottom: HIA telemetry modes and sensitivities, Low Side (used only in solar wind mode) energy-time spectrogram (integrated over $45^\circ \times 45^\circ$ centered in the solar wind direction), High Side energy-time spectrograms measured in the sunward, dusk, antisunward, dawn looking directions, and density.

Figure 31. Entry in the magnetosheath of s/c 1, 3, and 4 on Jan 24, 2001, between 05:38 and 05:43 as seen by CODIF. The 3 panels show CODIF telemetry modes and sensitivities, energy-time spectrogram integrated over 4 p, density and GSE velocity components. Note that on s/c 4 (lower panel) CODIF is used in low sensitivity mode and the density is correct while on s/c 1 (upper panel) and s/c 3 (middle panel) CODIF is used in high sensitivity mode and the measured densities are not correct due to saturation effects.

Figure 32. CODIF measurements on-board s/c 1, 3, and 4 on Jan 24, 2001, between 05:35 and 05:55. See Figure 31 caption for the details of the measurements

Figure 33. HIA measurements on-board s/c 1 and 3, on Feb 19, 2001, between 01:00 and 04:30 UT. Upper panel shows HIA s/c 1 measurements and lower panel HIA s/c 3 measurements. The 2 panels show from top to bottom: Telemetry modes and sensitivities, energy-time spectrogram measured in the sunward, dusk, antisunward, dawn looking directions, and density.

Figure 34. CODIF measurements on-board s/c 1 (upper panel), 3 (middle panel) and 4 (lower panel), on Feb 19, 2001, between 01:00 and 04:30 UT. The 3 panels show CODIF telemetry modes and sensitivities, H^+ and He^{++} energy-time spectrograms integrated over 4 p, density and GSE velocity components.

Figure 35. CODIF measurements on-board s/c 1, 3 and 4, on Feb 19, 2001, between 01:00 and 01:20 UT. See Figure 34 caption for the details of the measurements.

Figure 36. H^+ ions 3D CODIF measurement, on s/c 3, on Feb 19, 2001, at 01:18:30 UT.

Figure 37. Traversal of the auroral region by s/c 1 on Feb 23, 2001, as seen by HIA and CODIF between 15:15 and 16:15 UT. HIA measurements (upper panel) give telemetry modes and sensitivities, energy-time spectrograms measured in the sunward, dusk, antisunward, dawn looking directions and energy-time spectrogram integrated over 4 p; CODIF measurements (lower panel) give telemetry modes and sensitivities, energy-time spectrogram for upflowing H^+ and O^+ ions, HIA, CODIF H^+ and O^+ densities and GSE velocity components.

Figure 38. CODIF H^+ and O^+ measurements on s/c 1 (upper panel), 3 (middle panel), and 4 (lower panel), on Feb 23, 2001, between 15:50 and 16:15 UT. Each panel shows telemetry modes and sensitivities, energy-time spectrograms for upflowing H^+ and O^+ ions and H^+ and O^+ ion densities.

Figure 39. Positions of the 4 Cluster s/c and geometry of the magnetic field lines deduced from OVT. The 4 s/c are going up; s/c 1 is red, s/c 2 is green, s/c 3 is yellow and s/c 4 is violet.

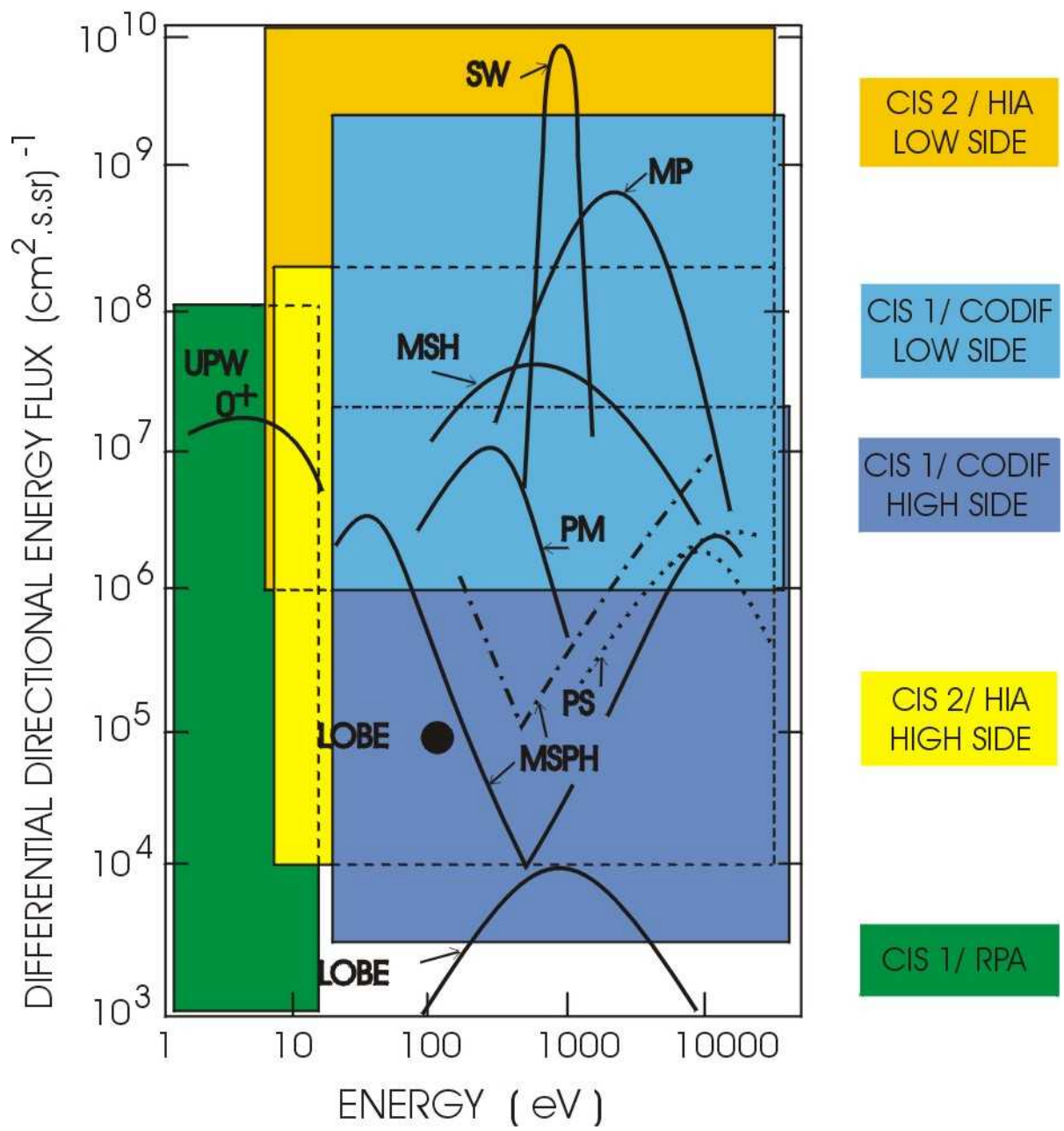
Figure 40. Example of RPA CODIF measurements with s/c 3, between ~ 0 and 25 eV, on Feb 14, 2001, between 04:00 and 12:00 UT. From top to bottom: HIA telemetry modes and sensitivities, energy-time spectrograms measured in the sunward, dusk, antisunward, dawn looking directions and energy-time spectrogram integrated over 4p; CODIF telemetry modes and sensitivities, H^+ , He^{++} , He^+ , and O^+ energy-time spectrogram integrated over 4p, between 1 and 25 eV, HIA and CODIF densities.

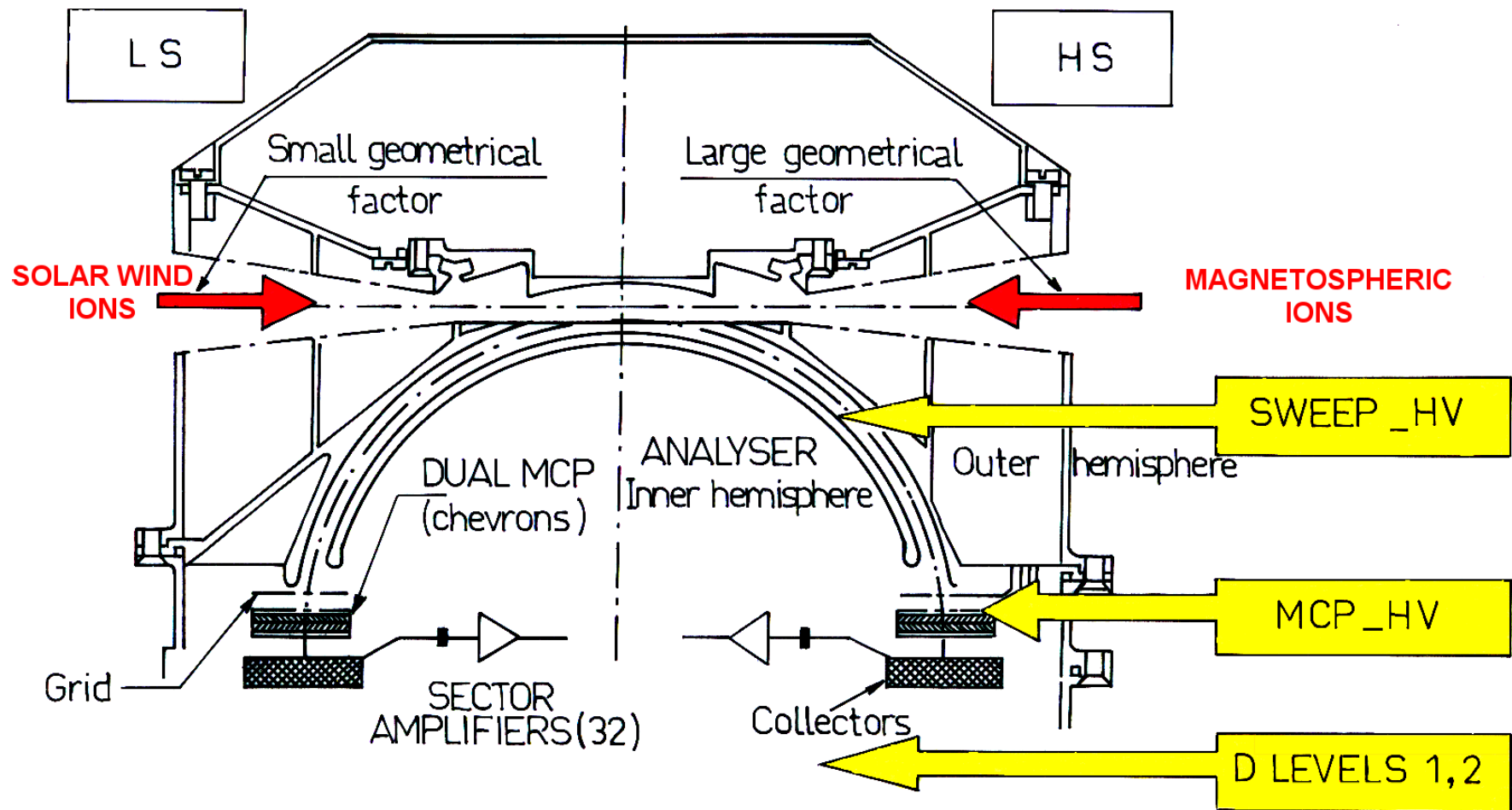
Figure 41. Effect on ASPOC for low energy ion measurements, on Feb. 4, 2001: CODIF energy-time spectrograms, integrated over 4p, for H^+ , He^{++} , He^+ , and O^+ ions on s/c 1, 3, and 4 are shown. On s/c 1 ASPOC does not work; on s/c 3 ASPOC stops at 15:20 UT; on s/c 4 ASPOC stops at 17:41 UT.

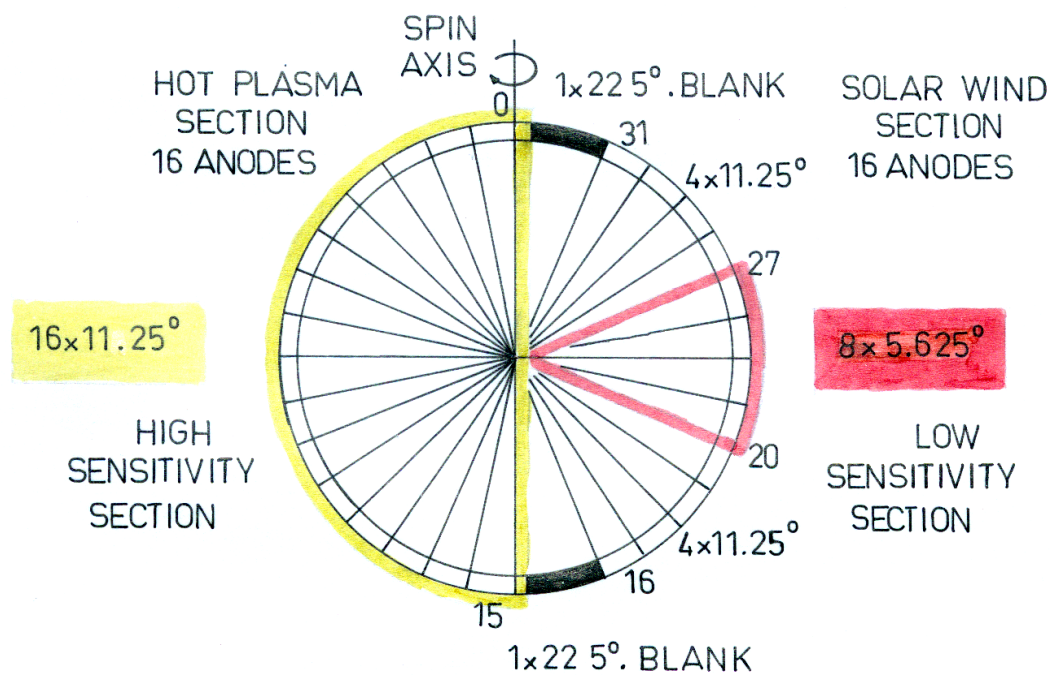
Acknowledgements

Cluster 2 decision was only possible thanks to Dr Roger BONNET, Science Director at ESA. We thank also ESA and DORNIER Project Teams, Starsem and Soyouz/Fregat Teams, ESOC and JSOC. The Cluster 2 CIS instrument was supported by ESA and by many institutions: CESR had the overall responsibility of the instruments, has fabricated the CODIF analyser, DPU CODIF boards, HIA detector, part of HIA electronics and HIA DPU, has participated to the integration, environmental and spacecraft tests and CODIF calibrations, has done the HIA calibrations and data analysis software. UNH has built the CODIF detector, the TOF digital electronics and has participated to the CODIF calibrations. MPE Garching has built the CODIF acceleration high voltage and the CODIF MCP high voltage, the time of flight electronics and the TAC converter. IFSI Roma has built the HIA analyser, part of the HIA electronics, and the HIA flight software. MPAE Lindau has built the CODIF analyser high voltage and the HIA analyser and MCP high voltages. IRF Kiruna has done the lay out of the CODIF DPU boards. SSL at UC Berkeley has done the DPU flight software and the GSE software. UW has done the CODIF RPA calibrations and the CODIF calibrations were done at the University of Bern. At CESR financial support came from CNES grant. The contribution of MPE Garching was supported by ESA under contract 1501073-2400 and by DLR (Deutsches Zentrum fuer Luft und Raumfahrt) under contracts 50 OC 8906 and 50 OC 0102. The high voltage supply of CIS-2 was provided by MPAE Lindau with the support of the Max-Planck-Gesellschaft zur Förderung der Wissenschaften and DARA. For IFSI CIS experiment was supported by Italian Space Agency (ASI). The work at the University of Washington, UNH, LPARL, and UC Berkeley was supported by NASA contract. The Swedish participation was funded by the Swedish National Space Board and the Swiss participation by the Swiss National Foundation and the State of Bern. The authors thank Mrs P. DECREAU for the Whisper data.

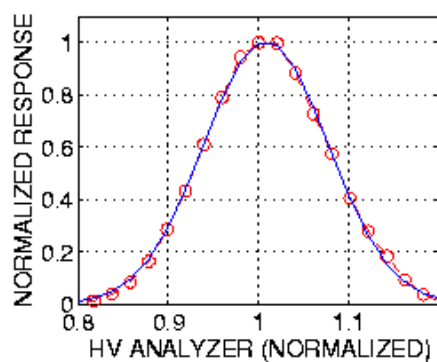
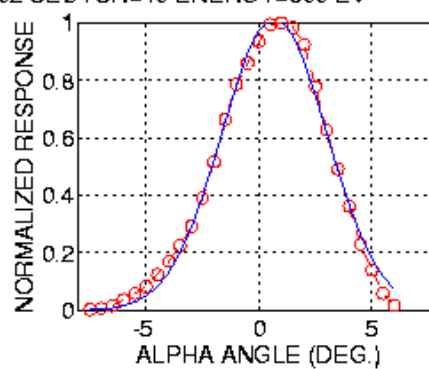
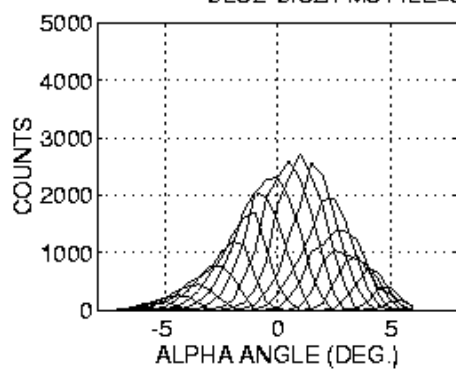
IONS







CLU2-CIS2/FM5 FILE=5a800102 SECTOR=10 ENERGY=800 EV



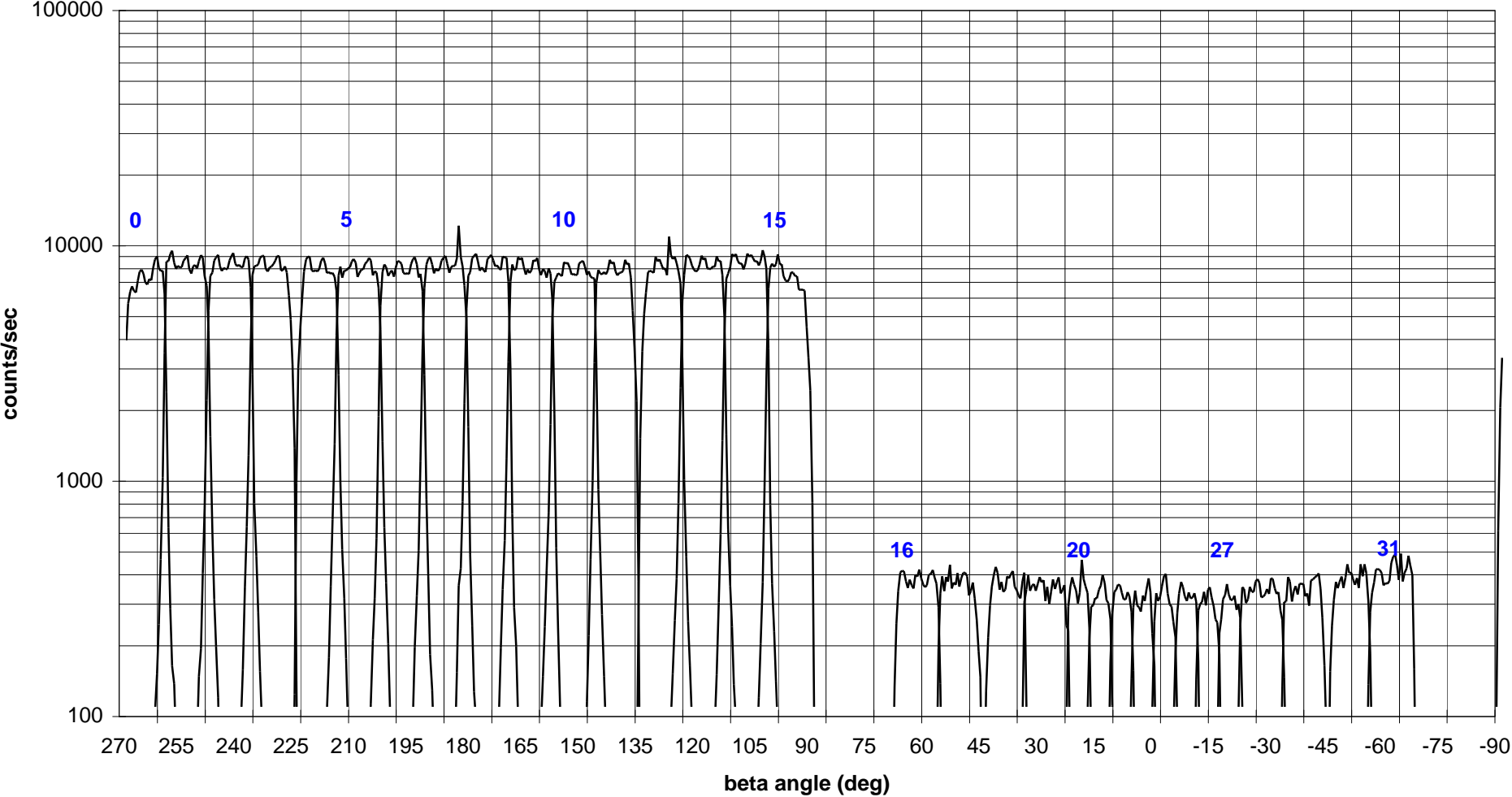
NORM= 1.006
FWHM(E)= 16.27 %
D(E)= 19.55 %
Emax= 1.008
HVmax= 103.8 Volts

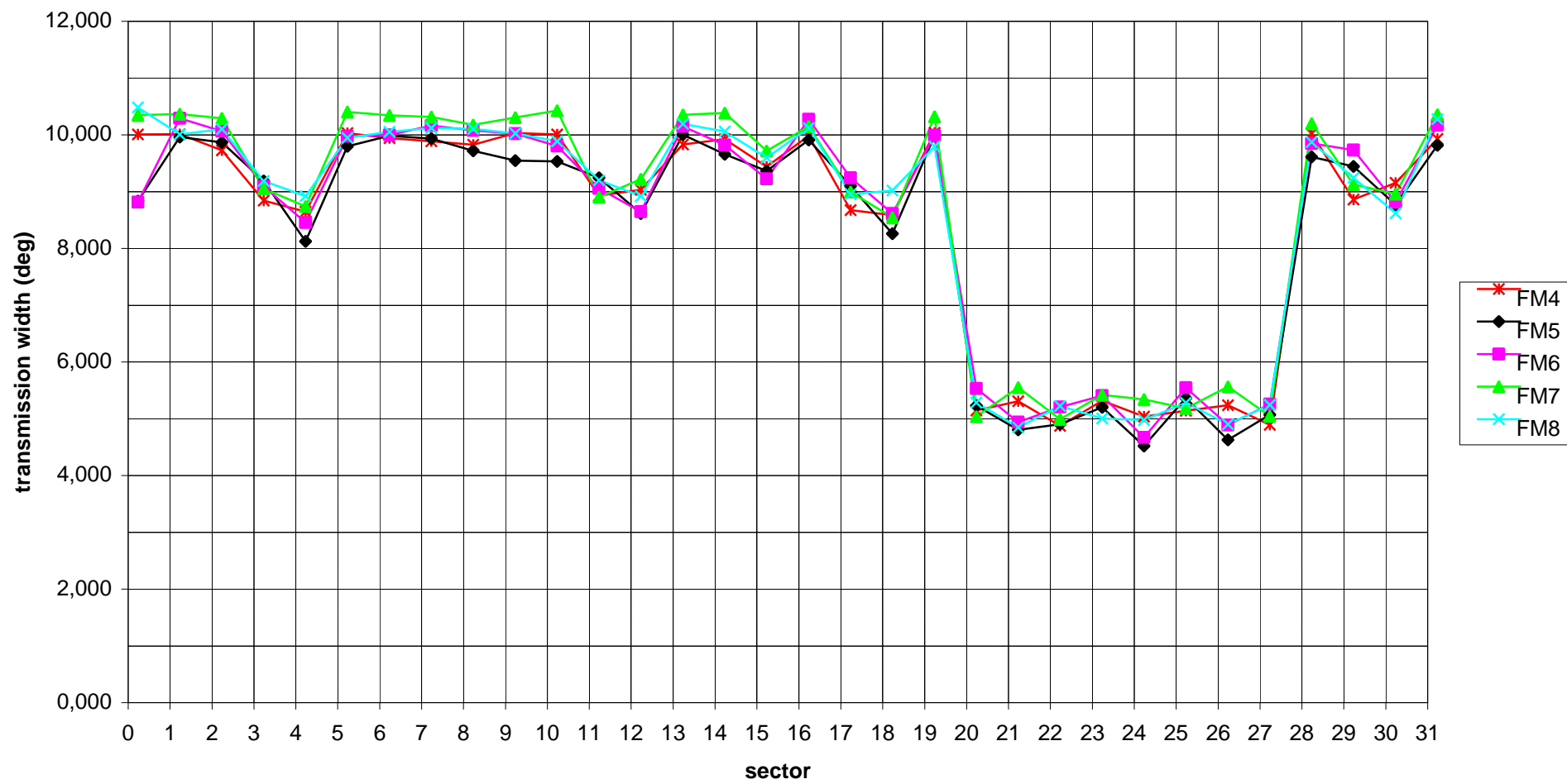
NORM= 1.018
FWHM(A)= 5.466 deg
D(AL)= 6.565 deg
ALmax= 0.6825 deg

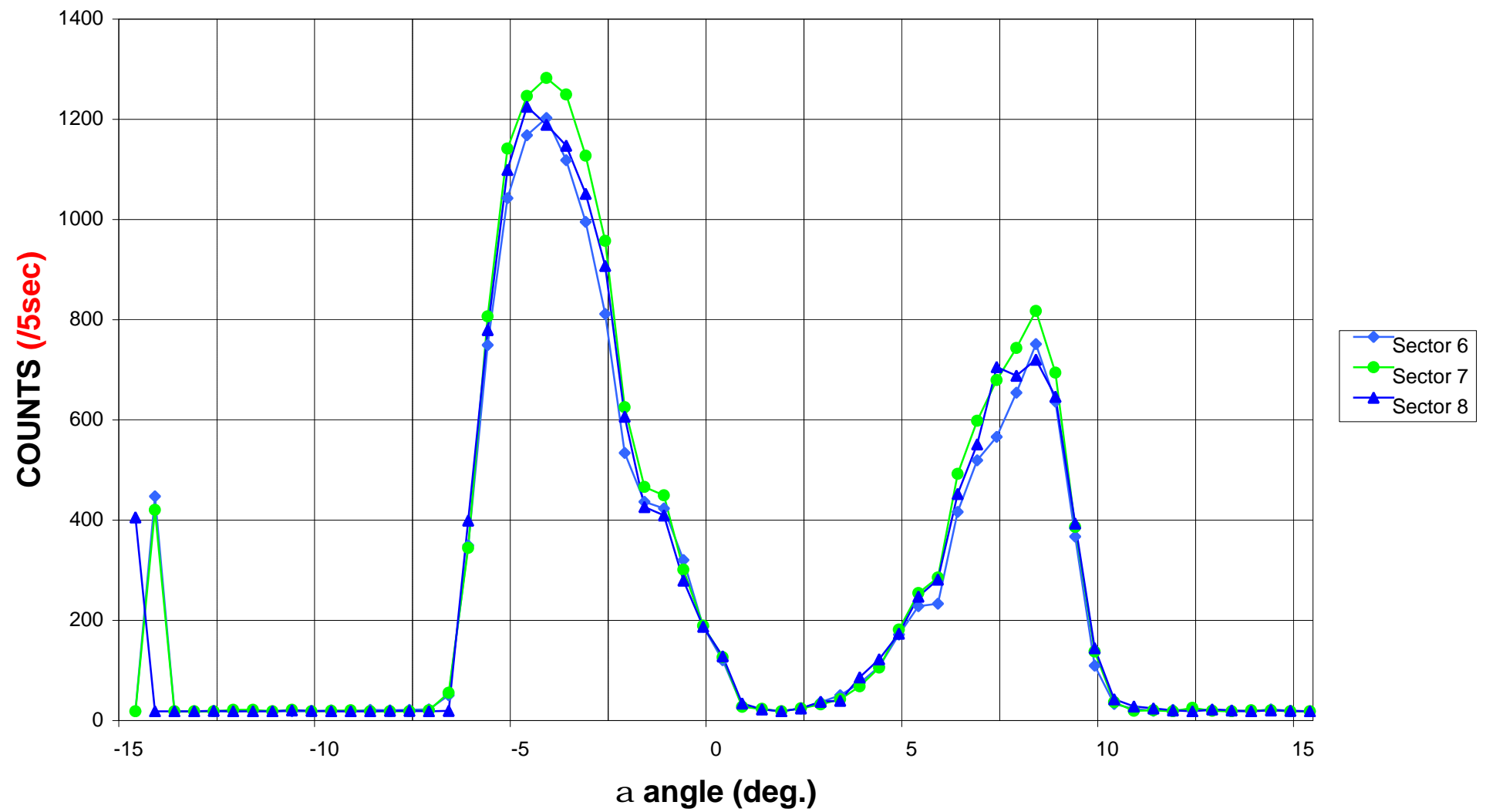
19/05/98

\\matlab\hia\matcis2.m

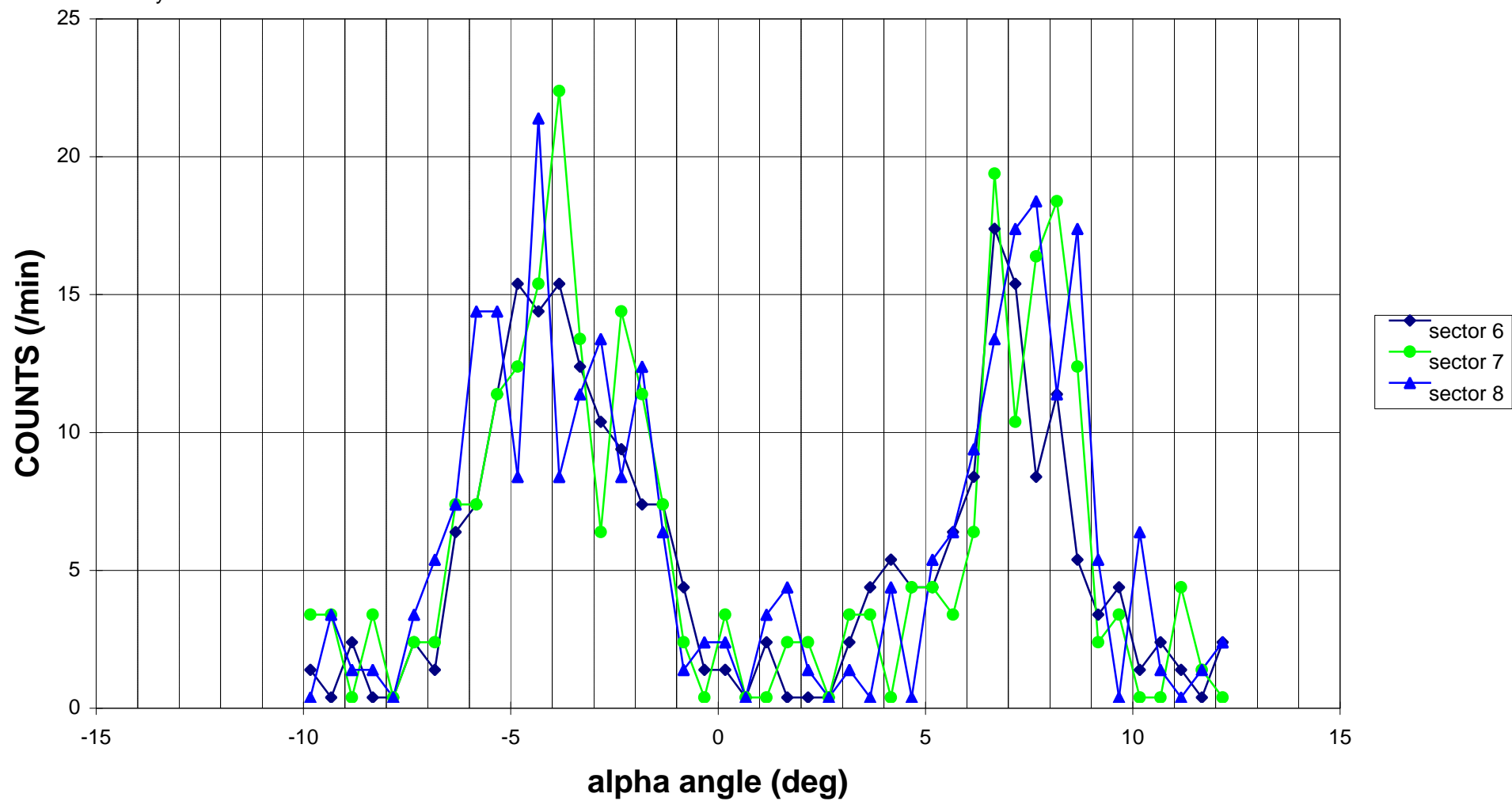
Analyzer HV = 687 volts







Analyzer HV = 0 volts



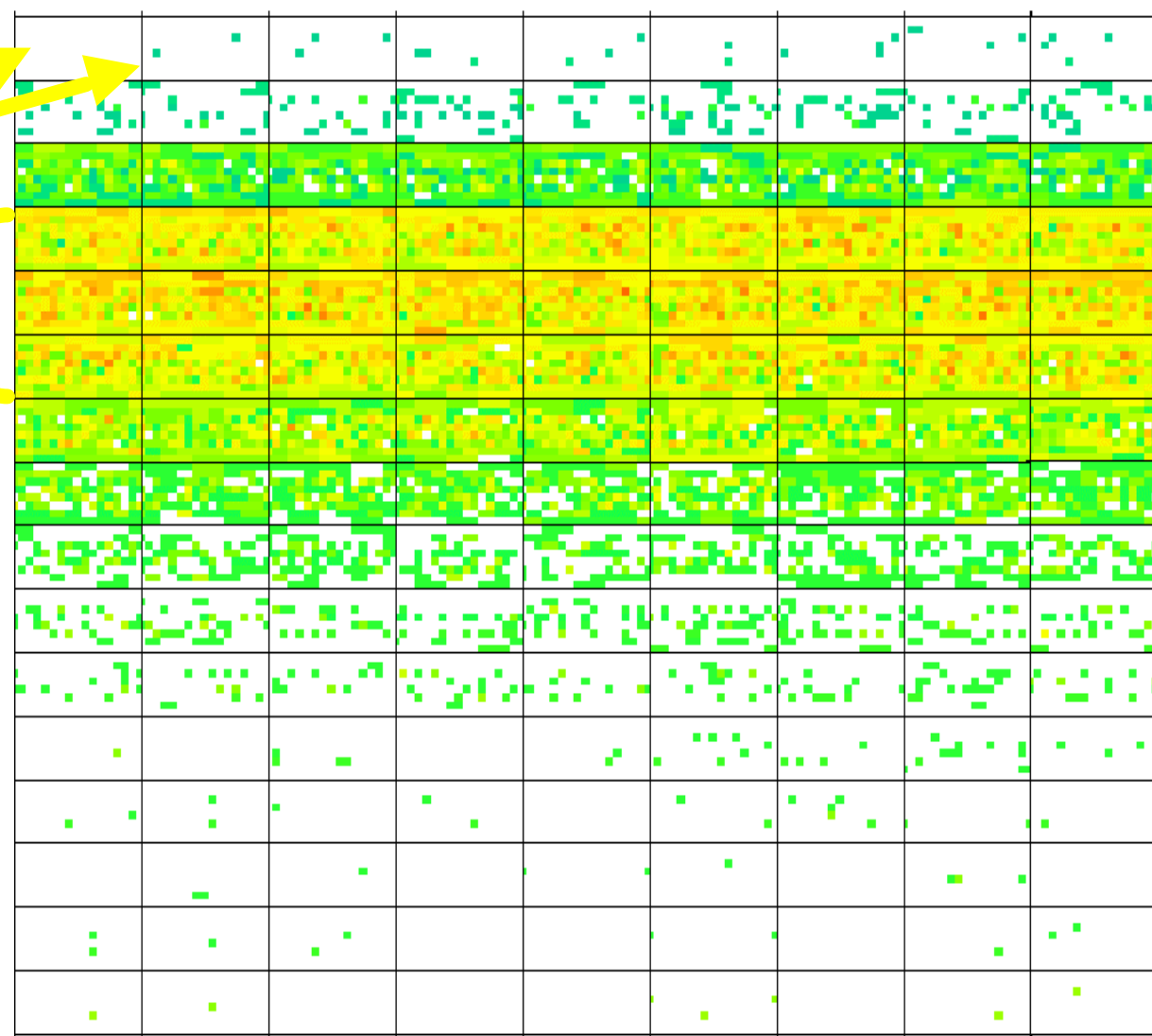
Satellite n°3

**Perfect UV
Rejection**

**CPS:Isotropic
Distributions**

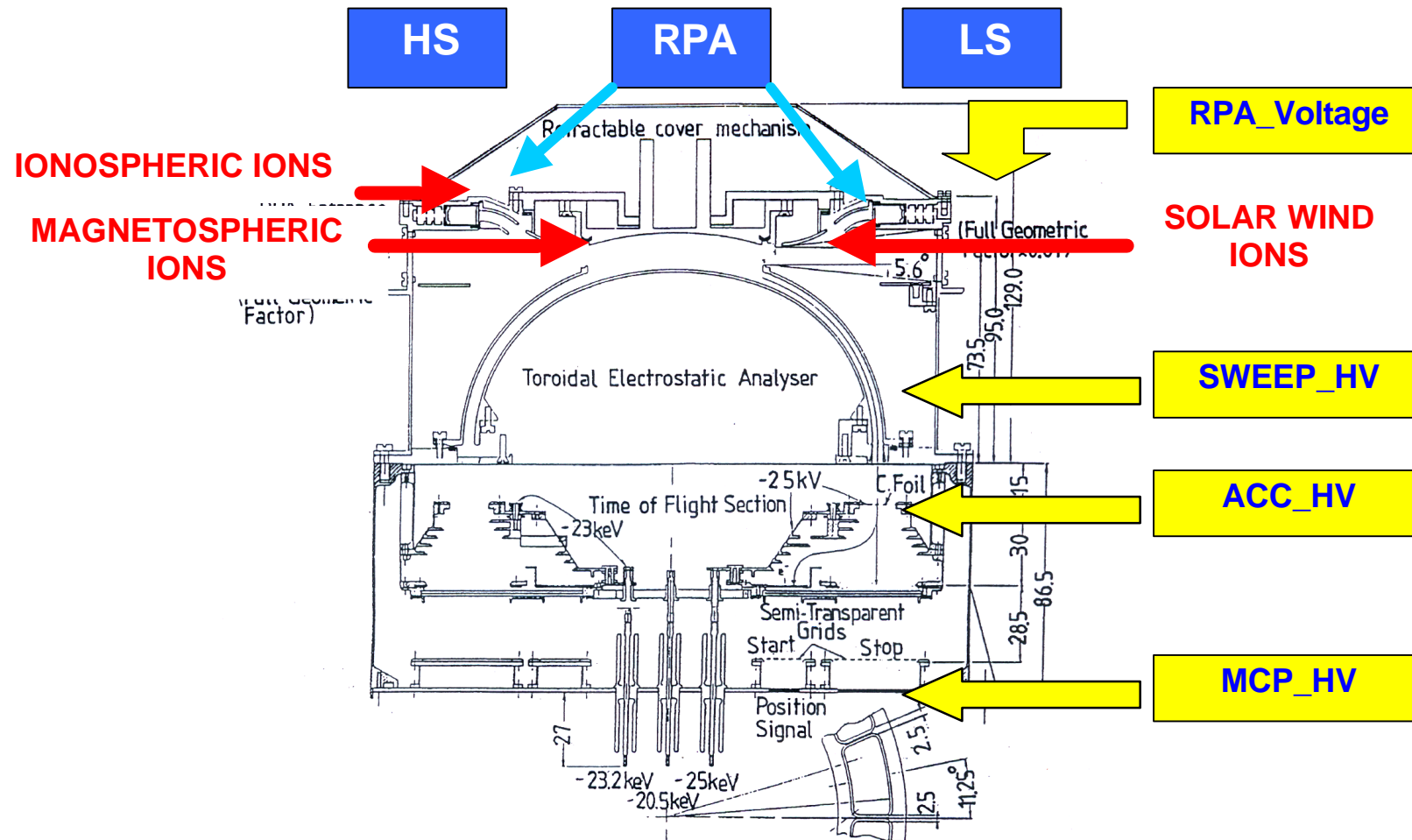
**Low MCP+Amp
Noise**

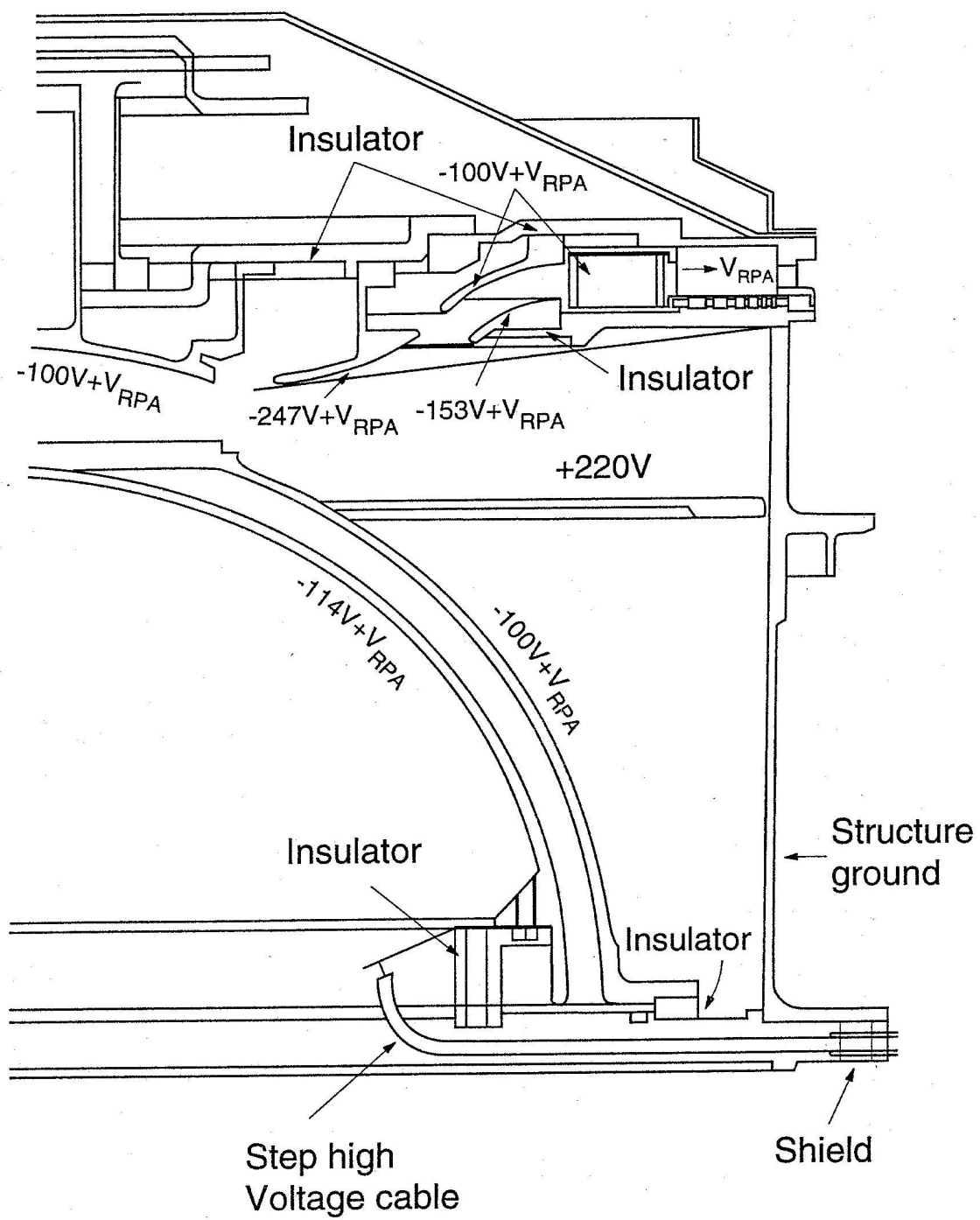
08:51:01 08:51:05 08:51:09 08:51:13 08:51:17 08:51:21 08:51:25 08:51:29 08:51:37

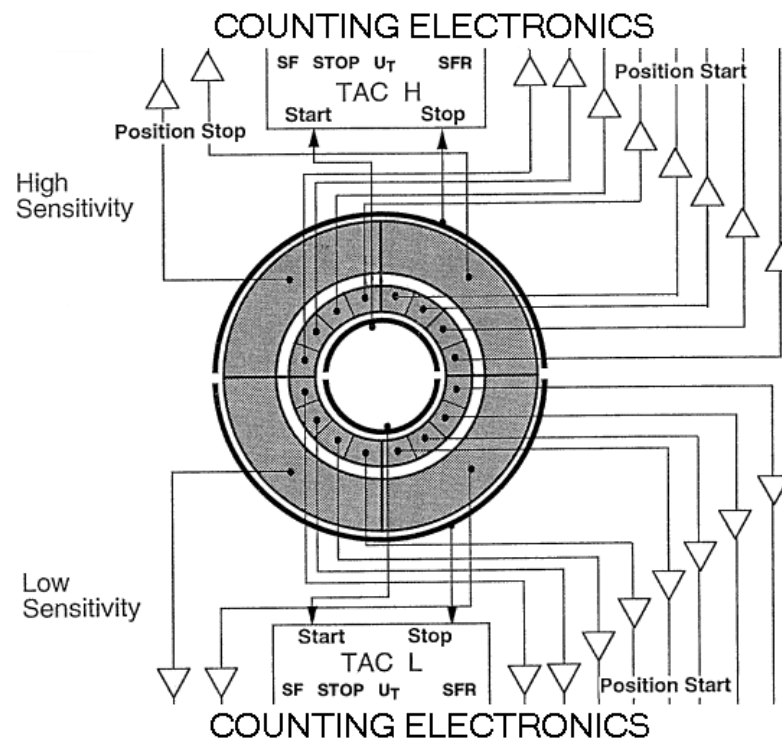
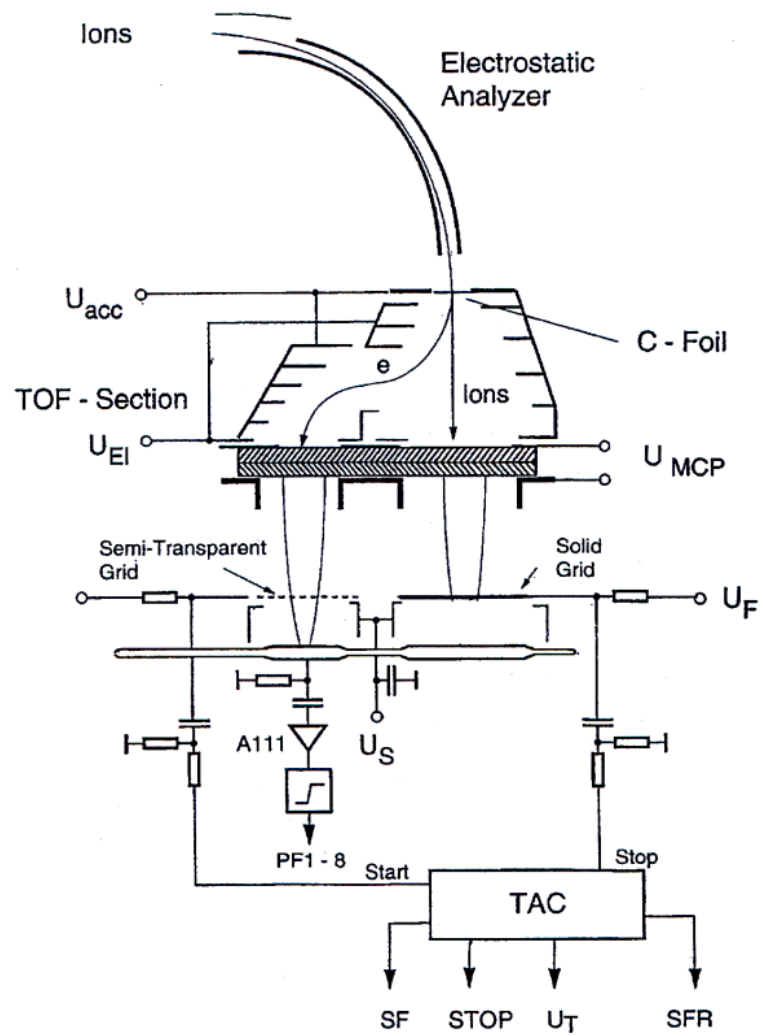


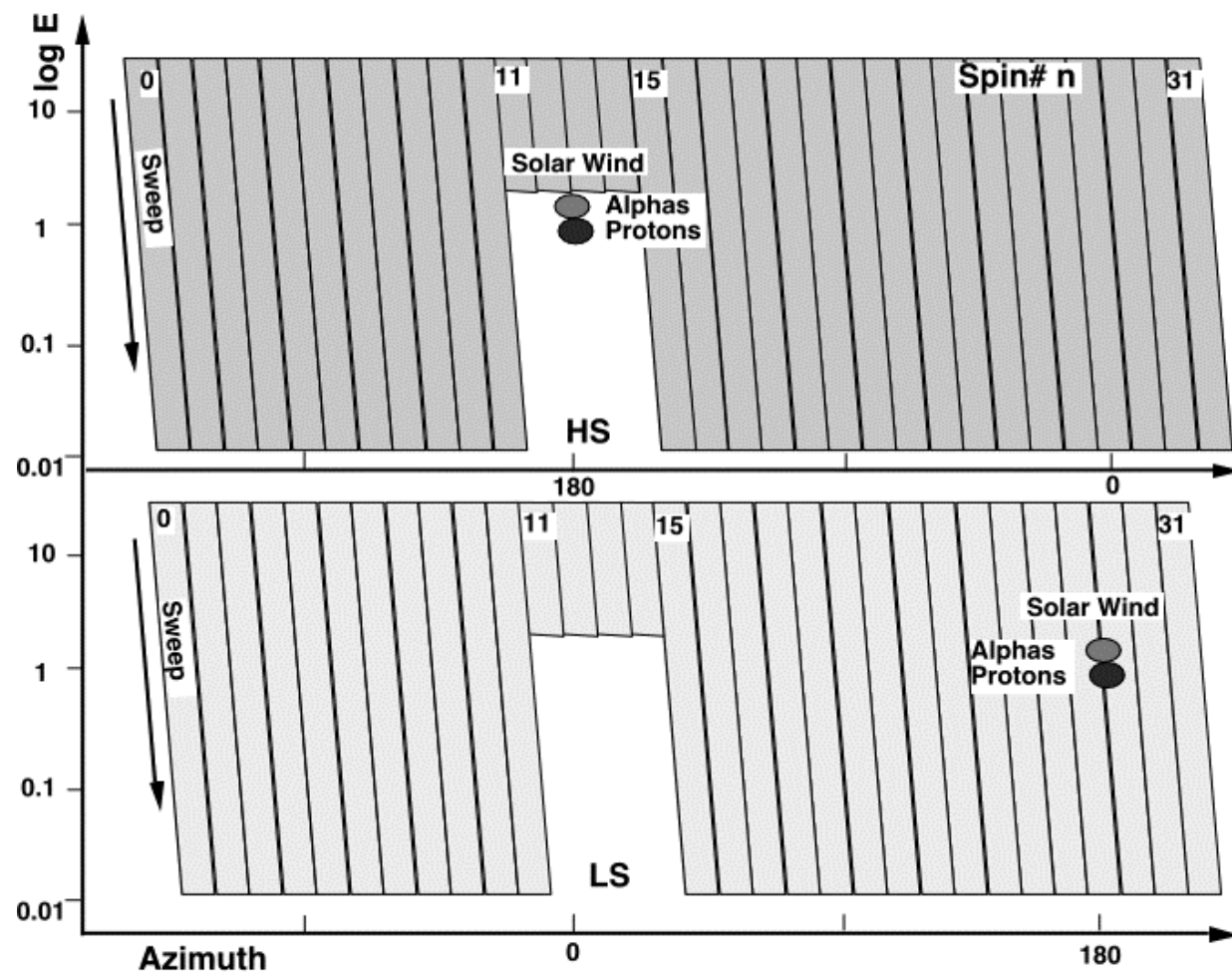
Log c/s
4.0
3.6
3.1
2.7
2.3
1.9
1.4
1.0

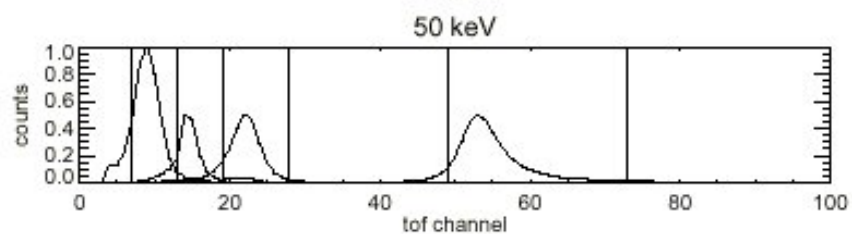
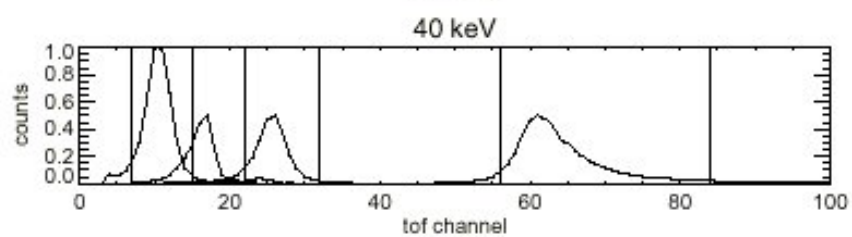
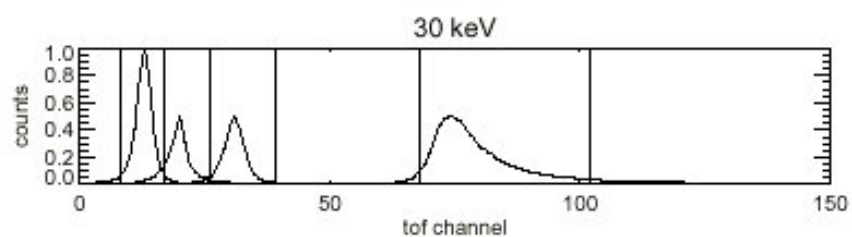
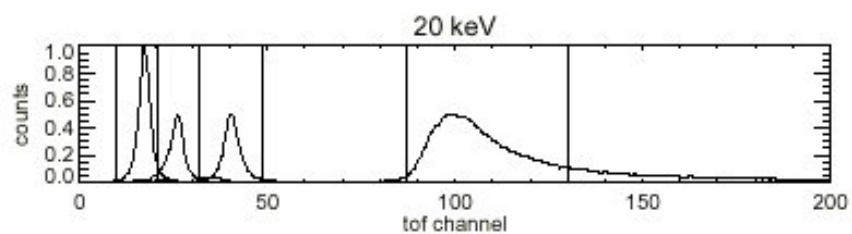
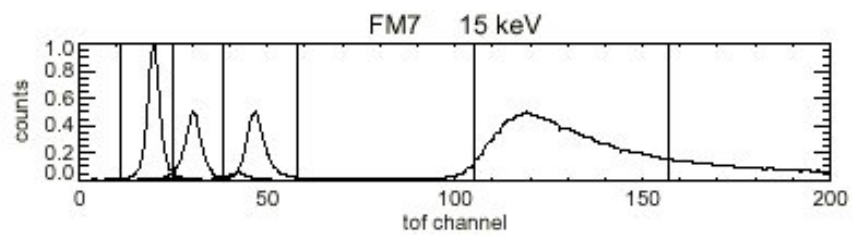
HIA Sensor on s/c 3 : 2000 Sept, 11th



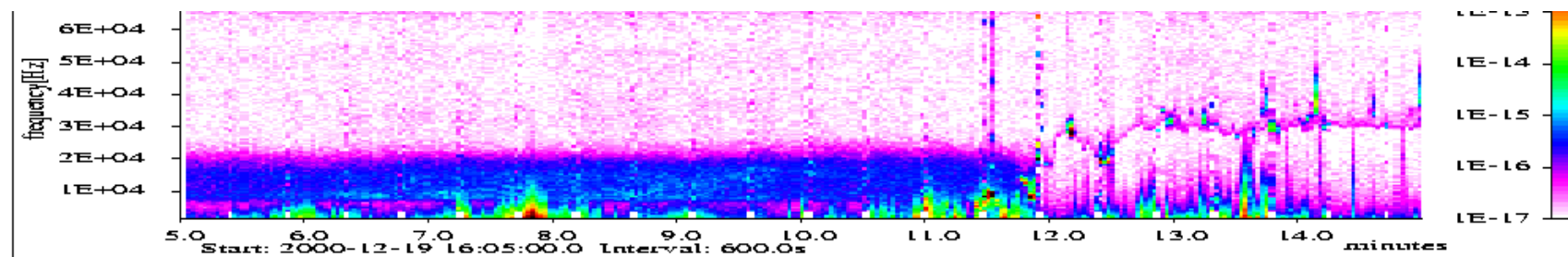
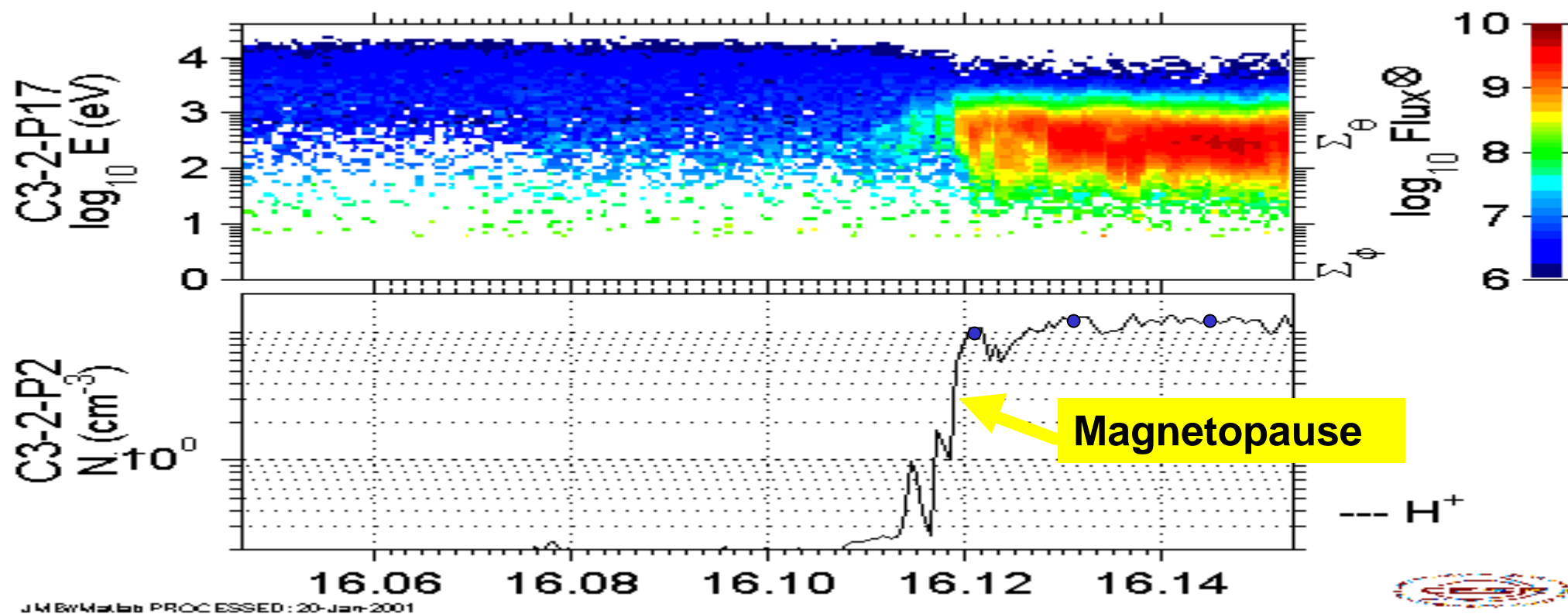








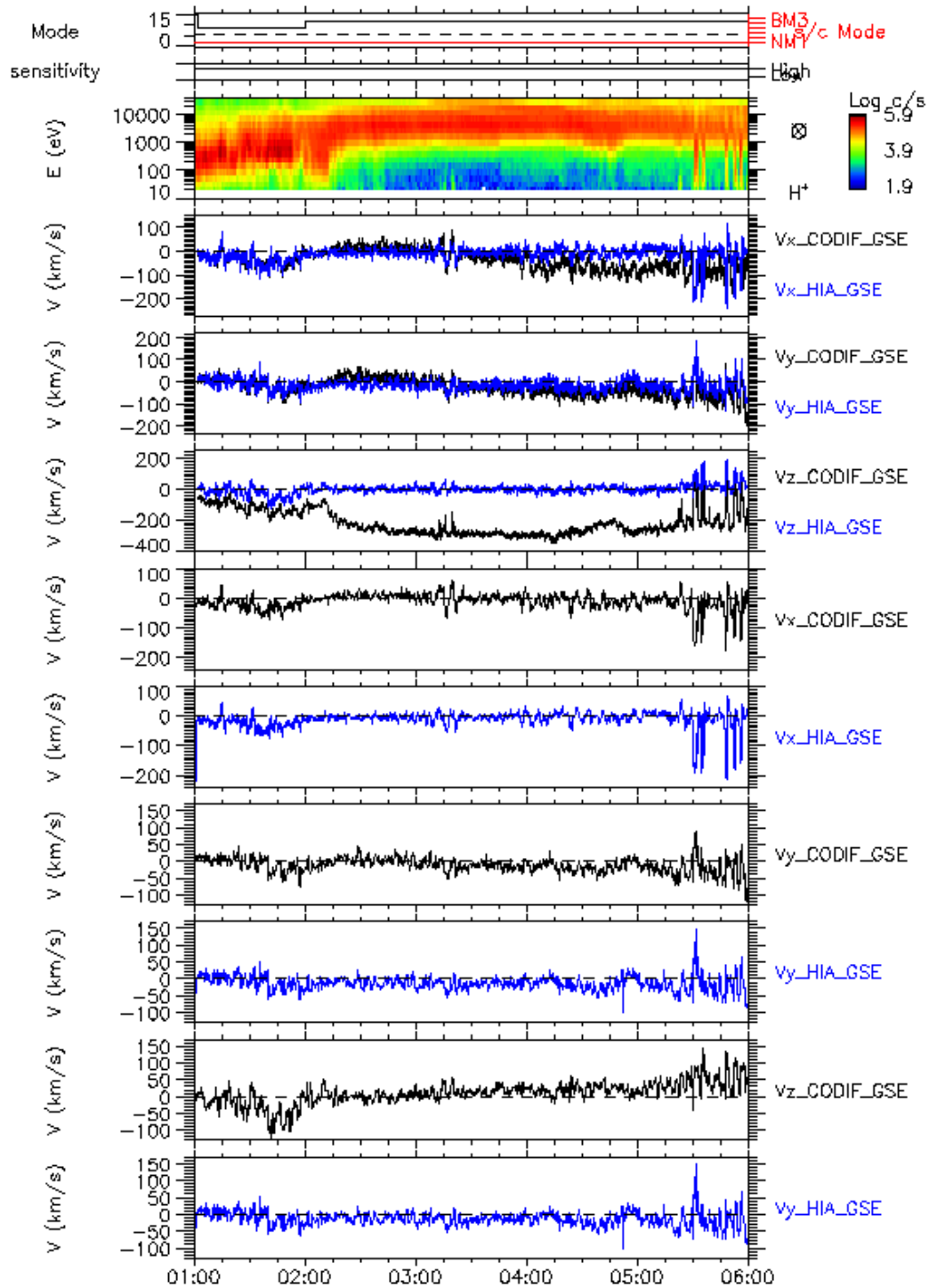
CLUSTER - CIS - DAY=19-12-2000



CIS-CODIF

SAMBA (SC 3)

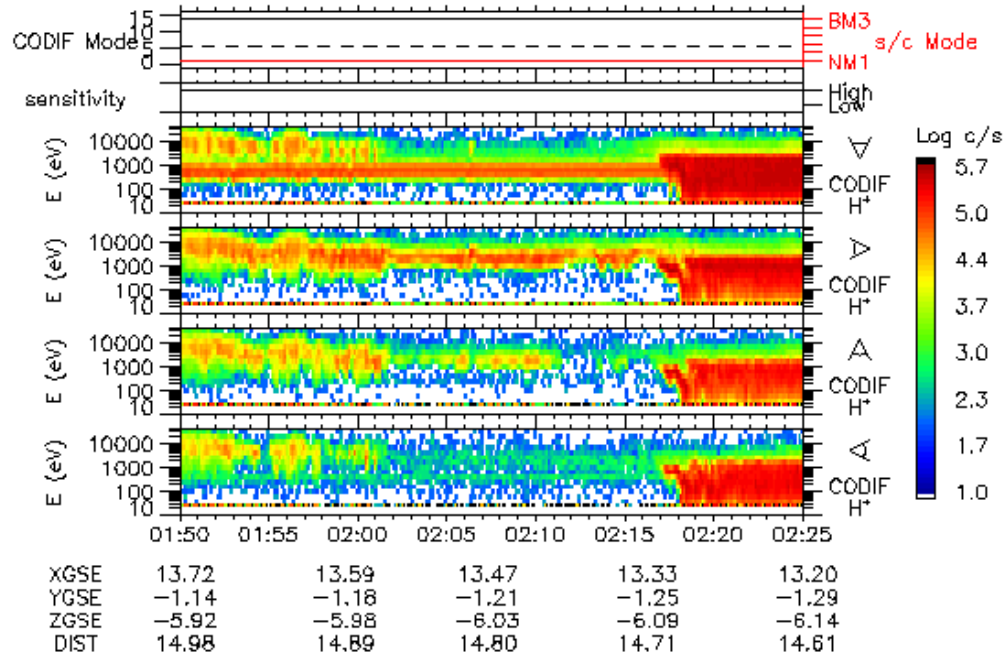
31/Jan/2001



CIS-CODIF

RUMBA (SC 1)

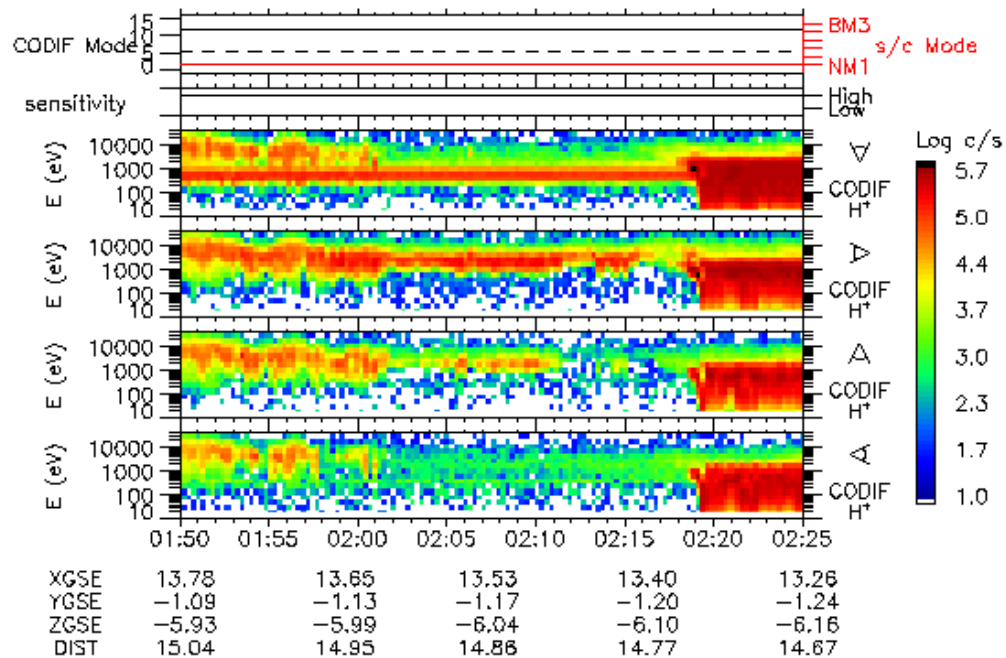
23/Feb/2001



CIS-CODIF

SAMBA (SC 3)

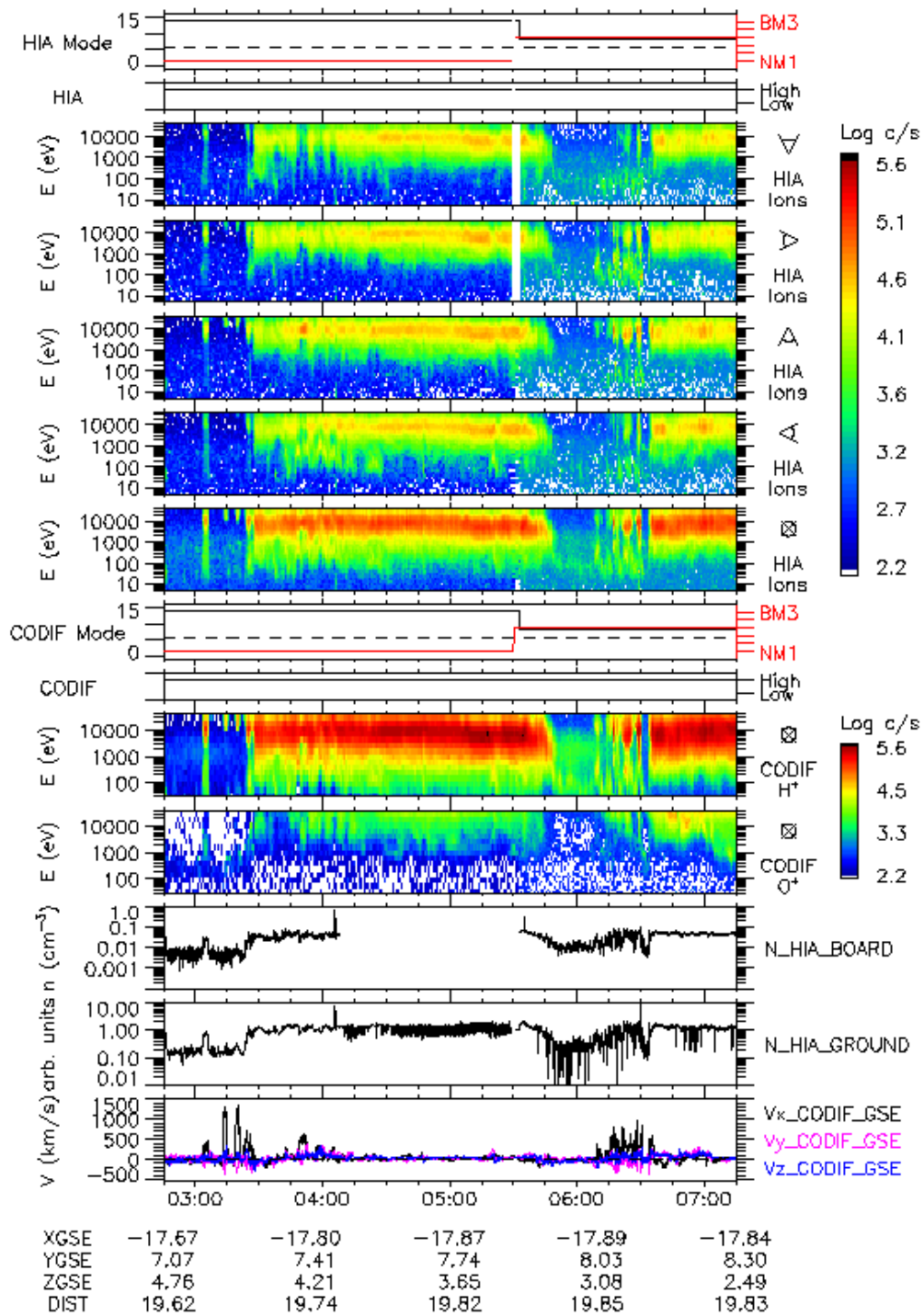
23/Feb/2001

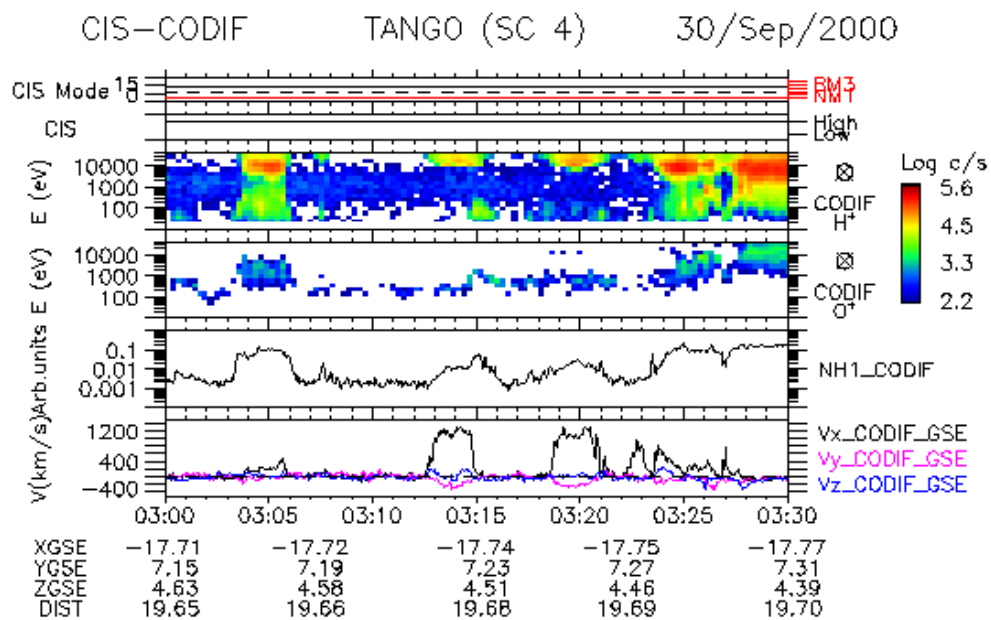
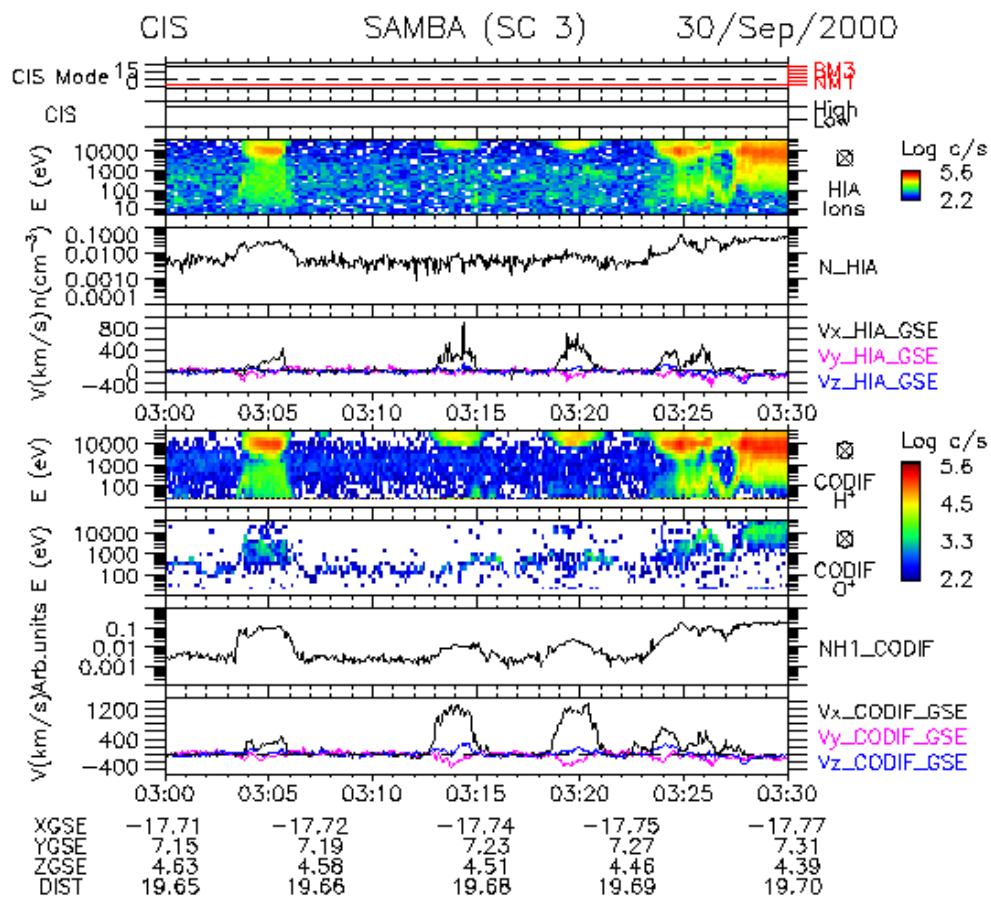


CIS

SAMBA (SC 3)

30/Sep/2000

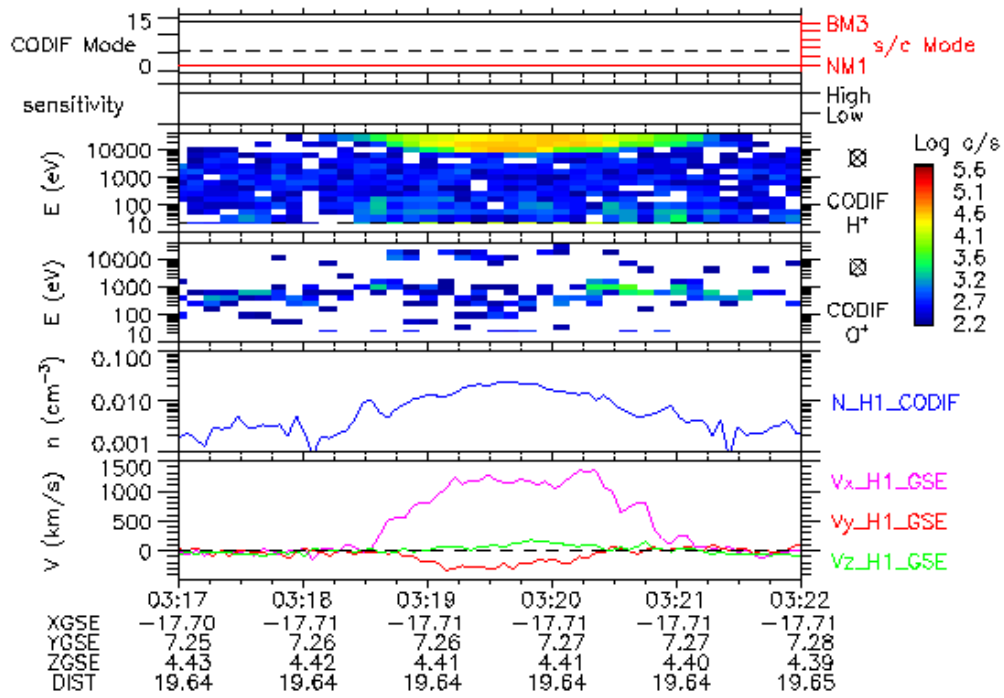




CIS-CODIF

SAMBA (SC 3)

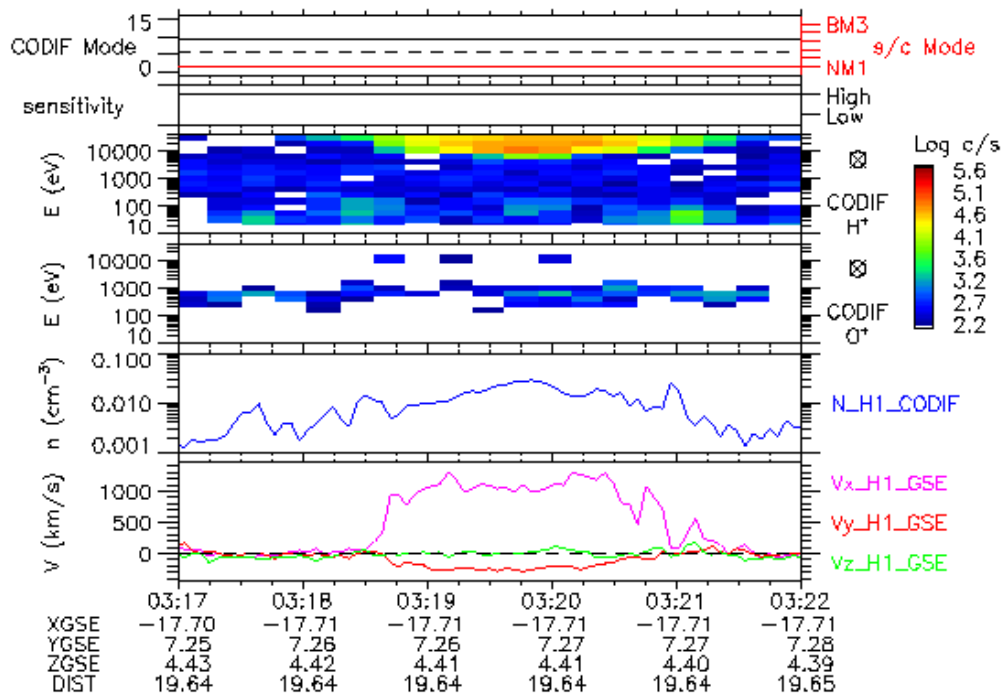
30/Sep/2000

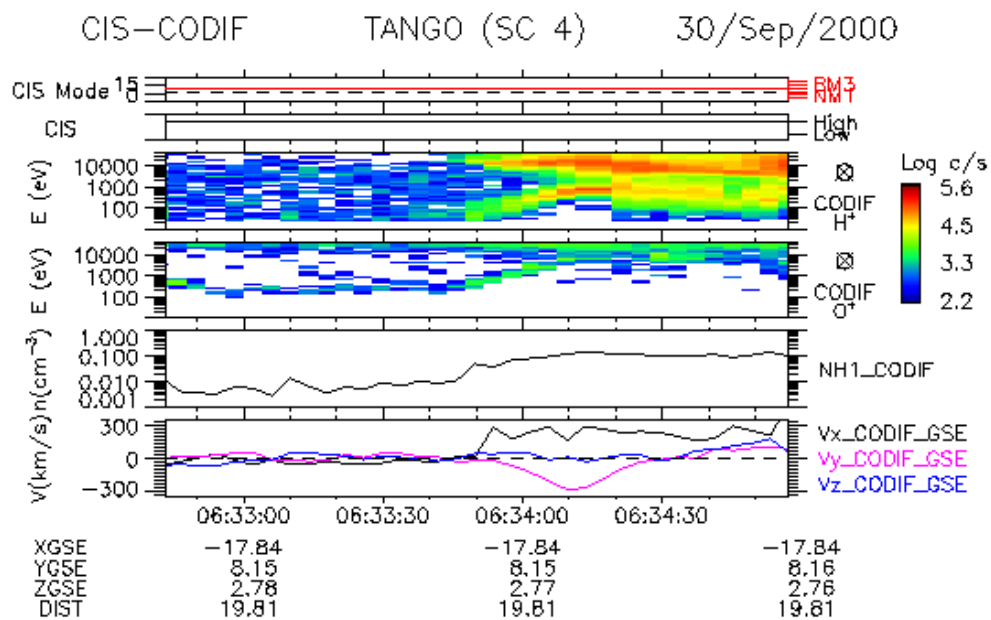
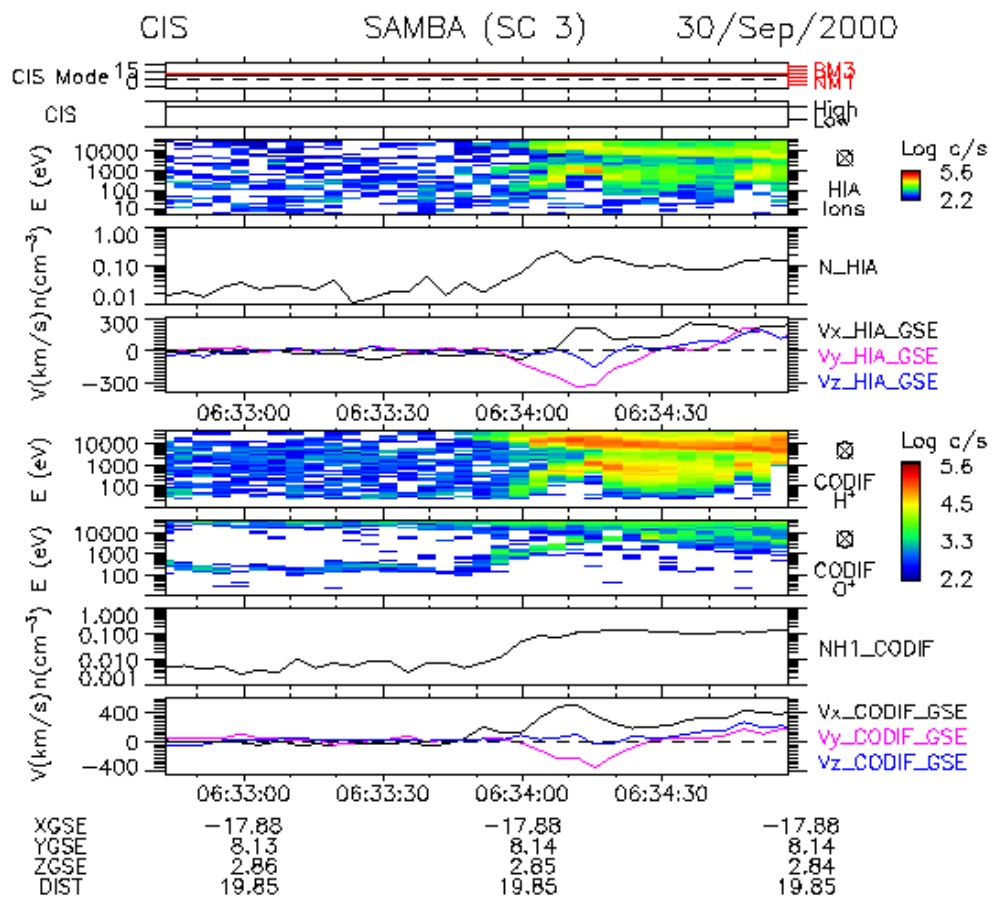


CIS-CODIF

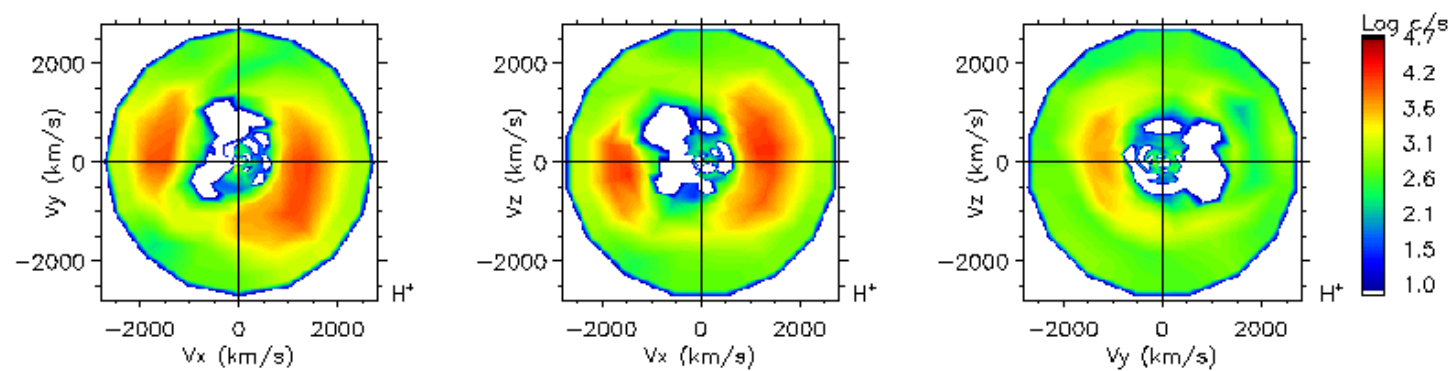
TANGO (SC 4)

30/Sep/2000



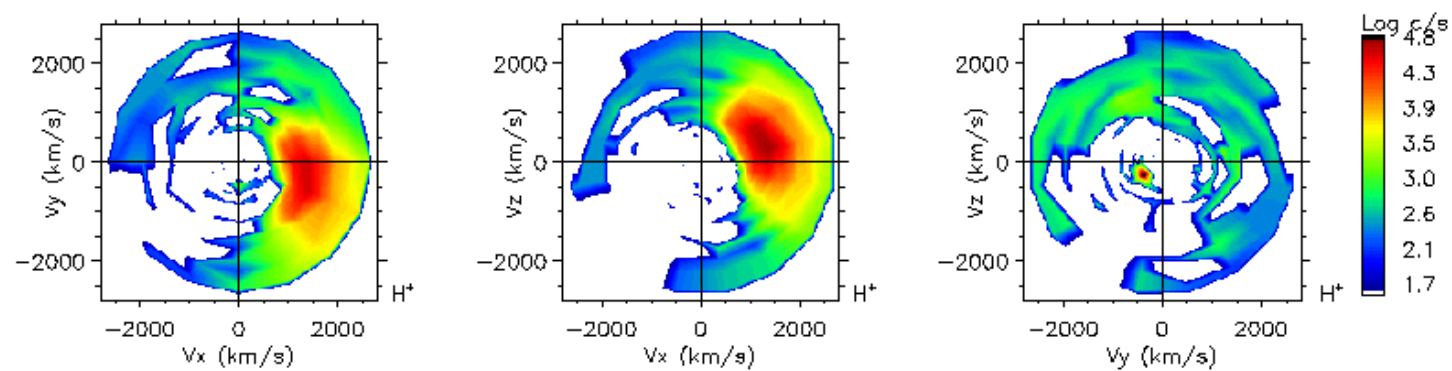


CIS-CODIF SAMBA (SC 3) 30/Sep/2000 03:04:31.044



3 spin accumulation

CIS-CODIF SAMBA (SC 3) 30/Sep/2000 06:17:23.074

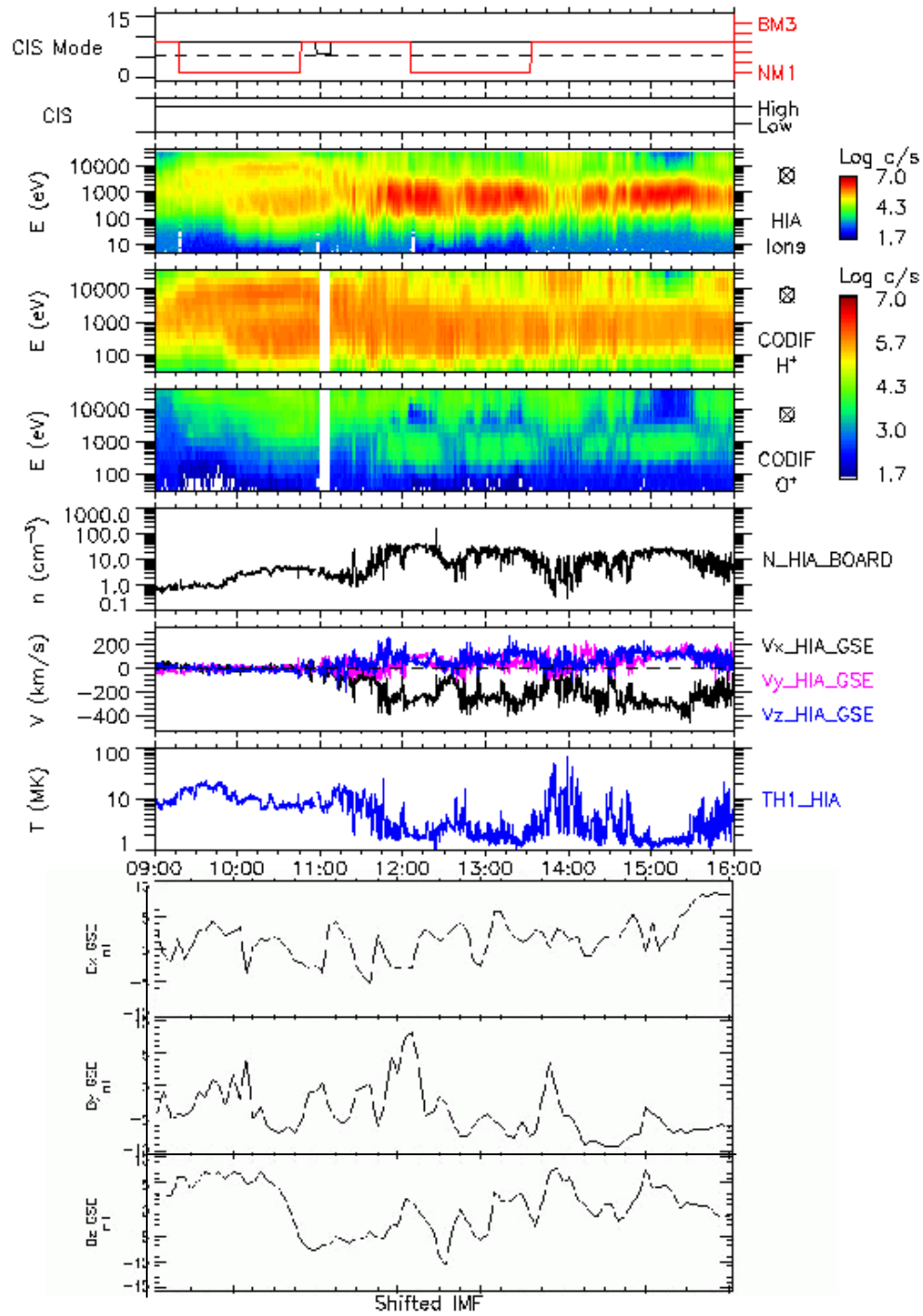


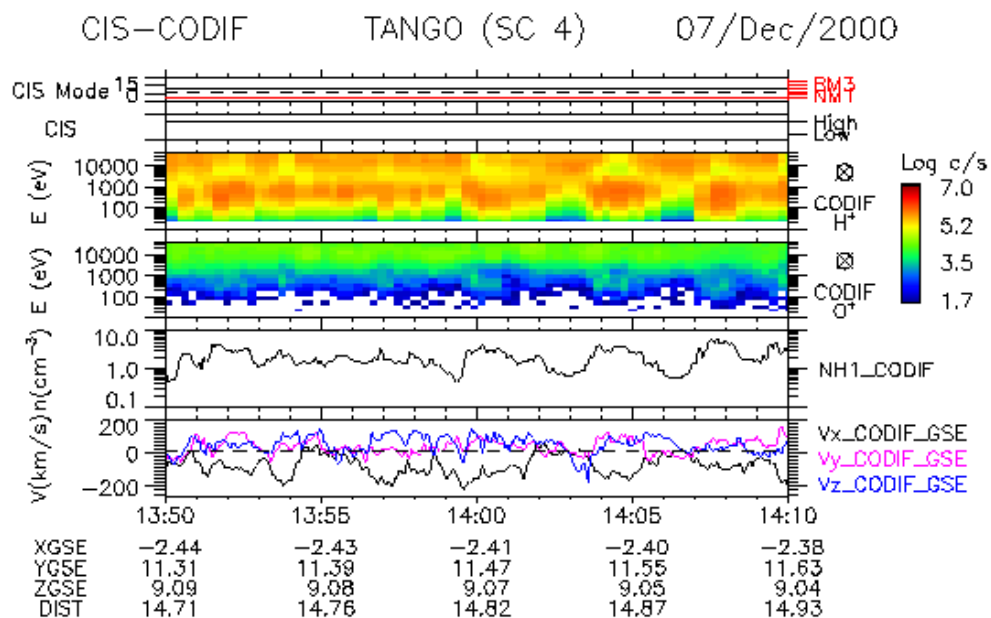
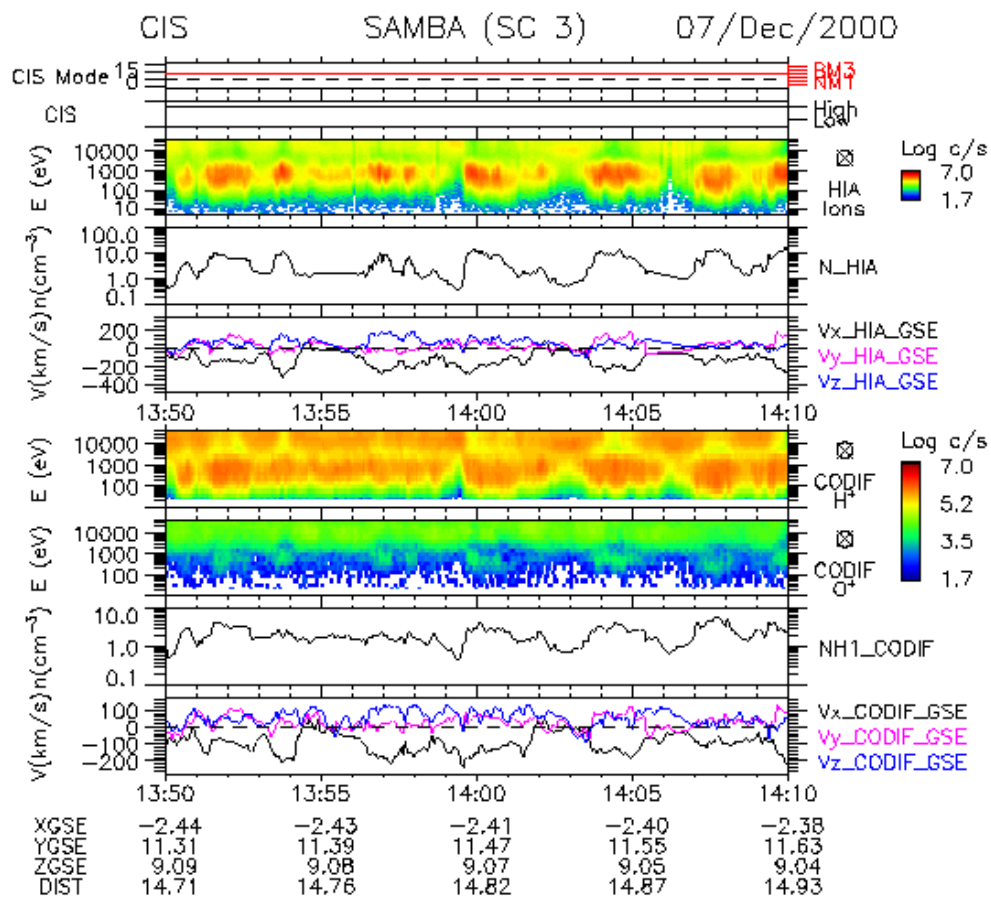
3 spin accumulation

CIS

SAMBA (SC 3)

07/Dec/2000

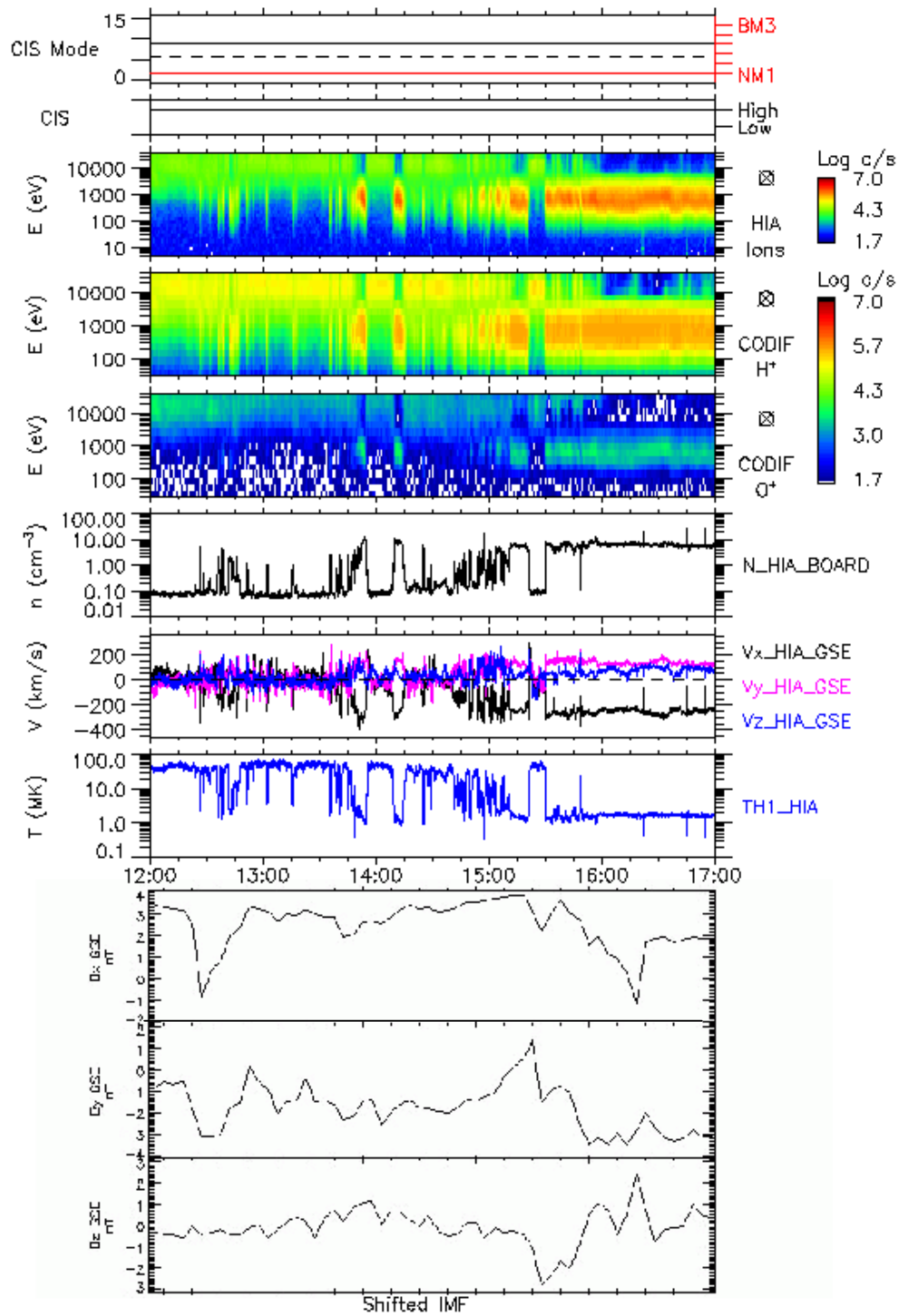




CIS

SAMBA (SC 3)

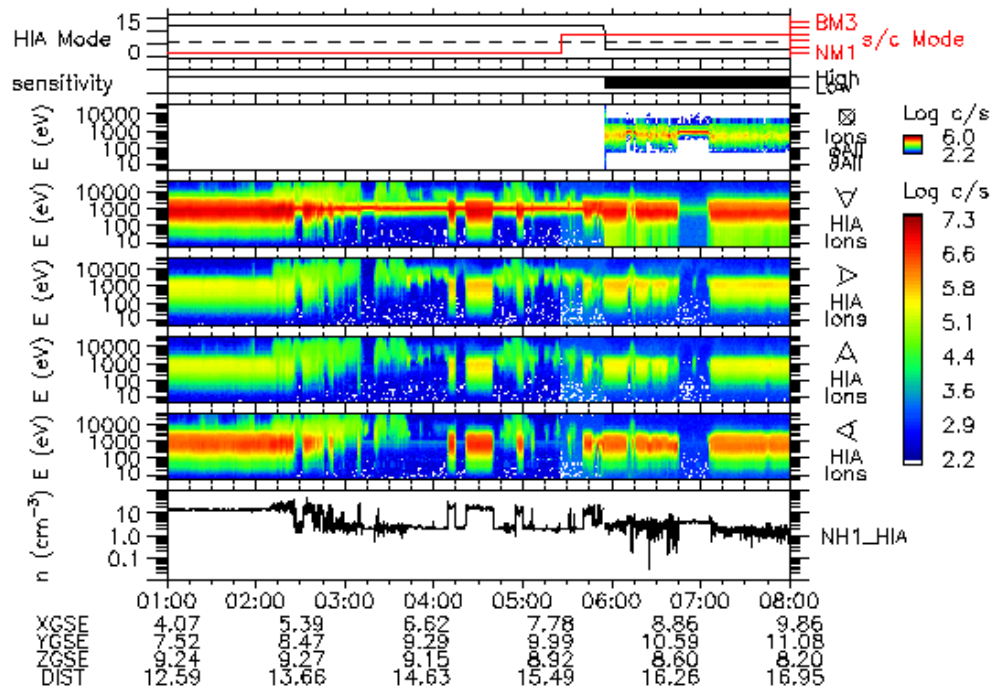
12/Dec/2000



CIS-HIA

RUMBA (SC 1)

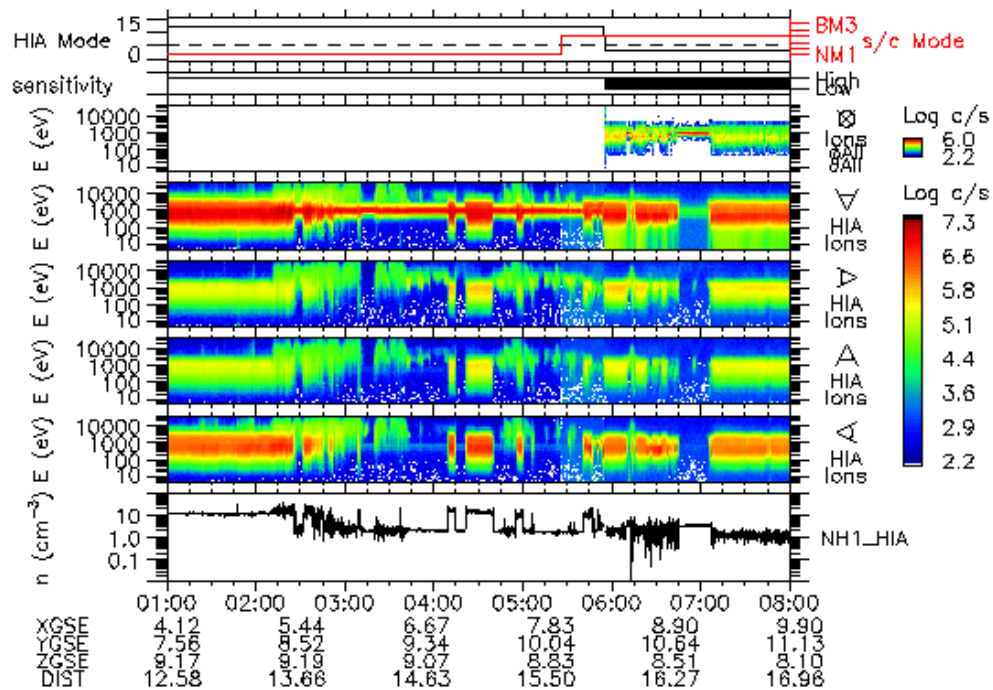
24/Jan/2001



CIS-HIA

SAMBA (SC 3)

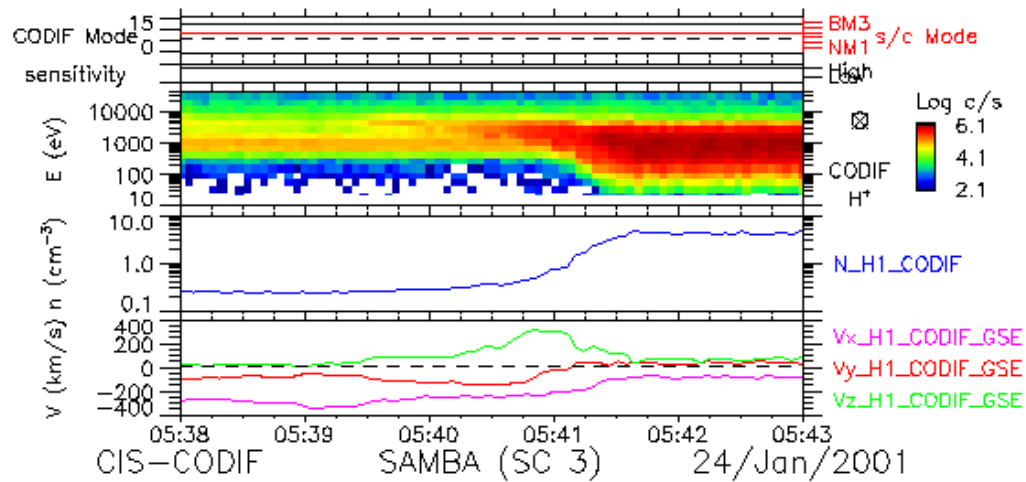
24/Jan/2001



CIS-CODIF

RUMBA (SC 1)

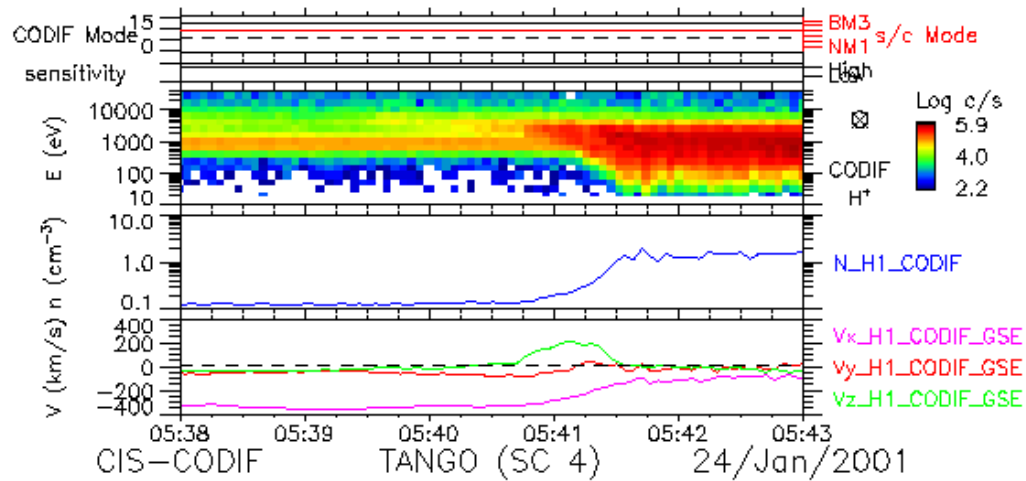
24/Jan/2001



CIS-CODIF

SAMBA (SC 3)

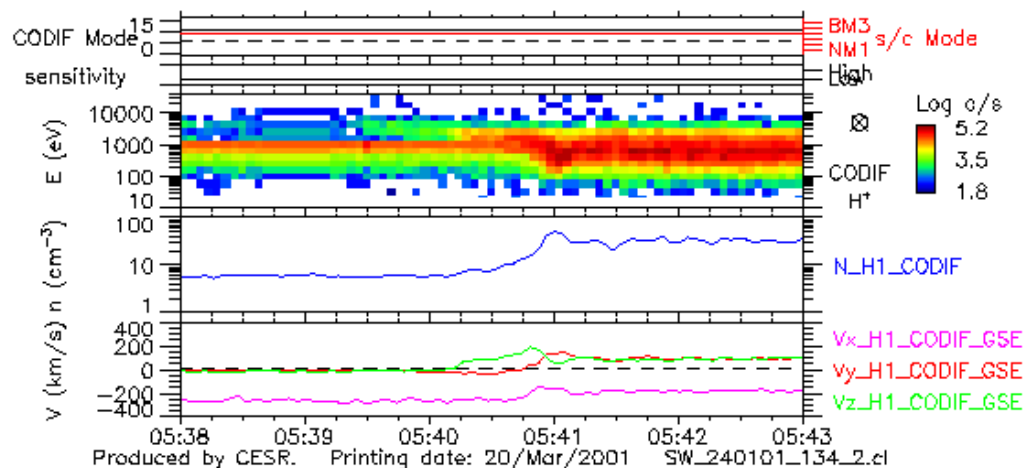
24/Jan/2001



CIS-CODIF

TANGO (SC 4)

24/Jan/2001

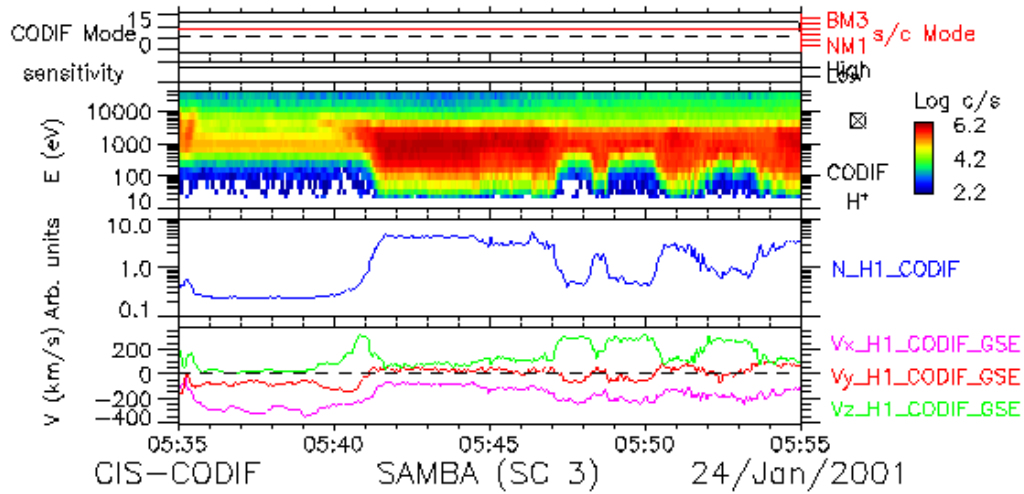


Produced by CESR. Printing date: 20/Mar/2001 SW_240101_134_2.cl

CIS-CODIF

RUMBA (SC 1)

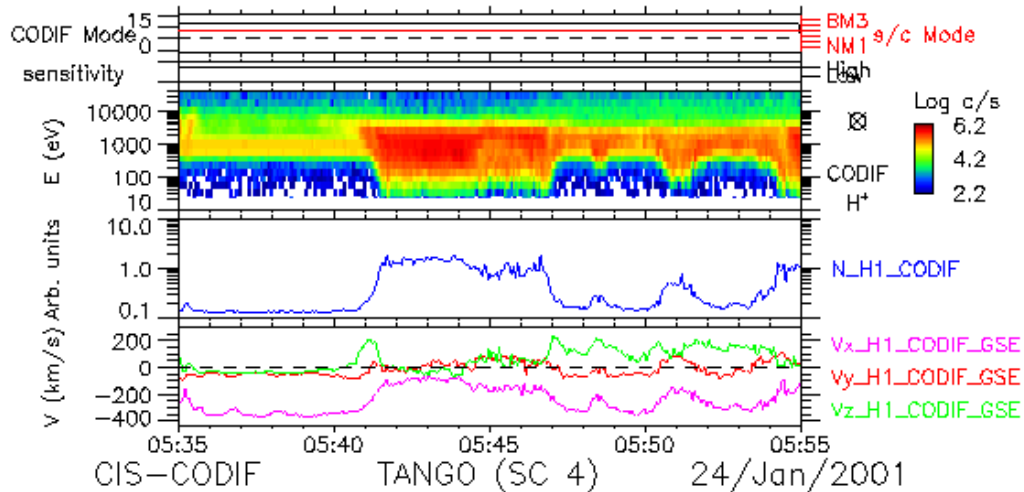
24/Jan/2001



CIS-CODIF

SAMBA (SC 3)

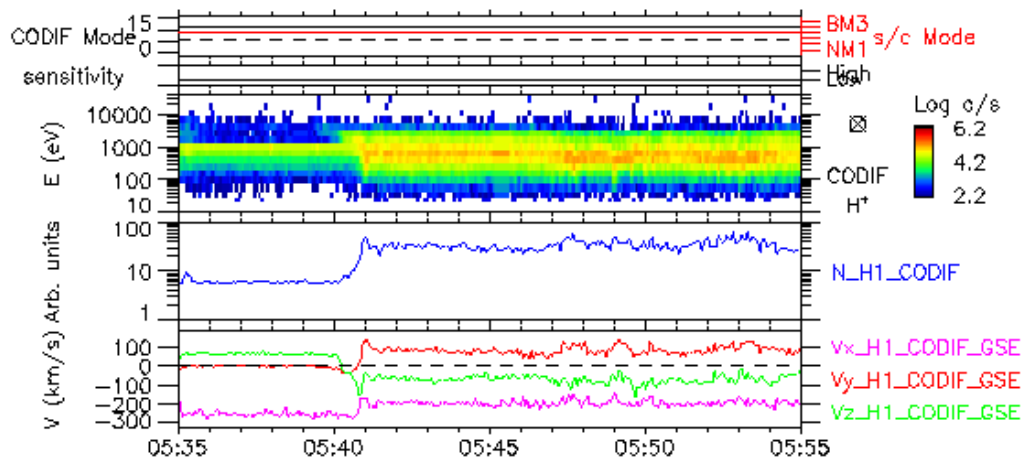
24/Jan/2001



CIS-CODIF

TANGO (SC 4)

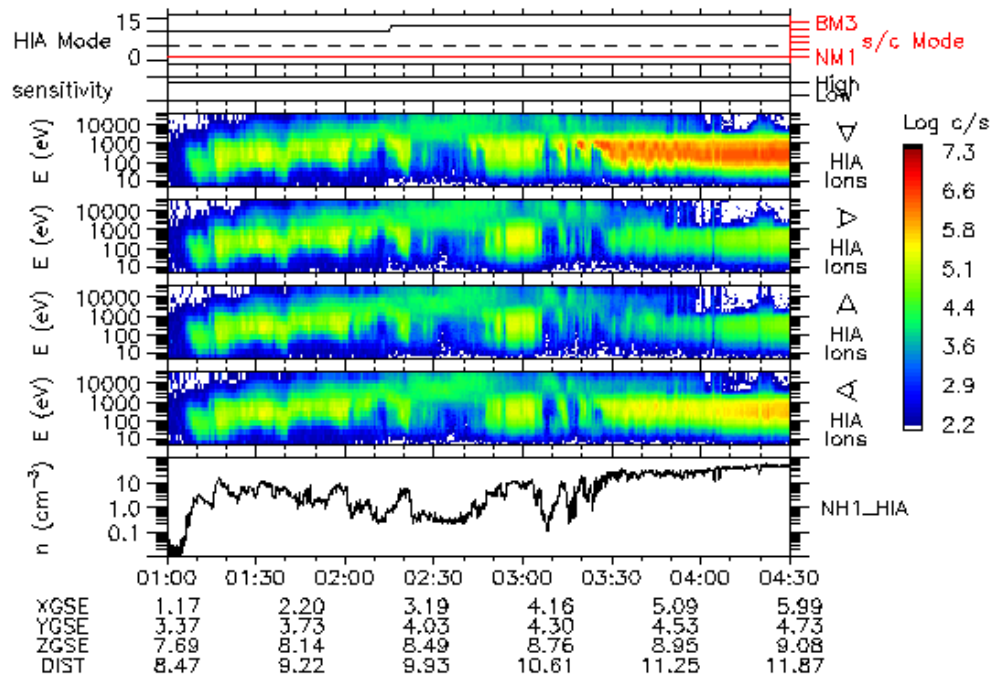
24/Jan/2001



CIS-HIA

RUMBA (SC 1)

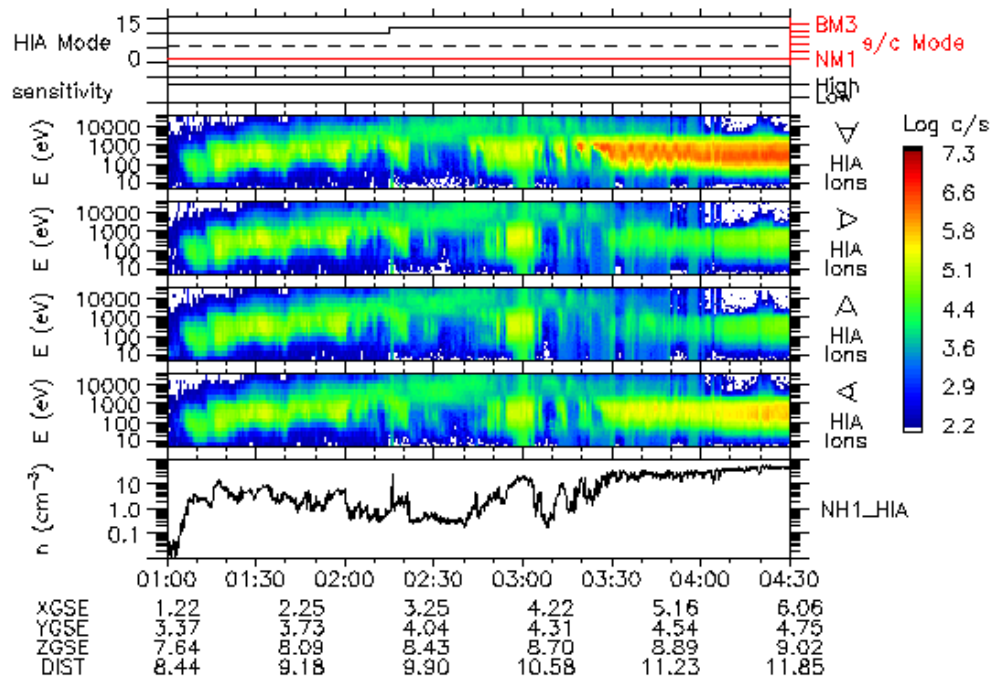
19/Feb/2001



CIS-HIA

SAMBA (SC 3)

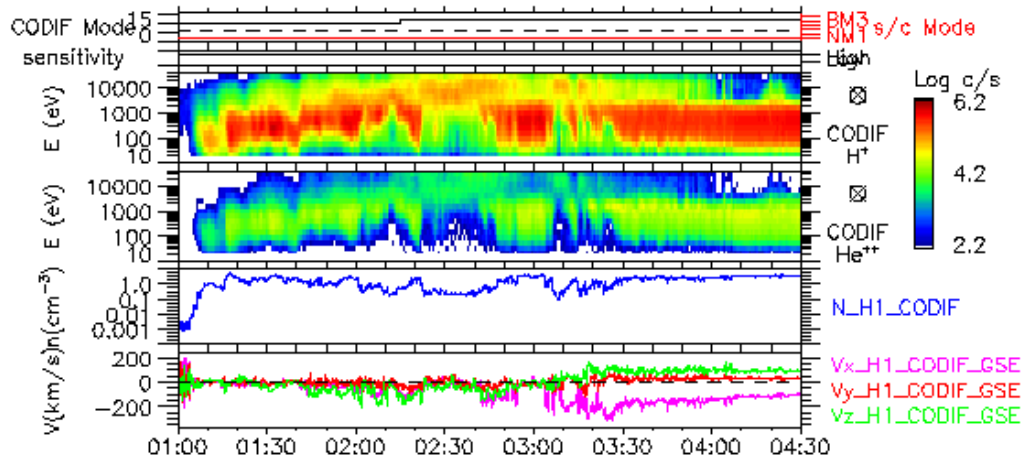
19/Feb/2001



CIS-CODIF

RUMBA (SC 1)

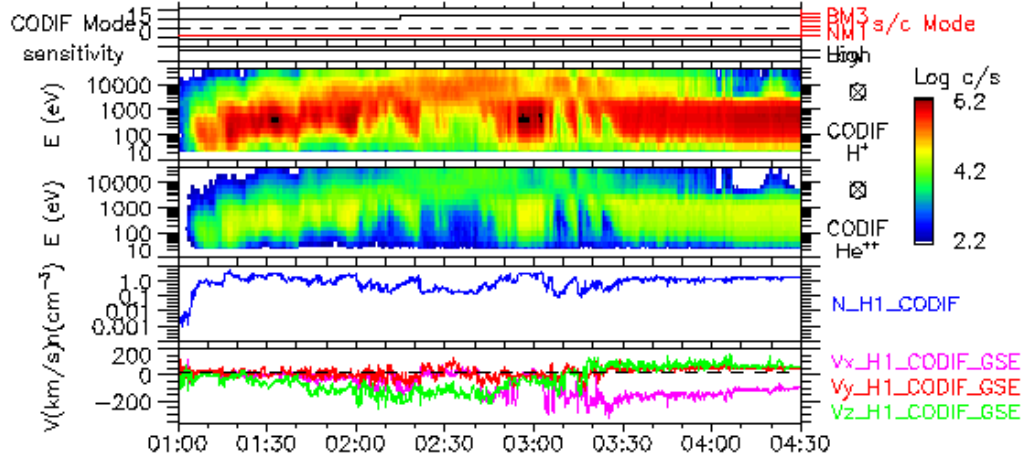
19/Feb/2001



CIS-CODIF

SAMBA (SC 3)

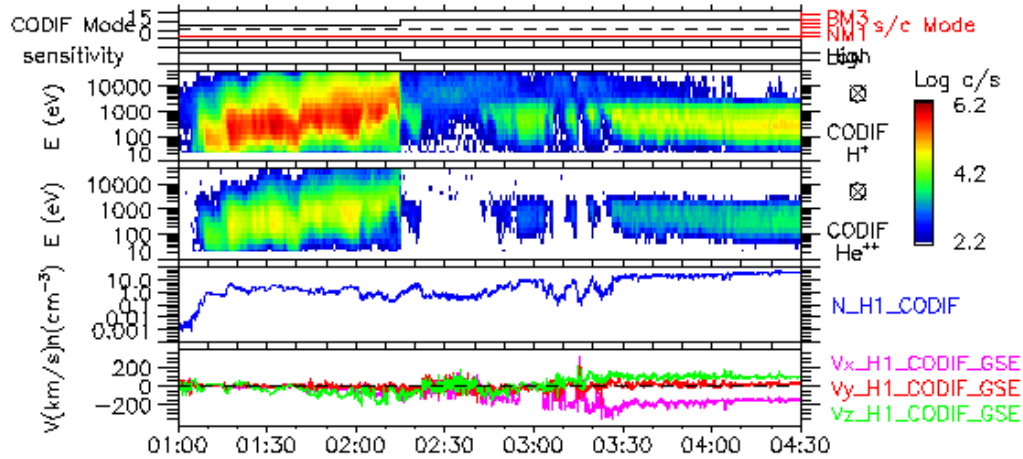
19/Feb/2001



CIS-CODIF

TANGO (SC 4)

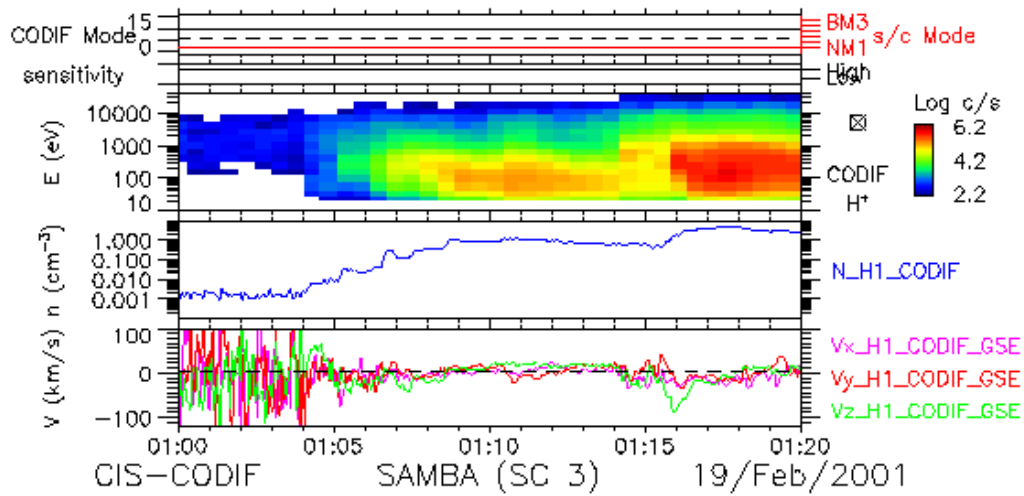
19/Feb/2001



CIS-CODIF

RUMBA (SC 1)

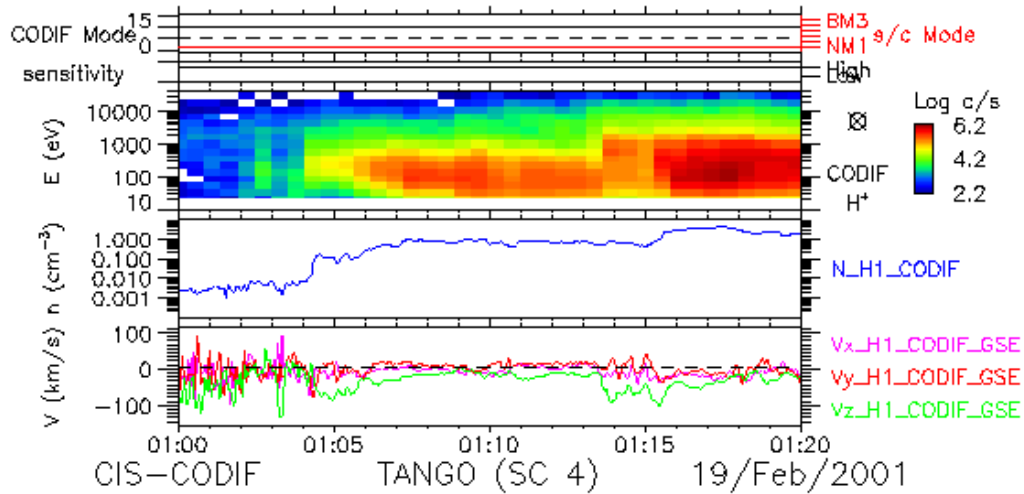
19/Feb/2001



CIS-CODIF

SAMBA (SC 3)

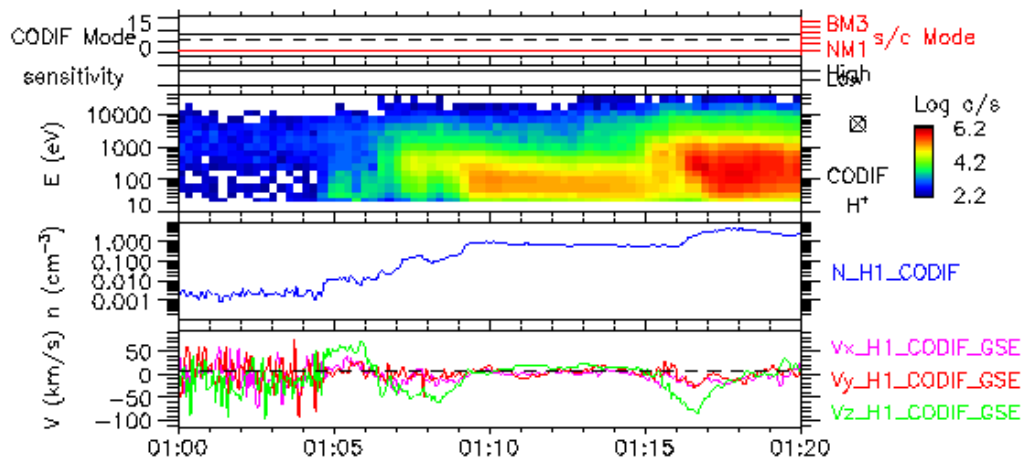
19/Feb/2001



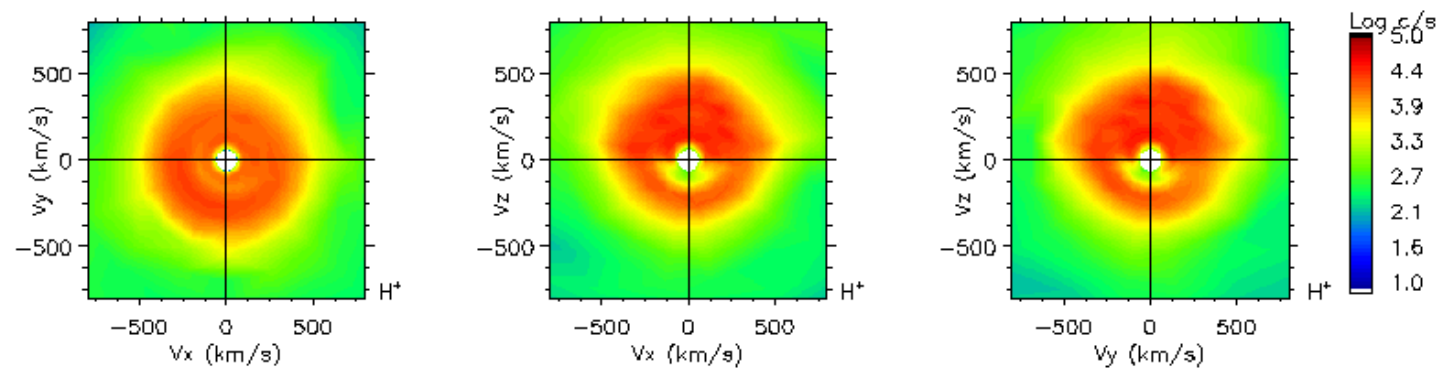
CIS-CODIF

TANGO (SC 4)

19/Feb/2001



CIS-CODIF SAMBA (SC 3) 19/Feb/2001 01:18:30.752

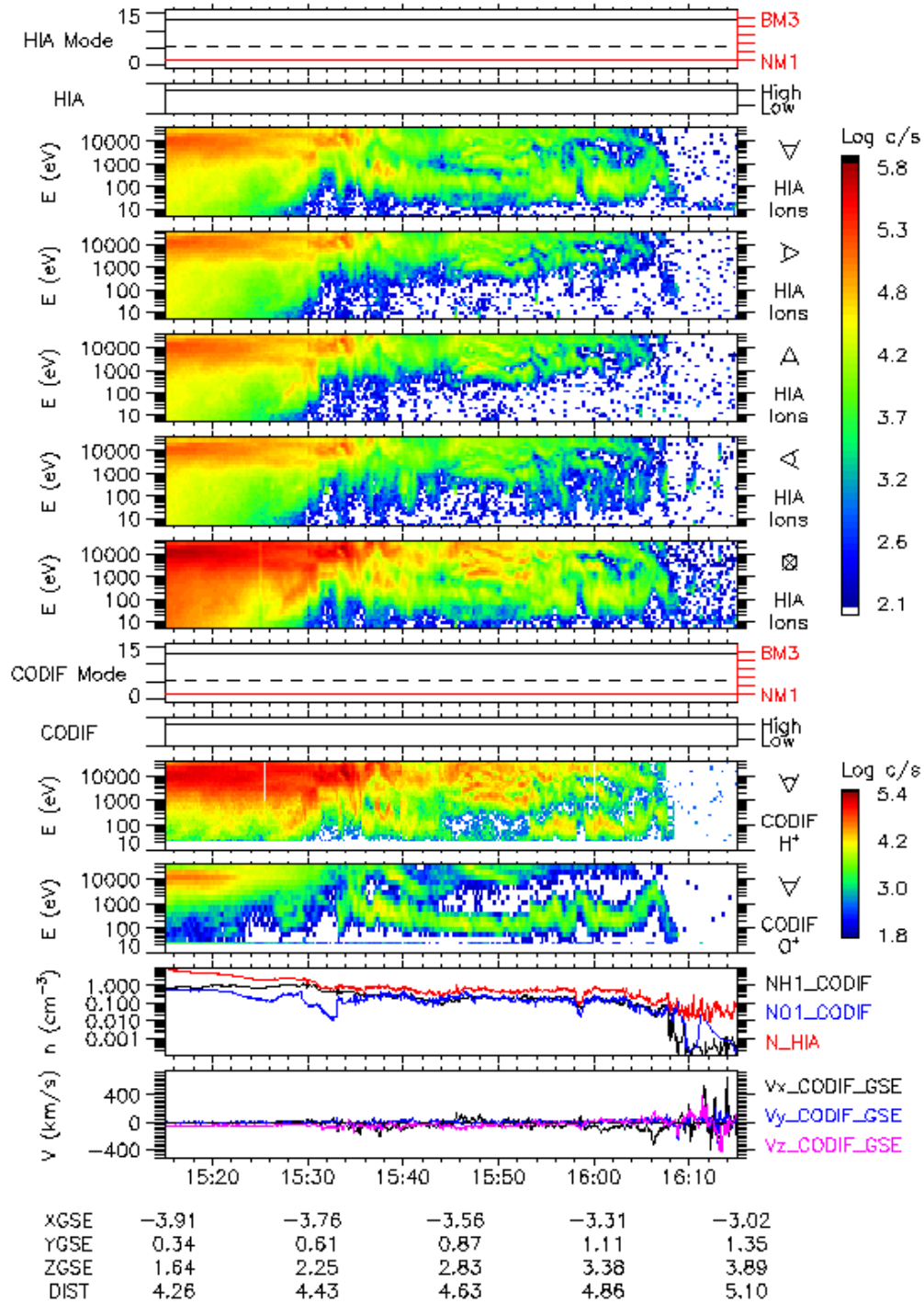


3 spin accumulation

CIS

RUMBA (SC 1)

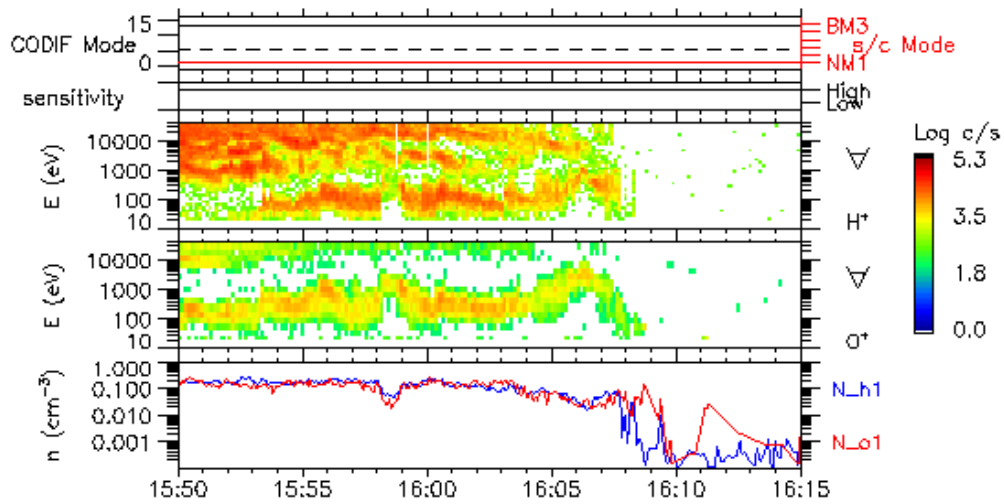
23/Feb/2001



CIS-CODIF

RUMBA (SC 1)

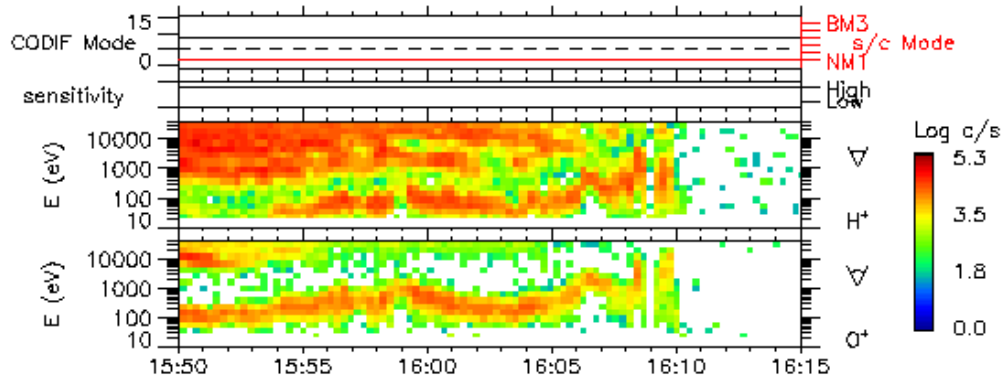
23/Feb/2001



CIS-CODIF

SAMBA (SC 3)

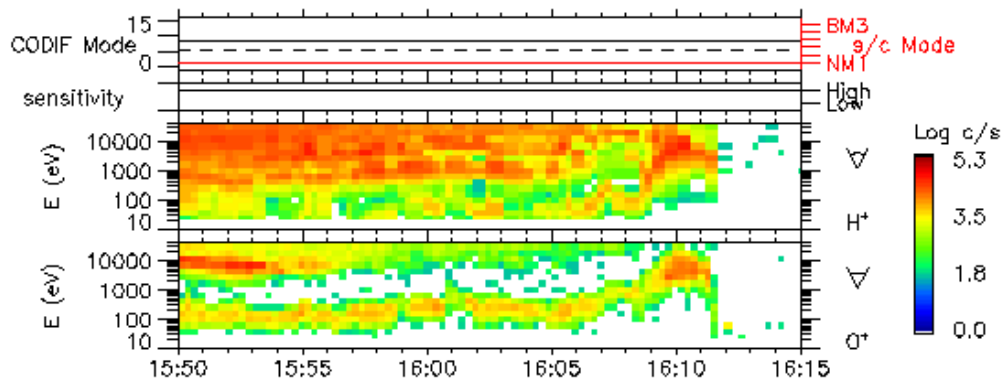
23/Feb/2001



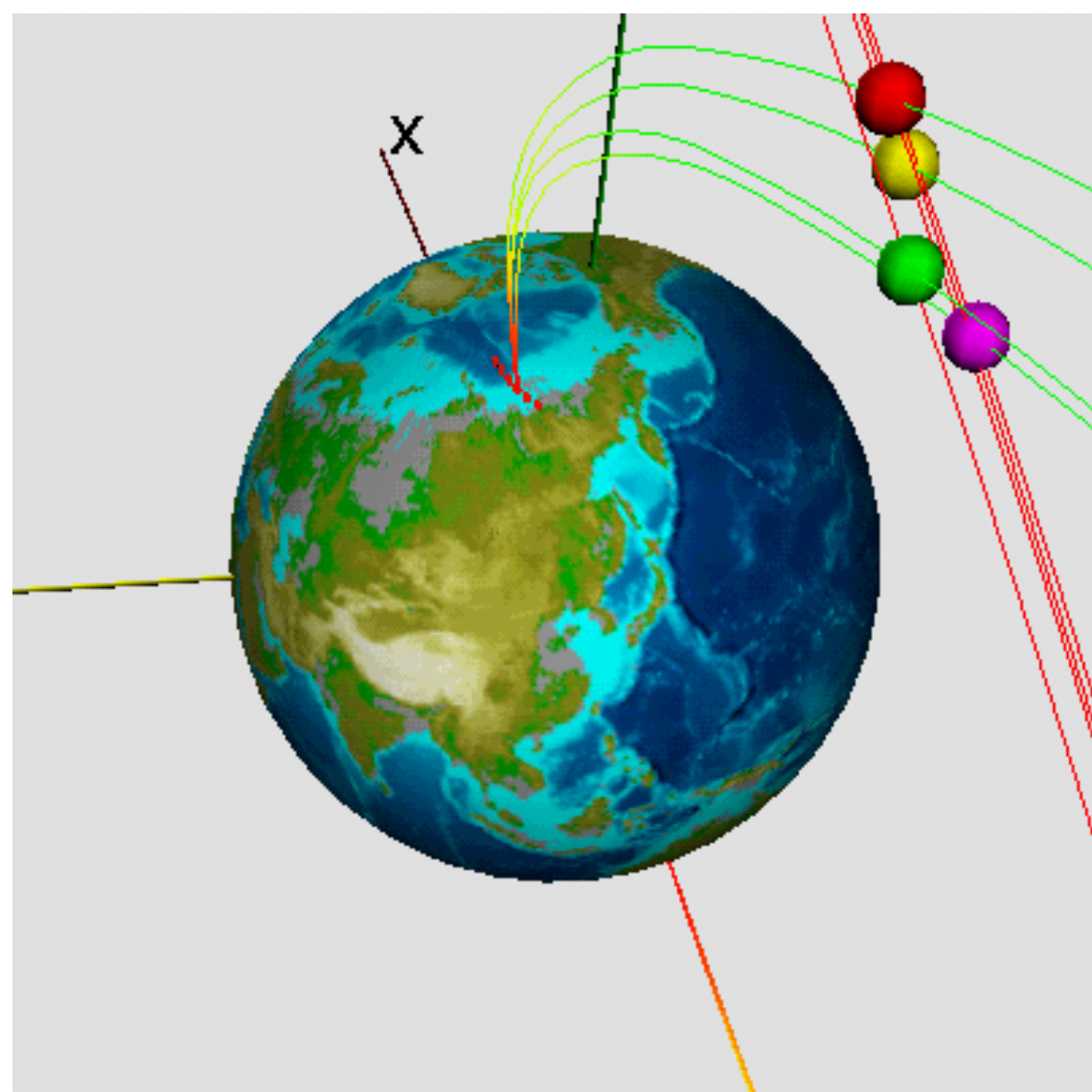
CIS-CODIF

TANGO (SC 4)

23/Feb/2001



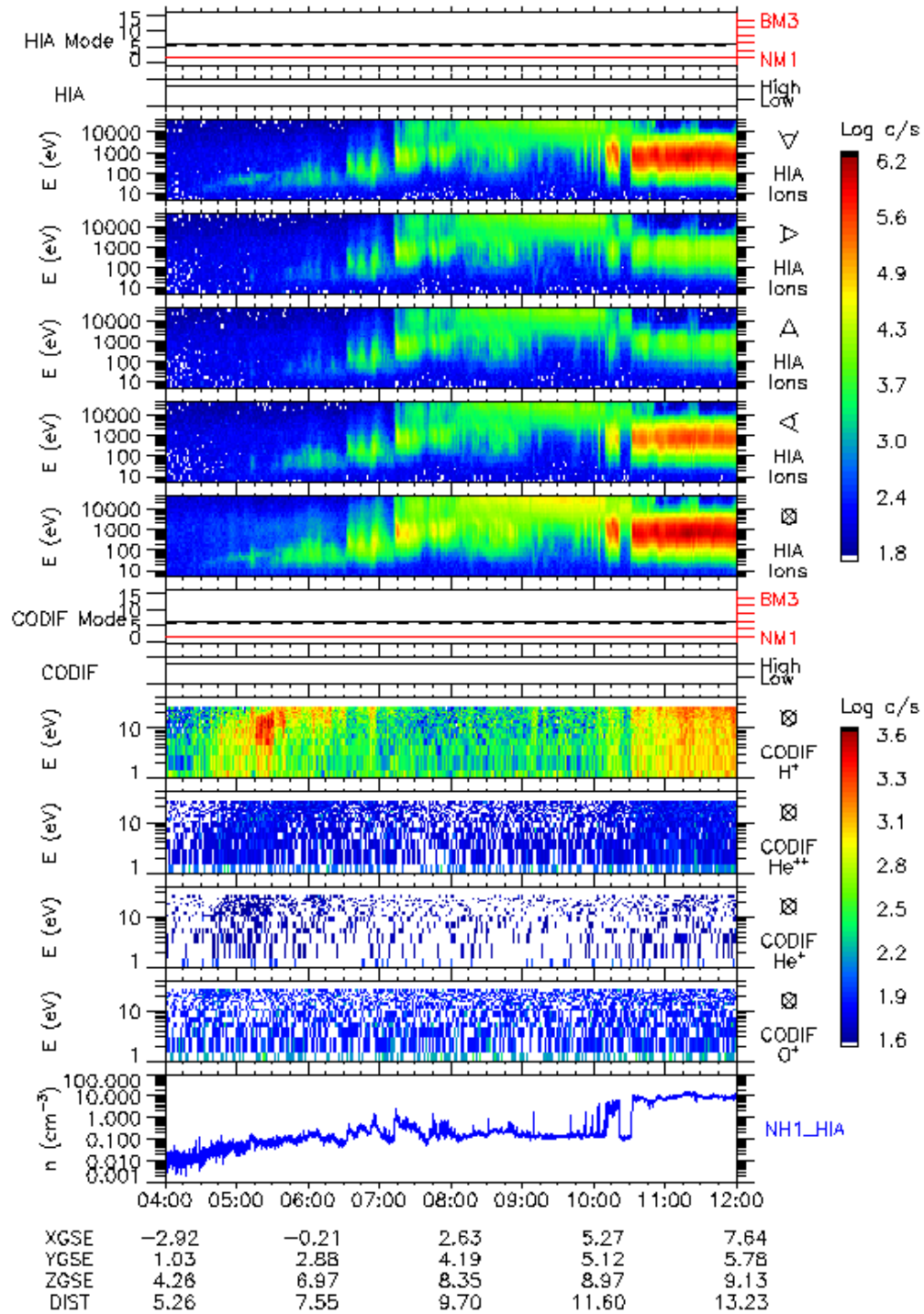
| | | | | | |
|------|-------|-------|-------|-------|-------|
| XGSE | -3.54 | -3.45 | -3.34 | -3.21 | -3.10 |
| YGSE | 0.86 | 0.96 | 1.06 | 1.17 | 1.26 |
| ZGSE | 2.83 | 3.06 | 3.27 | 3.52 | 3.72 |
| DIST | 4.62 | 4.70 | 4.79 | 4.91 | 5.00 |



CIS

SAMBA (SC 3)

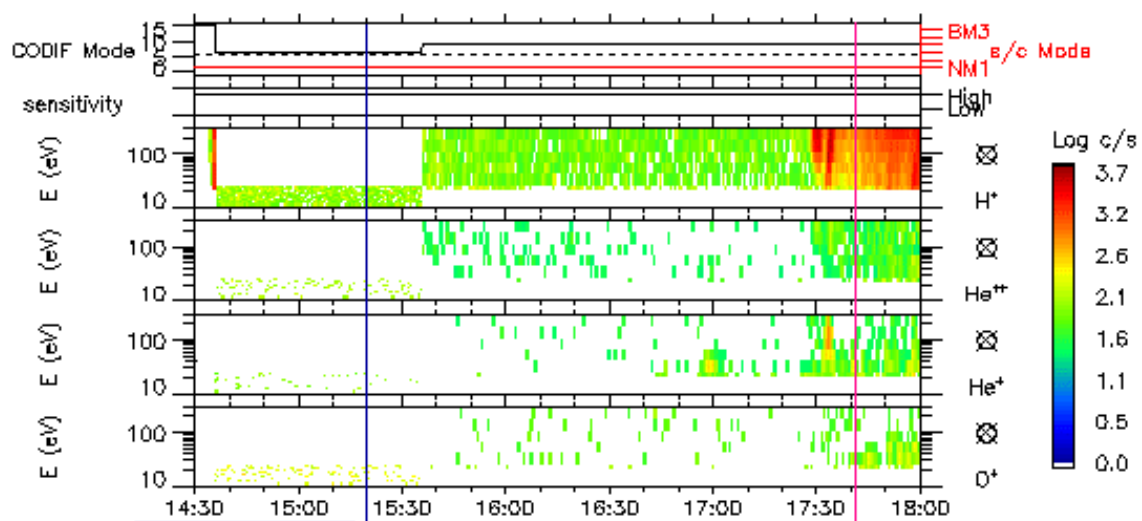
14/Feb/2001



CIS-CODIF

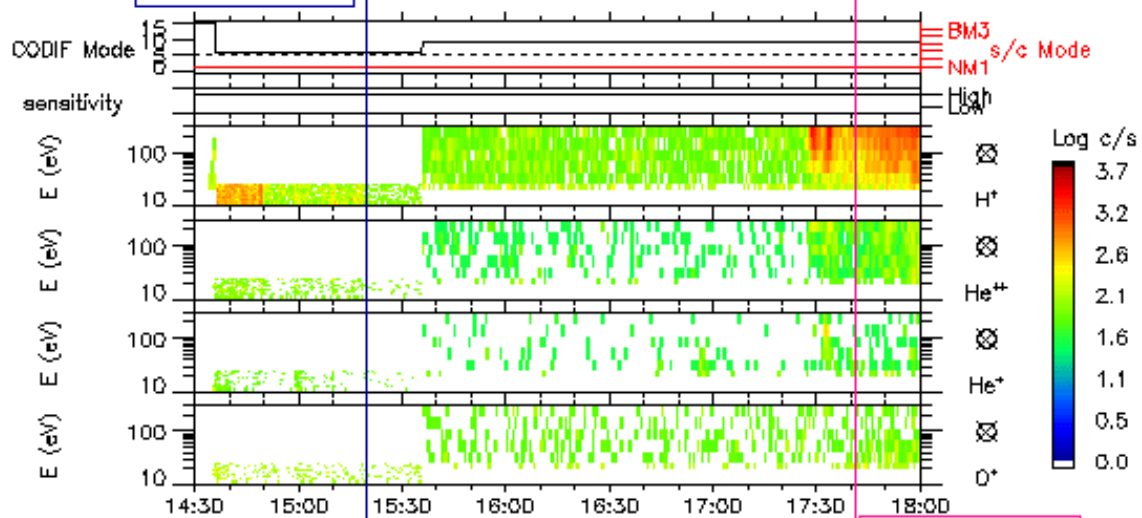
RUMBA (SC 1)

04/Feb/2001

sc3 ASPOC
Emission Stop

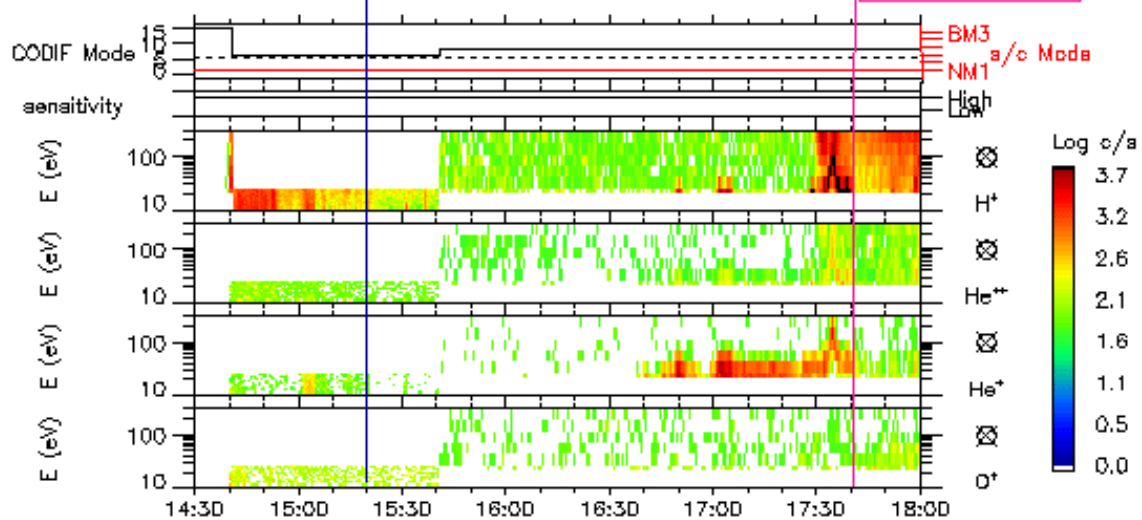
SAMBA (SC 3)

04/Feb/2001



CIS-CODIF

TANGO (SC 4)

sc4 ASPOC
Emission Stop

Produced by CNES/CESR. Printing date: 23/Feb/2001 CIS_ASPOC_sc_134.cl